Spectrum Allocation for Terahertz Band Communication Systems

Muhammed **Akram** Mohamed **Shafie**

January, 2023

A thesis submitted for the degree of Doctor of Philosophy
of The Australian National University

Research School of Engineering
College of Engineering and Computer Science
The Australian National University

Dedication

The thesis is dedicated to my father, who passed away during my PhD candidature, and to my mother .....

Declaration

The contents of this thesis are the results of original research and have not been submitted for a higher degree to any other university or institution.

The research work presented in this thesis has been performed jointly with Assoc. Prof. Nan Yang (The Australian National University), Prof. Salman Durrani (The Australian National University), Assoc. Prof. Xiangyun Zhou (IEEE Fellow, The Australian National University), Assoc. Prof. Chon Han (Shanghai Jiao Tong University, China), Assoc. Prof. Josep M. Jornet (Northeastern University, USA), Prof. Markku Juntti (IEEE Fellow, University of Oulu, Finland), Dr. Sheeraz A. Alvi (The Australian National University), Dr. Chunhui Li (Ericsson Research, Japan), Prof. Thomas Kürner (IEEE Fellow, Institut für Nachrichtentechnik, Technische Universität Braunschweig, Germany), and Prof. Trung Q. Duong (IEEE Fellow, Queen's University Belfast, U.K.). The substantial majority of this work was my own.

Much of the research work presented in this thesis has been published or has been submitted for publication as journal papers or conference proceedings.

Akram Shafie
Research School of Engineering,
College of Engineering and Computer Science,
The Australian National University,
Canberra, ACT 2601,
Australia

Acknowledgments

The work presented in this thesis would not have been possible without the help and support of a number of individuals and organizations.

- My sincere gratitude goes to my primary supervisor, Assoc. Prof. Nan Yang, for the continual guidance and support throughout my Ph.D. candidature. I am thankful for his willingness to his technical guidance and expertise. Besides that, he always trains me to be an independent researcher by providing me with chances to participate in funding proposal writing and student supervision. He also used his own networking to expand my research connections, which made me establish close collaborations with internationally leading researchers in terahertz band communications.

- I would like to thank Prof. Salman Durrani and Assoc. Prof. Xiangyun Zhou for being part of my supervisory panel. I really appreciate their effort and time for evaluating my annual progress and providing guidance regarding my Ph.D. candidature.

- Many thanks to my collaborators Assoc. Prof. Chon Han (Shanghai Jiao Tong University, China), Assoc. Prof. Josep M. Jornet (Northeastern University, USA), Prof. Markku Juntti (IEEE Fellow, University of Oulu, Finland), and Dr. Chunhui Li (Ericsson Research, Japan) for their constructive comments and helpful discussions to the research work.

- It has been a great pleasure to study in the Communications Group in the School of Engineering. I would like to thank everyone in my research group

for making the research environment a supportive and friendly one, and for the constructive conversations, I have had over the last few years.

- Thanks to The Commonwealth Department of Education and Training and The Australian National University for the fee offset and stipend Ph.D. scholarship.

- I would like to thank my lecturers at the Department of Electrical and Electronic Engineering, The University of Peradeniya, Sri Lanka, where I received my Bachelor's degree prior to commencing the Ph.D. candidature. Special thanks to Dr. Himal A. Suraweera, Prof. Roshan Godaliyadda, Prof. Janaka B. Ekanayake (IEEE Fellow), and Prof. Parakrama Ekanayake for mentoring and inspiring me to do a Ph.D.

- Special thanks to Dr. Samitha Herath and Dr. Sheeraz A. Alvi for the great help and kind support during my Ph.D. candidature, especially at times when my own confidence was lacking.

- Last but not least, I would like to express my utmost gratitude thank to my parents, my wife, my siblings, and my in-laws, for their love and support throughout my life, and particularly over the course of my Ph.D. candidature.

Abstract

Terahertz (THz) band communication (THzCom) has been envisaged as a highly promising paradigm for the sixth-generation (6G) and beyond era. In particular, the ultra-wide spectrum ranging from 0.1 to 10 THz and the short wavelengths at the THz band offer enormous potential to realize new applications that demand ultra-high-data rates. The exploration of novel and efficient spectrum allocation strategies is of paramount significance to harness the potential of the THz band. When such strategies are to be devised, the unique characteristics of the THz band, such as the frequency- and distance-dependent molecular absorption loss, pose new and pressing challenges that have never been seen at lower frequencies. Against this background, this thesis aims to design and analyze novel and efficient spectrum allocation strategies for multiuser THzCom systems that can wisely tackle the challenges imposed by the characteristics at the THz band.

First, in Chapter 2, we, for the first time, propose multi-band-based spectrum allocation with adaptive sub-band bandwidth (ASB) to improve the spectral efficiency of multiuser THzCom systems, by allowing to divide the to-be-allocated spectrum into sub-bands with unequal bandwidth. To study the impact of ASB, we formulate a resource allocation problem, while focusing on spectrum allocation. We then propose reasonable approximations and transformations and arrive at a solvable approximate convex problem. Aided by numerical results, we show that considering ASB leads to a significantly higher data rate as compared to considering equal sub-band bandwidth.

Second, in Chapter 3, we propose a novel spectrum allocation strategy for multiuser THzCom systems when the to-be-allocated spectrum is composed of multiple transmission windows (TWs). Specifically, we explore the benefits and designs of (i) sub-band assignment, (ii) avoiding using some spectra that exist at

the edges of TWs where molecular absorption loss is very high, and (iii) ASB. With these considerations in mind, we formulate a resource allocation problem and solve it using a convex-optimization-based approach. Aided by numerical results, we show that data rate gains, as well as improvement in the feasibility region of the resource allocation problem, can be obtained by adopting ASB and optimally determining the unused spectra at the edges of TWs.

Third, in Chapter 4, we propose an unsupervised learning-based approach to obtaining the solution to the multi-band-based spectrum allocation problem with ASB. In the proposed approach, we first train a deep neural network (DNN) while utilizing a loss function that is inspired by the Lagrangian of the formulated problem, and then approximate the near-optimal sub-band bandwidths using the trained DNN. Aided by numerical results, we show that when the values of the molecular absorption coefficient within the to-be-allocated spectrum vary highly non-linearly, the proposed unsupervised learning-based approach outperforms the existing approximate approaches.

Finally, in Chapter 5, we investigate (i) the modeling and analysis of different types of blockages in a THzCom system and (ii) the coverage probability of an indoor three-dimensional (3D) THzCom system when frequency reuse is considered. We first characterize the joint impact of blockages caused by the user itself, moving humans, and wall blockers in a THzCom environment, and then derive the blockage probabilities associated with a point-to-point THzCom link. We then develop a tractable analytical framework, using stochastic geometry, to evaluate the coverage probability by characterizing the regions where dominant interferers (i.e., those that can cause outage by themselves) can exist, and the average number of interferers that exist in these regions. Using numerical results, we show the significance of blockage characterization and coverage analysis in a 3D THzCom system while considering the unique THz band propagation properties.

Contents

List of Publications

The research work of my Ph.D. candidature has been published, accepted, or submitted for publication as journal papers or conference proceedings in [1–10]. For ease of reference, [1–10] are denoted by [J1-J6] and [C1-C4], respectively, and are listed as follows:

Journal Papers

[J1]. **A. Shafie**, N. Yang, S. Durrani, X. Zhou, C. Han, and M. Juntti, "Coverage analysis for 3D terahertz communication systems," *IEEE J. Sel. Areas Commun.*, vol. 39, no. 6, pp. 1817–1832, June 2021. (Chapter 5)

[J2]. **A. Shafie**, N. Yang, S. A. Alvi, C. Han, S. Durrani, and J. M. Jornet, "Spectrum allocation with adaptive sub-band bandwidth for terahertz communication systems," *IEEE Trans. Commun.*, vol. 70, no. 2, pp. 1407–1422, Jan. 2022. (Chapter 2)

[J3]. **A. Shafie**, N. Yang, C. Han, and J. M. Jornet, "Novel spectrum allocation among multiple transmission windows for terahertz communication systems," *IEEE Trans. Veh. Techn.*, vol. 71, no. 12, pp. 13415–13421, Dec. 2022. (Chapter 3)

[J4]. **A. Shafie**, N. Yang, C. Li, X. Zhou, and T. Q. Duong, "Spectrum Allocation for Multiuser Terahertz Communication Systems: An Unsupervised Learning Approach," *submitted to IEEE J. Topics Signal Process.*, Dec. 2022. (Chapter 4)

[J5]. **A. Shafie**, N. Yang, C. Han, J. M. Jornet, M. Juntti, and T. Kürner, "Terahertz communications for 6G and beyond wireless networks: Challenges, key advancements, and opportunities," *IEEE Netw. Mag.*, pp. 1–8, Sept. 2022. (Chapters 1 and 6)

[J6]. N. Yang and **A. Shafie**, "Terahertz communications for massive connectivity and security in 6G and beyond era," *IEEE Commun. Mag.*, pp. 1–7, Oct. 2022. (Chapters 1 and 6)

Conference Proceedings

[C1]. **A. Shafie**, N. Yang, and C. Han, "Multi-connectivity for indoor terahertz communication with self and dynamic blockage," in *Proc. IEEE Int. Conf. Commun. (ICC)*, Dublin, Ireland, June 2020, pp. 1–7. (Not included in the thesis)

[C2]. **A. Shafie**, N. Yang, Z. Sun, and S. Durrani, "Coverage analysis for 3D terahertz communication systems with blockage and directional antennas," in *Proc. IEEE Int. Conf. Commun. (ICC) Workshop*, Dublin, Ireland, June 2020, pp. 1–7. (Chapter 5)

[C3]. **A. Shafie**, N. Yang, S. Alvi, S. Durrani, C. Han, and J. M. Jornet, "Adaptive sub-band bandwidth enabled spectrum allocation for terahertz communication systems," in *Proc. IEEE Int. Conf. Commun. (ICC)*, Seoul, South Korea, May 2022, pp. 4013–4018. (Chapter 2)

[C4]. **A. Shafie**, C. Li, N. Yang, X. Zhou, and T. Q. Duong, "An unsupervised learning approach for spectrum allocation in terahertz communication systems," in *Proc. IEEE Global Commun. Conf. (Globecom)*, Rio de Janeiro, Brazil, Dec. 2022, pp. 3447–3453 **(Best Paper Award)**. (Chapter 4)

The journal papers [J1-J6] and conference proceedings [C2-C4] are used in the thesis. The conference proceeding [C1] is related to the thesis but not explicitly used in the thesis.

List of Acronyms

THz	Terahertz
THzCom	Terahertz band communication
GHz	Gigahertz
TW	Transmission window
PACSR	Positive absorption coefficient slope region
NACSR	Negative absorption coefficient slope region
ASB	Adaptive sub-band bandwidth
ESB	Equal sub-band bandwidth
DAMC	Distance-aware multi-carrier
LUCW	Long-user-central-window
mmWave	Millimetre wave
VLC	Visible light communication
ITU	International Telecommunication Union
6G	Sixth-generation
5G	Fifth-generation
4G	Fourth-generation
LTE	Long-Term Evolution
KPI	Key performance indicator
QoS	Quality-of-service
MC	Multi-connectivity

NOMA	Non-orthogonal multiple access
IoT	Internet of Things
SCA	Successive convex approximation
ML	Machine learning
DNN	Deep neural network
LoS	Line-of-sight
nLoS	Non-line-of-sight
Inter-BI	Inter-band interference
Intra-BI	Intra-band interference
AWGN	Additive white Gaussian noise
SNR	Signal-to-noise ratio
SINR	Signal-to-interference-plus-noise ratio
CSI	Channel state information
MIMO	Multiple-input-multiple-output
HBA	Hybrid beamforming architecture
DAoS	Dynamic array-of-subarray
TTD	True-time delay
DSP	Digital signal processing
AP	Access point
UE	User equipment
2D	Two-dimensional
3D	Three-dimensional
DKE	Double knife-edge
RD	Random directional
LBLRTM	Line by line radiative transfer model
PDF	Probability density function
PPP	Poisson point process

List of Figures

List of Tables

Chapter 1

Introduction

1.1 Background

We live in an era of remarkable expansion of wireless data traffic. The wireless data demands have doubled every eighteen months over the past three decades and are currently approaching the capacity of wired communication systems [11]. The International Telecommunication Union (ITU) predicts that by 2030, the global wireless data traffic will reach an astonishingly 5 zettabytes per month and the number of connected devices could surge beyond 50 billion [12]. Although the recently launched fifth-generation (5G) cellular systems can offer significant advancements beyond fourth-generation (4G) Long-Term Evolution (LTE) systems, these systems are inherently limited in supporting the data and connection demands in the 2030s. This is because the initial premise of 5G was to enable the Internet of Things (IoT) applications with low latency requirements [13]. This has prompted the industry and academia to look beyond 5G and conceptualize and design a new generation of wireless technology, termed sixth-generation (6G) [14]. The 6G wireless technology is expected to meet a wide variety of key performance indicators (KPIs), such as peak and average user data rates of up to one terabit per second (Tb/s) and one gigabit per second (Gb/s), respectively, which are 10 to 20 times higher than those of 5G, connection density of 10^7 devices/km^2, and ultra-low end-to-end latency of less than 1 millisecond [15].

The global research community and industry have reached the consensus that

harnessing promising spectrum at high frequencies is necessary to meet the KPIs, especially those related to data rates, of 6G and beyond era [16]. With this in mind, the upper spectrum region of the 5G solution – millimeter wave (mmWave) band (24–100 gigahertz (GHz)) – has been explored [17,18]. Despite so, it turns out that it is extremely difficult to use the upper mmWave band to support multi-Gb/s data rates since the total consecutive bandwidth available within this is less than 10 GHz. Also, although visible light communication (VLC) (430–770 terahertz (THz)) shows significant promise, it faces several challenges, such as interference with natural light, lack of line-of-sight (LoS) for mobile users, and health risks posed by flickering on human eyes [19, 20]. These challenges have prompted the exploration of the spectrum between mmWave and VLC frequencies, i.e. the terahertz (THz) band, for innovative wireless paradigms for the 6G and beyond era.

1.1.1 Terahertz (THz) Band Communication

The THz band communications (THzCom) has been envisaged as a highly promising paradigm for 6G and beyond era [21–23]. The THzCom refers to the communications in the electromagnetic spectrum ranging from 0.1 THz to 10 THz. The huge available bandwidths in the order of tens up to a hundred GHz and the extremely short wavelengths offer enormous potential to realize promising 6G applications that demand high data rates, such as holographic telepresence, augmented/virtual/extended reality, Gb/s Wi-Fi for conferencing and smart offices, high-speed wireless backhaul, smart factory, wireless data centers, and military communication networks [24–26]. These applications are beyond the reach of sub-6 GHz and mmWave communications, and VLC, which undoubtedly creates the need for THzCom. Additionally, THzCom systems possess the inherent benefit of seamlessly integrating with other emerging THz band technologies, such as THz sensing, imaging, and high-precision localization, to dramatically improve the performance of 6G networks [27]. Thus, similar to mmWave communication which was first envisioned and then utilized for 5G, THzCom will inevitably play an indispensable role in developing 6G and beyond wireless networks.

Despite the promise, signals transmitted over THz channels experience characteristics that are different from those encountered at lower frequencies, which

results in new and pressing challenges. Some of the THz band characteristics related to this thesis are described as follows:

High Spreading Loss: In wireless propagation, the spreading loss increases quadratically with frequency as antenna apertures decrease at both ends of a wireless link [28]. Given the very high frequencies at the THz band, the signal propagated over a THz link is impacted by the severe spreading loss [29]. For example, the free space spreading loss experienced by a THz signal transmitted over 10m is over 100 dB, making long-range THz transmission challenging [30].

Molecular Absorption Loss: The THz band is uniquely characterized by the molecular absorption loss, resulting from the phenomenon that THz signal energies are absorbed by water vapor and oxygen molecules in the propagation medium [29]. The severity of molecular absorption loss depends on the operating frequency and transmission distance [31]. In particular, certain frequencies of the THz spectrum are very sensitive to molecular absorption. Thus, molecular absorption peaks exist at such frequencies, where the THz signal energy is profoundly decreased, and this existence of molecular absorption peaks creates transmission windows (TWs), as illustrated in Fig. 1.1. In this thesis, the entire spectrum regions that exist between neighboring molecular absorption coefficient peaks are defined as TWs [32]. Within TWs, drastically varying molecular absorption loss is experienced and this variation increases with the transmission distance, as shown in Fig. 1.2.

High Sparsity: The wavelength of THz signals is extremely short, e.g., at the level of millimeter and sub-millimeter, thus becoming comparable to the surface roughness of typical objects in the environment [29]. This implies that the surfaces considered smooth at lower frequencies are rough at the THz band. When THz waves hit such rough surfaces, very high reflection, diffraction, and scattering losses occur, leading to significant attenuation of the non-line-of-sight (nLoS) rays [33,34]. This results in high sparsity of THz channels and triggers the need for LoS links for reliable transmission.

High Vulnerability to Blockages: Given the extremely short wavelength of THz signals, THz propagation is highly vulnerable to various types of blockages [33, 35]. Specifically, objects with small dimensions such as the user itself, moving humans, and inherent indoor constructions, can act as impenetrable blockers. This vulnerability significantly limits the transmission distance of THz signals

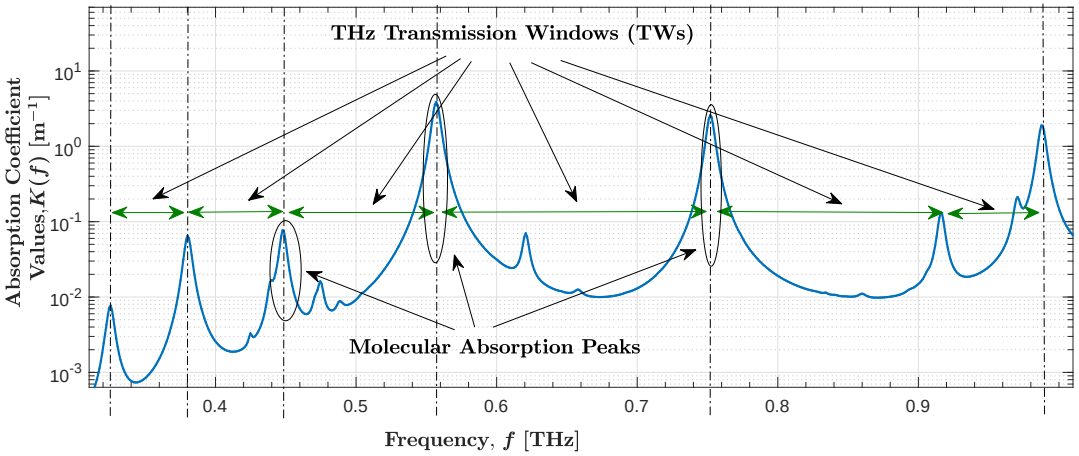

Figure 1.1: Illustration of molecular absorption peaks and transmission windows (TWs) at the THz band within the spectrum range from 0.32 THz and 1 THz.

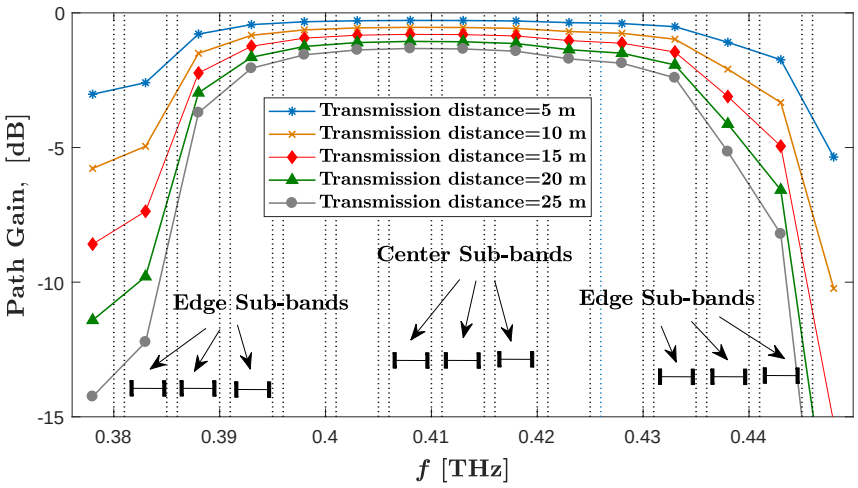

Figure 1.2: Variation of path gain within the TW between 0.38 THz and 0.45 THz for different transmission distances.

and reinforces the importance of LoS propagation in THzCom.

In 2011, Jornet and Akyildiz presented the first impactful work on physical layer communications at the THz band in [29], where some of the aforementioned characteristics and their impacts were discussed. From there onwards, THz band physical layer communications research has rapidly accelerated across the globe [36]. Despite this, considerable progress still needs to be made on new communications and

signal processing mechanisms to realize ready-to-use THzCom systems [37].

1.1.2 Spectrum Allocation for THzCom

The exploration of novel and efficient spectrum allocation strategies is of paramount significance to harnessing the potential of the THz band [38, 39]. Specifically, the aforementioned propagation characteristics at the THz band, especially the frequency- and distance-dependant nature of molecular absorption loss, are unique and pose new and pressing challenges that have never been seen at lower frequencies. Thus, it is necessary to understand these characteristics and then apply them to the analysis, design, and development of novel spectrum allocation strategies for THzCom systems.

For very short transmission distances (less than one meter), the molecular absorption loss is very low and remains almost the same throughout the THz band [40, Fig. 1]. Due to this phenomenon, the single-band pulse-based spectrum allocation scheme, where the entire THz band is considered as a single band, is proposed for applications with very short transmission distances, e.g., nanonetworks and device-to-device communications [41–44]. However, when transmission distances are relatively long, the molecular absorption varies significantly within the THz band, which makes it impossible to use single-band pulse-based spectrum allocation schemes. This necessitates the exploration of efficient spectral allocation schemes, based on carrier-based modulation strategies, for utilizing the bandwidths available within TWs towards micro- and macro-scale THzCom applications [43]. In THz band carrier-based systems, the to-be-transmitted data is first modulated into single/multi-carrier waveforms and/or pulses, and then the modulated signals are upshifted to higher THz band frequencies via expensive and sensitive cascaded frequency multipliers.

In the literature, two types of carrier-based spectrum allocation schemes are explored for micro- and macro-scale THzCom systems, namely, multi-TW-based spectrum allocation and multi-band-based spectrum allocation. In the multi-TW-based spectrum allocation scheme, individual TWs are fully allocated to separate high-speed communication links while exploring wideband signals that have bandwidths equal to those of TWs [40, 45]. When this scheme is adopted in multiuser

THzCom systems, only a limited number of users can be supported without utilizing complex interference cancellation schemes, since the number of available TWs within the entire THz band is limited. Alternatively, in the multi-band-based spectrum allocation scheme, the to-be-allocated spectrum is divided into a set of non-overlapping sub-bands that have a relatively small bandwidth, and then the sub-bands are utilized to satisfy the service demands of single or multiple users in the system [32, 46].[1] When this scheme is adopted in multiuser THzCom systems, first, a higher number of users can be accommodated since there are a relatively larger number of sub-bands. Second, intra-band interference (Intra-BI) can be reduced by assigning the users to different sub-bands, where Intra-BI refers to the interference caused due to multiple users sharing the same spectrum resource. Third, frequency selectivity within the spectra to be utilized by individual users can be reduced, which would become beneficial in minimizing the channel squint effect and temporal broadening [32, 46, 49].[2] Due to these, this scheme has been widely explored for micro- and macro-scale multiuser THzCom applications [32, 46, 50–54].

Against this background, this thesis is motivated to investigate the design and analysis of novel and efficient multi-band-based spectrum allocation schemes for multiuser THzCom systems.

1.2 Research Challenges and Limits of Existing Solutions

Despite the promise, the design of efficient multi-band-based spectrum allocation schemes brings new and pressing challenges. We must overcome these challenges to fully unlock the lucrative benefits offered by the THz band. In this section, while primarily focusing on a practical yet complex indoor THzCom system, as depicted

[1] The multi-band-based spectrum allocation scheme is similar to the frequency division multiple access (FDMA) discussed at sub-6G and mmWave communication systems [47, 48]. However, following previous studies at the THz band [32, 46], we use the term multi-band-based spectrum allocation scheme consistently throughout this thesis.

[2] We clarify that channel squint effect refers to the phase shift errors introduced during beamforming at the THz band when THzCom systems generally have large bandwidth [49]. Also, temporal broadening refers to the pulse broadening in the time domain due to the frequency selective nature of molecular absorption loss [32, 46].

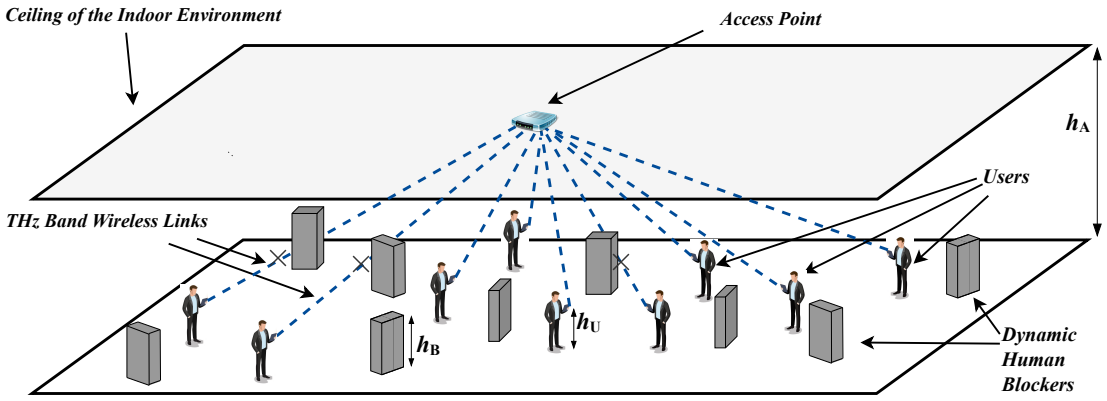

Figure 1.3: Illustration of the typical three-dimensional (3D) THzCom system studied in this thesis, where a single access point (AP) supports the downlink transmission of users that demand high data rates in the presence of blockers.

in Fig. 1.3, we discuss the research challenges and limits of existing solutions, which are described as follows:

1.2.1 Sub-band Assignment in Multiuser THzCom Systems

The molecular absorption loss, which is unique and non-negligible at the THz band, is frequency- and distance-dependent. Due to this, users that are assigned to sub-bands that exist even within a TW, experience drastically varying channel quality levels depending on the sub-bands that they are assigned and their transmission distances. Specifically, on one hand, due to the frequency-dependent nature of molecular absorption loss, even a single user with a fixed transmission distance experiences different channel quality levels depending on where the sub-band to which it is assigned is located. As shown in Fig. 1.2, the users assigned to center sub-bands experience favorable channel quality levels, as compared to the users assigned to edge sub-bands. Here, center and edge sub-bands are the sub-bands that exist at the center and edge regions of the TWs, respectively (see Fig. 1.2). On the other hand, due to the distance-dependent nature of molecular absorption loss, users with different transmission distances experience different channel quality levels even if assigned to the same sub-band, as shown in Fig. 1.2. These characteristics necessitate the efficient assignment of sub-bands among the users, such that the quality-of-service (QoS) requirements of all the users in the system are satisfied.

Motivated by this necessity, several studies have explored sub-band assignment strategies for multiuser THzCom systems. The distance-aware multi-carrier (DAMC)-based sub-band assignment strategy, also referred to as the long-user-central-window (LUCW) principle, was proposed in [32], in order to improve the data rate fairness among the users. Particularly, [32] proposed to assign edge sub-bands to the users with shorter transmission distances and center sub-bands to the users with longer transmission distances. Adopting DAMC-based sub-band assignment, resource allocation problems in THz band backhaul networks and non-orthogonal multiple access (NOMA)-assisted THzCom systems were discussed in [51] and [52], respectively. Despite the promise, it is noted that DAMC-based sub-band assignment is a heuristic technique, i.e., an approach that employs a practical and convenient method that is not guaranteed to be optimal; hence, its optimality needs examination. Moreover, DAMC-based sub-band assignment is readily applicable only within a TW. New challenges related to sub-band assignment arise when the to-be-allocated spectrum spans multiple TWs. For example, the number of sub-bands that exist within each TW needs to be optimally decided since the pathloss and the variation of molecular absorption loss change considerably between TWs. Also, the set of users that are served by each TW needs to be identified. These challenges necessitate the study of optimal sub-band assignment for multiuser THzCom systems, especially when the to-be-allocated spectrum spans multiple TWs.

To determine the optimal sub-band assignment, optimization problems can be formulated while considering sub-band assignment indicators as design variables. However, such problems are mixed-integer non-linear problems and are difficult to solve using traditional optimization techniques without rendering modifications to the problems. Recently, sub-band assignment algorithms for THzCom systems based on the alternative optimization technique and the alternative direction method were developed in [50] and [53], respectively, to attain near-optimal performance.

1.2.2 Spectrum Allocation with Adaptive Sub-band Bandwidth

It has been identified that the consideration of equal sub-band bandwidth (ESB), where the to-be-allocated spectrum is divided into sub-bands with equal bandwidth, increases the variation of the channel quality level among the users that are assigned to sub-bands. Specifically, when ESB is considered, all sub-bands are allocated the same bandwidth, irrespective of whether they are edge or center sub-bands. However, the molecular absorption losses are drastically different in the center and edge sub-bands, as shown in Fig. 1.2. This leads to the users that are assigned to edge sub-bands and center sub-bands experiencing highly unfavorable and favorable channel quality levels, respectively, thus causing a large variation of channel quality among the users in multiuser systems. Due to this high variation, on one hand, the QoS requirements of the users assigned to edge sub-bands may not be satisfied. On the other hand, the users assigned to center sub-bands may possess spectrum resources far beyond what they might need to satisfy their QoS requirements.

To overcome this challenge, multi-band-based spectrum allocation schemes enabled with adaptive sub-band bandwidth (ASB) can be explored, by allowing to change the bandwidth of sub-bands. The consideration of ASB allows the users that are assigned to edge sub-bands and center sub-bands to occupy larger and smaller bandwidths, respectively, as compared to what would have been allocated when ESB is considered. This can lead to the satisfaction of QoS requirements of all users and the avoidance of spectrum redundancy.

Despite the promise of ASB, all previous studies on multi-band-based spectrum allocation schemes, i.e., [32, 46, 50–54], considered ESB. The impact of distance-varying usable bandwidth on multi-band-based spectrum allocation schemes was discussed in [46]. However, [46] considered that when the usable bandwidth within TWs changes, the number of sub-bands that can be utilized for communication changes, but the bandwidth of the sub-band remains unchanged. Some recent studies in [40, 45] considered variable bandwidths for THzCom systems. However, we note that [40, 45] explored multi-TW-based spectrum allocation schemes, where the individual TWs are fully allocated to separate high-speed communications links;

thus, the design principles in [40, 45] cannot be applied for the multi-band-based spectrum allocation schemes with ASB.

To develop multi-band-based spectrum allocation schemes with ASB, first, spectrum allocation problems need to be formulated while considering the sub-band bandwidths as design variables. Then, the formulated problems need to be solved efficiently by using traditional or non-traditional optimization techniques [37]. It is found that the spectrum allocation problems with ASB are highly non-convex. The non-convexity arises mainly due to the achievable rates of users being non-convex with respect to (w.r.t.) the design variables.[3] To overcome this challenge, first, reasonable approximations and transformations need to be found to transform the problems into standard convex optimization problems. Then, standard convex problem solvers might need to be utilized to attain solutions [55, 56]. Alternatively, emerging non-traditional optimization techniques such as machine learning (ML) can be explored to attain near-optimal solution [57, 58]. Various ML models have been widely explored for wireless communication systems, e.g., [59–64]. Nevertheless, these studies primarily focused on utilizing supervised learning models, which may not be applicable for spectrum allocation problems with ASB, due to the unavailability of labeled data [65]. Thus, unsupervised learning models need to be explored to learn the constrained optimization problem and then obtain the near-optimal solution [66, 67].

1.2.3 Under-utilization of Edge Spectra of Transmission Windows

An important challenge arises in multi-band-based spectrum allocation schemes with regard to the under-utilization of a certain segment of the to-be-allocated spectrum. The molecular absorption losses are extremely high at edge regions of

[3]We note that resource (such as spectrum, power, and bits) allocation problems are widely explored for multiuser sub-6 GHz and mmWave communication systems, and the formulated problems are solved typically via convex optimization (such as the water-filling method) [28]. However, these studies did not consider the impact of molecular absorption loss, which is unique at the THz band. When molecular absorption loss is considered, resource allocation problems become highly non-convex w.r.t. the design variable, bandwidth. This necessitates the development of novel optimization algorithms, which are different from those proposed for sub-6G and mmWave systems in the existing literature.

TWs as compared to those in central regions of TWs. Thus, it may be beneficial if some spectra at edge regions of TWs are avoided from utilization during spectrum allocation. This consideration is most beneficial when the to-be-allocated spectrum spans multiple TWs.

Despite the benefits of under-utilization of spectra at edge regions of TWs, it has rarely been examined in previous studies in THz band spectrum allocation. The studies [32, 51–54] considered that the entire spectrum existing within the to-be-allocated spectrum is fully utilized. Several recent studies [40, 45, 68] considered avoiding certain spectra at edge regions of TWs. Specifically, [45, 68] proposed to avoid edge regions of TWs where the molecular absorption loss is greater than a predefined molecular absorption loss. Also, [40] proposed to avoid a certain segment of edge regions of TWs, whose utilization could lead to more than 3 dB path loss difference for a given predefined transmission distance. Despite the efforts in [40, 45, 68], it is noted that they considered the unused spectra at edge regions of TWs to be pre-defined, i.e., arbitrarily chosen and fixed, which may not guarantee the optimal performance.

1.2.4 Inter-band Interference

The inter-band interference (Inter-BI) is an important performance limiting factor in multi-band-based spectrum allocation schemes, especially when each user demands multiple sub-bands to satisfy its QoS requirements [25]. The Inter-BI at the THz band can be caused by power leakage from adjacent sub-bands, as well as the harmonics generated in frequency multiplying chains during frequency upshifting. Given the high bandwidth available at the THz band, sub-bands can be well-spaced to avoid the effect of Inter-BI. Despite so, the need to fully utilize the bandwidths available in TWs may arise, in order to satisfy the KPIs of 6G and beyond networks. Due to this, when sub-bands are close to each other, the impact of Inter-BI needs to be precisely modeled, analyzed, and then mitigated or eliminated to reap the benefits of multi-band-based spectrum allocation schemes.

It is noted that the Gaussian approximation has been widely used to model Inter-BI at sub-6 GHz and mmWave frequencies, assuming that neighboring sub-bands have similar channel quality [32, 46]. However, the applicability of this ap-

proximation at the THz band needs to be re-examined, since the adjacent THz sub-bands exhibit drastically different channel characteristics, due to molecular absorption loss. As for Inter-BI suppression, recently, Inter-BI suppression schemes that can suppress Inter-BI with minimal throughput degradation [68] and waveform designs that minimize power leakages to adjacent bands [69] were proposed. However, time-domain front-end filtering, subcarrier weighting, windowing, and orthogonal precoding methods need to be carefully investigated to further mitigate the impact of Inter-BI in multi-band-based spectrum allocation schemes.

1.2.5 Blockage Management

The general understanding in mmWave communication systems is that penetration losses across objects with small dimensions are high, but are not strong enough to fully block the communication signals [70, 71]. Unlike at the mmWave band, the signals at the THz band can be completely blocked by objects with small dimensions such as the user itself, moving humans, and inherent indoor constructions (e.g., walls and furniture). This is due to the very high penetration losses experienced by THz signals as a result of their very small wavelengths [33, 35]. This necessitates the precise modeling of blockages, analyzing their impact on THzCom systems, and then devising strategies to mitigate their impacts.[4] We discuss two research directions related to blockage management in the following subsections.

1.2.5.1 Blockage Modeling

The impact of human blockers on the THzCom system performance was studied in [72–75]. However, [72–75] modeled the human blockers using the simplified circular cylindrical model, which may not accurately model humans. Thus, the need exists to model human blockers using a more accurate model, such as the double knife-edge (DKE) model [76], and then derive performance metrics while considering the specifications of the more accurate model. In addition, it is noted that the previous studies in [72–75] did not consider the impact of wall blockers, despite that the primary applications of THzCom systems are found in indoor

[4]We clarify that blockage management, and the challenges discussed in the subsequent subsections 1.2.6 and 1.2.7, are experienced even by other THz band spectrum allocation schemes.

environments where walls exist. Moreover, we clarify that non of the previous studies at the THz band studied the impact of self-blockages, although self-blockage may lead to the fact that signals from some access points (APs) surrounding a user are totally blocked, even if the APs are within close proximity [71, 77].

1.2.5.2 Multi-connectivity

Among various promising solutions, multi-connectivity (MC) is recognized as a promising solution to address the reliability degradation caused by blockages in THzCom systems. When multiple APs exist in the system, MC allows users to associate and communicate with multiple APs simultaneously [78–80].[5] The design of MC-enabled THzCom systems is hugely beneficial but complicated since it requires advancements in several aspects of THzCom systems. First, MC strategies require a cell-free architecture with centralized controlling, data processing, and combining strategies. This in turn demands high-capacity backhaul connections and precise clock synchronization as well as promising packet scheduling methods, such as packet duplication and packet splitting, for latency reduction. Second, dynamic AP selection strategies need to be wisely designed to improve the reliability and throughput performance in MC-enabled THzCom systems, at the cost of frequent AP switching [81]. Given this cost, "lightweight" solutions in terms of software and hardware implementations need to be examined, aiming to provide a trade-off between improving the reliability/throughput performance and AP switching [82].

1.2.6 Frequency/Sub-band Reuse in THz Band Spectrum Allocation

The majority of early studies on multi-band-based spectrum allocation schemes considered that the users in the system are served by separate sub-bands, e.g., [32, 46, 50]. This was to ensure Intra-BI-free data transmission and to eliminate the signal processing overhead and hardware complexity caused by frequency/sub-band

[5] We clarify that several terminologies such as multi-connectivity, cooperative transmission, joint transmission, concurrent transmission, and coexisting communication, have been used in the literature to denote simultaneous association and communication of users with multiple APs [78–80]. However, following [78, 79], we use the term multi-connectivity in this thesis.

reuse in the system. However, higher spectral efficiency can be achieved by leveraging frequency/sub-band reuse during spectrum allocation, which has prompted the research on frequency reuse in THz band spectrum allocation [38]. We discuss two research directions related to frequency reuse in the following subsections.

1.2.6.1 Coverage Probability Analysis

When frequency reuse is considered, Intra-BI is experienced among the users assigned to the same sub-band. Hence, the need arises to first model Intra-BI in a tractable manner. Then, the reliability degradation that occurs as a result of Intra-BI needs to be examined by quantifying the performance metrics such as coverage probability, where coverage probability is the probability that the signal-to-interference-noise (SINR) at a user is larger than the predefined SINR threshold.

In sub-6 GHz and mmWave communication systems, the coverage probability in the presence of Intra-BI has been widely investigated [83–85]. Despite this, the studies on the coverage probability at the THz band that incorporates all the unique characteristics of THzCom systems are very limited. Using tools from stochastic geometry and considering Intra-BI limited regime, the coverage probability for THzCom systems was determined in [86] by approximating the Intra-BI distribution using a log-logistic distribution. The Intra-BI and coverage probability of dense THz wireless networks was investigated in [87], using the conventional Laplace transform-based analysis. Additionally, the Intra-BI distribution was approximated using a normal distribution in [88] for tractable coverage probability analysis of dense THzCom systems. In other studies in [74,75], the coverage probability of THzCom systems was derived, but the accuracy of their results deteriorates significantly, especially for long transmission distances, since they used the average Intra-BI instead of the instantaneous Intra-BI when evaluating the coverage probability. It has to be noted that despite the efforts in the studies in [74, 75, 86–88], they focused only on a two-dimensional (2D) environment.

In sub-6 GHz and mmWave communication systems, it may be reasonable to ignore the impacts of the vertical heights of communication entities due to the large transmission distance. However, the vertical dimension may greatly impact the reliability performance of THzCom systems, since transmission distances at

the THz band are limited to the order of a few meters [15]. Thus, it is essential to consider the vertical heights of communication entities and investigate their impact on the coverage probability in THzCom systems. Very recently, the coverage probability for a THzCom system was determined in [89] for a three-dimensional (3D) environment. However, [89] did not address the impact of 3D directional antennas at both the transmitter and receiver sides.

1.2.6.2 Spatial and Power-domain Multiplexing

Besides performance analysis, new spatial and power-domain multiplexing strategies operated at the THz band need to be developed for adopting frequency reuse in THzCom systems. One of the most encouraging spatial multiplexing strategies is beam sectorization [90]. In a THzCom system with beam sectorization, each AP can perform beamforming to form non-overlapping beam sectors with high directional gains, and the entire THz spectrum available in the system can be reused within beam sectors. Two challenges need to be tackled to reap the most benefits of beam sectorization [91]. The first challenge is inter-sector interference cancelation which minimizes or eliminates the impairment caused by non-ideal beam shapes. The second challenge is sector deployment, i.e., the identification of sector regions, which can be addressed by 2D sector deployment.

As an emerging power-domain multiplexing strategy, non-orthogonal multiple access (NOMA) brings an extra degree of freedom in the power domain [92]. In NOMA, superposition coding and successive interference cancellation (SIC) are deployed to decode signals for different users in the same time and frequency resource block, offering additional access in congested traffic scenarios, e.g., ultra-dense networks [93]. In multiuser THzCom systems with sparse channels of users in the limited scattering environment, NOMA acts as a potential technique to improve the spectral efficiency. The application of NOMA into THzCom systems has recently attracted increasing attention, e.g., [52–54]. However, several key challenges in NOMA-aided THzCom systems still remain unanswered, e.g., (i) the construction of effective clustering criteria, including full channel knowledge-based criterion and location-based criterion, and then the evaluation of their impacts on the system spectral efficiency, (ii) development of accurate channel estimation methodologies

since NOMA requires precise channel state information (CSI), and (iii) investigation into computationally efficient SIC-based decoders since existing decoders are computationally very intensive.

1.2.7 THz Hardware Development

Despite the surge in THz research over the past decade, state-of-the-art advances still remain mostly theoretical in nature, with much emphasis on propagation and physical layer challenges [36,39]. Recently, the U.S. Federal Communications Commission (FCC) opened up the 95 GHz to 3 THz for future mobile communications [94]. This along with other contributing factors has prompted the accelerated research on THz devices and testbeds/prototypes to obtain experimental measurements, such that the theoretical evaluations can be validated. We discuss two research directions related to THz band experimental research in the following subsections.

1.2.7.1 THz Devices

For many years, the challenges associated with the on-chip generation, modulation, and radiation of THz signals have limited the utilization of the THz band. However, the THz technology gap is progressively being closed, thanks to the major advancements across different device technologies [95], although much work is left to be done on this end. Today, the majority of THzCom systems rely on frequency up-converting systems, which are able to generate (sub) THz signals starting from a mmWave oscillator by using frequency multipliers. Different processes can be utilized to build such up-converters, ranging from silicon complementary metal-oxide-semiconductor (CMOS) for milliwatt powers at frequencies of up to 200-300 GHz to the III-V semiconductor-based Hight Electron Mobility Transistor (HEMT), or the Schottky diode technology, which can provide higher hundreds of milliwatts of power at hundreds of GHz and a few milliwatts of power above 1 THz. For now, most of the THz devices rely on external high-gain directional antennas (e.g., horn and dish antennas). Only recently, fully digital antenna arrays with 8 to 16 channels have been demonstrated at frequencies between 100 and 200 GHz [95].

We also note that some of the unique research challenges and their possible solutions mentioned in the previous subsections may need new THz hardware capabilities. For example, to implement multi-band-based spectrum allocation schemes, it would be necessary to deploy very precise digital signal processing (DSP) filters, which are substantially expensive at THz frequencies, at THz transceivers [37, 96, 97]. Also, to gain the benefits of ASB, THzCom users need to be equipped with tunable front-ends for adjusting their operating frequency and bandwidth. These THz hardware capabilities are beyond the current advancements, thus motivating the development of novel and efficient THz devices.

Beyond well-established technologies, innovative solutions need to be explored when embracing new materials that open doors to new physics. Inspired by this, the use of graphene has been proposed to develop signal sources, modulators, antennas, and antenna arrays, due to its ability to support the propagation of surface plasmon polariton (SPP) waves, theoretically for frequencies as low as 100 GHz [34,95]. However, for graphene-based plasmonic devices to operate efficiently at the lower THz band, high electron relaxation times are required. Although theoretically possible, it remains experimentally very challenging; thus, at present, the majority of graphene-based plasmonic devices for THz applications are found at frequencies of 1 THz and beyond [34,95]. Interestingly, this is also the frequency range where the conventional electronic approaches to THz wave generation decay, making graphene a promising candidate. Although plasmonic nano-antenna technologies are at their early stages, the need exists to further advance such technologies, since they can drastically increase the efficiency of THzCom systems and other emerging THz band technologies, e.g., THz sensing and imaging [27].

1.2.7.2 THz Prototypes/Testbeds

Recently, several research groups have started to focus on the development of THz testbeds to obtain experimental measurements. An integrated testbed for THzCom was developed at the Institute for the Wireless Internet of Things, Northeastern University, Boston, USA [98]. Using this testbed, experimental results for wireless THzCom at 1.02 THz were obtained [99, 100]. A series of channel measurements were made in a vehicle-to-infrastructure test center at 304.2 GHz with 8 GHz band-

width and the measurement results were presented in [30]. Moreover, wideband channel measurement data for THz indoor communications were reported in [101]. Recently, efforts have been made to implement an open-source scalable and affordable prototyping platform called *MillimeTera* to support the broader mmWave and THz band research community [102].

To support THzCom research, major players in the wireless communication industry have also introduced new state-of-the-art instruments through which experimental research can be performed. For example, National Instruments (NI) Corporation developed a real-time sub-THz software-defined radio that is built on NI's mmWave transceiver system and Virginia diode's radio heads [103]. Keysight Technologies developed a 6G sub-THz testbed for 6G research [104], where an arbitrary waveform generator was used to generate a wideband intermediate frequency (IF) which is up-converted to the D or G-band. On the receive side, the signal is down-converted to a 46 GHz IF and digitized, then demodulated and analyzed with PathWave Vector Signal Analysis software. In addition, Huawei is expected to release THz band channel measurement data obtained at 140 GHz in the near future [105]. Based on the aforementioned major developments in experimental research, as well as the progress in theoretical research and the standardization efforts at the THz band over the past decade [39], we are very optimistic for the future of THzCom. We note that most THz testbeds are single-input single-output and do not rely on fully digital antenna arrays; hence, much work is still left to be done on this end to develop ready-to-use THzCom systems.

1.3 Thesis Overview and Contributions

This thesis focuses on the design and analysis of novel and efficient spectrum allocation strategies for multiuser THzCom systems that can wisely tackle the challenges imposed by the characteristics at the THz band. Specifically, the thesis investigates several research challenges encountered by multi-band-based spectrum allocation schemes, such as those discussed in subsections 1.2.1, 1.2.2, 1.2.3, 1.2.5.1, and 1.2.6.1, and propose efficient design guidelines and analytical frameworks to alleviate them. By doing so, this thesis will advance our understanding of the fundamentals of spectrum allocation strategies for THzCom systems.

Table 1.1: The overview of the four technical chapters of the thesis.

		Chapter 2	**Chapter 3**	**Chapter 4**	**Chapter 5**
Main Considerations		◇ ASB within a TW	◇ ASB across multiple TWs ◇ Sub-band assignment ◇ Under-utilization of edge spectra	◇ Machine learning for ASB ◇ Blockage characterization	◇ Blockage characterization ◇ Coverage characterization during frequency reuse
Communication Scenario	System Deployment	3D THzCom with a single AP and multiple users	3D THzCom with a single AP and multiple users	3D THzCom with a single AP and multiple users	3D THzCom with multiple APs and multiple users
	Blockages	-	-	Dynamic human blockers	Dynamic humans, walls, and self blockers
	Spectrum of Interest	Within a TW	Across multiple TWs	Within a TW	A single sub-band
Mainly used Analytical Tool		Convex optimization	Convex optimization	Machine learning	Stochastic geometry
Publi-cations		[J2, C3]	[J3]	[J4, C4]	[J1, C2]

The rest of the thesis is organized as follows. In Chapters 2 to 5, i.e., the four technical chapters of the thesis, we discuss in detail the technical contributions of the thesis. Finally, in Chapter 6, we summarize the conclusions drawn from the thesis and outline some of the research directions directly related to the thesis. In the rest of this chapter, we present the specific contributions of Chapters 2 to 5 of the thesis. A brief overview of Chapters 2 to 5 of the thesis is presented in Table 1.1.

Chapter 2 – Spectrum Allocation with Adaptive Sub-band Bandwidth for THzCom Systems

This chapter presents solutions to some of the design challenges outlined in Section 1.2.2. Specifically, the chapter investigates the benefits and the design challenges of dividing the to-be-allocated spectrum into sub-bands with unequal bandwidths. To this end, we focus on an indoor THzCom environment where a single AP supports the downlink transmission of multiple users and consider the to-be-allocated spectrum that exists entirely within a TW. For this system, we study multi-band-based spectrum allocation with ASB while considering that sub-bands are assigned according to the DAMC-based sub-band assignment strategy.

The key contributions of this chapter are summarized as follows:

- We, for the first time, propose multi-band-based spectrum allocation with ASB to improve the spectral efficiency of multiuser THzCom systems. To study the impact of ASB, we formulate a resource allocation problem, with the main emphasis on spectrum allocation with ASB. In the problem, we aim to maximize the data rate of the multiuser THzCom system under given constraints on sub-band bandwidth and power. This problem consists of the determination of the optimal sub-band bandwidth and optimal transmit power.

- We propose a solution to the formulated resource allocation problem. Specifically, we propose reasonable approximations, as well as transformations, and arrive at an approximate convex problem, which can be solved efficiently by using standard convex problem solvers.

- Aided by numerical investigation, we arrive at the following observations and design guidelines:

  - The consideration of ASB leads to a significantly higher data rate as compared to the consideration of ESB, due to the enhanced capability of ASB. Thus, it is beneficial to adopt ASB in multi-band-based spectrum allocation schemes although this can demand new THz hardware capabilities at the transceivers.

  - The performance gain of adopting ASB is most profound when the variation in molecular absorption loss within the to-be-allocated spectrum is high.

The findings from this chapter have been presented in the following publications [J2] and [C3]:
[J2]. **A. Shafie** N. Yang, S. Alvi, C. Han, S. Durrani, and J. M. Jornet, "Spectrum allocation with adaptive sub-band bandwidth for terahertz communication systems," *IEEE Trans. Commun.*, vol. 70, no. 2, pp. 1407–1422, Feb. 2022.
[C3]. **A. Shafie**, N. Yang, S. Durrani, X. Zhou, C. Han, and M. Juntti, "Coverage analysis for 3D terahertz communication systems," *IEEE J. Sel. Areas Commun.*, vol. 39, no. 6, pp. 1817–1832, June 2021.

Chapter 3 – Spectrum Allocation Among Multiple Transmission Windows for THzCom Systems

This chapter presents solutions to some of the design challenges outlined in Sections 1.2.2, 1.2.3, and 1.2.4. Specifically, the chapter investigates the benefits and design challenges of sub-band assignment, under-utilization of edge spectra of TWs, and ASB. To this end, we study a novel multi-band-based spectrum allocation scheme when the to-be-allocated spectrum is composed of multiple TWs. We clarify that the design in Chapter 2 is only applicable when the to-be-allocated spectrum exists entirely within a specific region of a TW. Differently, the design in this chapter is applicable even when the to-be-allocated spectrum spans across multiple TWs.

The key contributions of this chapter are summarized as follows:

- We propose a novel spectrum allocation strategy for multiuser THzCom systems when the to-be-allocated spectrum is composed of multiple TWs. Specifically, we explore the benefits of (i) sub-band assignment, (ii) avoiding using some spectra that exist at the edges of TWs where molecular absorption loss is very high, and (iii) ASB when the to-be-allocated spectrum is composed of multiple TWs. With these considerations in mind, we formulate

a resource allocation problem, with the primary focus on spectrum allocation, to maximize the aggregated multiuser data rate.

- We propose a solution approach to derive the sub-band assignment, sub-band bandwidth, the unused spectra at the edges of TW, and the transmit power of the formulated resource allocation problem. To this end, we first propose modifications to the formulated problem and arrive at a mixed-integer non-linear problem. We then propose several transformations, including the binary variable to real variable transformation, and arrive at an approximate convex problem. Subsequently, we develop an iterative algorithm based on the successive convex approximation technique to solve the approximate convex problem.

- Using numerical investigation, we arrive at the following observations and design guidelines:

  - Although the state-of-the-art DAMC-based sub-band assignment is a heuristic technique, it is applicable to obtain a near-optimal solution to the sub-band assignment problem at the THz band when the to-be-allocated spectrum is entirely within a TW. However, the sub-band assignment design proposed in this chapter needs to be considered when the to-be-allocated spectrum is composed of multiple TWs, since DAMC-based sub-band assignment is only readily applicable within a TW.
  - When the to-be-allocated spectrum is composed of multiple TWs, enabling ASB achieves a significantly higher data rate as compared to adopting ESB.
  - An additional gain can be obtained by optimally determining the unused spectra at the edges of TWs, as compared to avoiding using pre-defined spectra that exist at the edges of TWs, especially when the power budget constraint is stringent.
  - The feasibility region of the resource allocation problem can be improved by adopting ASB and optimally determining the unused spectra at the edges of TWs.

The main findings from this chapter have been presented in the following publication [J3]:
[J3]. **A. Shafie**, N. Yang, C. Han, and J. M. Jornet, "Novel spectrum allocation among multiple transmission windows for terahertz communication systems," *IEEE Trans. Veh. Techn.*, vol. 71, no. 12, pp. 13415–13421, Dec. 2022.

Chapter 4 – An Unsupervised Learning Approach for Spectrum Allocation in THzCom Systems

This chapter presents solutions to some of the design challenges outlined in Sections 1.2.2 and 1.2.5.1. Specifically, the chapter investigates (i) the design challenges of multi-band-based spectrum allocation schemes with ASB when the molecular absorption coefficient varies in a highly non-linear manner and (ii) the modeling and analysis of the impact of human blockages on THz band spectrum allocation.[6] We note that designs in Chapters 2 and 3 for the multi-band-based spectrum allocation problem with ASB is only applicable when the molecular absorption coefficient within the to-be-allocated spectrum is simple such that it can be modeled as a piecewise exponential function of frequency with minimal approximation errors. Differently, the approach presented in this chapter can be applicable even if the molecular absorption coefficient varies in a highly non-linear manner.

The key contributions of this chapter are summarized as follows:

- We propose an unsupervised learning-based approach to obtaining the near-optimal solution to the multi-band-based spectrum allocation problem with ASB. In the proposed approach, we first train a deep neural network (DNN) while utilizing a loss function that is inspired by the Lagrangian of the formulated problem. Then, using the trained DNN, we approximate the near-optimal solutions.

- We characterize human blockers at the THzCom systems using the more

[6]We note that in order to understand the throughput degradation caused by blockages and to develop novel spectrum management techniques for mitigating the impact of blockage on system performance, e.g., MC-enabled sub-band assignment, it is of utmost importance to delve into blockage characterization for THzCom systems.

accurate double knife-edge (DKE) model and evaluate its impact on multi-band-based spectrum allocation schemes.

- Using numerical investigation, we arrive at the following observations and design guidelines:

  - When the values of the molecular absorption coefficient within the to-be-allocated spectrum can be modeled as an exponential function of frequency, the data rate obtained by the proposed unsupervised learning-based approach converges to that obtained from the design presented in Chapters 2 and 3.

  - When the values of the molecular absorption coefficient within the to-be-allocated spectrum change rapidly and thus cannot be modeled as an exponential function of frequency, the proposed unsupervised learning-based approach outperforms the existing approximate approaches.

  - The throughput of the spectrum allocation strategy decreases with the increasing density of human blockers. Thus, system parameters, e.g., power budget and maximum sub-band bandwidth, have to be carefully selected for achieving the desired throughput and reliability performance, depending on the density of human blockers in the indoor environment.

The main findings from this chapter have been or to be presented in the following publications [J4] and [C4]:

[J4]. **A. Shafie**, N. Yang, C. Li, X. Zhou, and T. Q. Duong, "Spectrum Allocation for Multiuser Terahertz Communication Systems: An Unsupervised Learning Approach", *submitted to IEEE J. Topics Signal Process.*, Dec. 2022

[C4]. **A. Shafie**, C. Li, N. Yang, X. Zhou, and T. Q. Duong, "An unsupervised learning approach for spectrum allocation in terahertz communication systems," in *Proc. IEEE Global Commun. Conf. (Globecom)*, Rio de Janeiro, Brazil, Dec. 2022, pp. 3447–3453 **(Best Paper Award)**.

Chapter 5 – Blockage and Coverage Analysis for 3D THzCom Systems

This chapter presents solutions to the design challenges outlined in Sections 1.2.5.1 and 1.2.6.1. Specifically, the chapter investigates (i) the modeling and analysis of different types of blockages in a 3D THzCom system and (ii) the coverage probability of an indoor THzCom system when frequency reuse is considered. To this end, we focus on an indoor THzCom environment where the downlink transmission of a user is impacted by different types of blockages, directional antennas, and interference from nearby transmitters.

The key contributions of this chapter are summarized as follows:

- We model the joint impact of blockages caused by the user itself, moving humans, and wall blockers in a 3D THzCom environment. Then, we derive the blockage probabilities associated with a point-to-point THzCom link. Also, we consider the effect of 3D directional antennas and derive the *hitting probability*, which is defined as the probability of the signal corresponding to the main lobe of an interferer reaching a user.

- We develop a tractable analytical framework, using stochastic geometry, to evaluate the coverage probability of 3D THzCom systems when frequency reuse is considered. Specifically, we derive an expression for the coverage probability, by characterizing the regions where dominant interferers (i.e., those that can cause outage by themselves) can exist, and the average number of interferers that exist in these regions.

- Using numerical investigation, we arrive at the following observations and design guidelines:

  - Our analysis well matches the simulations; thus, the proposed tractable analytical framework can be utilized to evaluate the coverage probability of the considered 3D THzCom system.

  - The network densification deteriorates the reliability of THzCom systems, and it is necessary to carefully select the AP densities to obtain

the desired reliability performance depending on the communication environment of interest.

- The vertical heights of the THz devices profoundly impact the coverage probability in THzCom systems; therefore, ignoring their impacts leads to a substantial underestimation of system reliability.
- An increase in the density of human blockers slightly improves the coverage probability when the transmission link of interest is in LoS, but reduces the overall coverage probability.

The findings from this chapter have been presented in the following publications [J1] and [C2]:

[J1]. **A. Shafie**, N. Yang, S. Durrani, X. Zhou, C. Han, and M. Juntti, "Coverage analysis for 3D terahertz communication systems," *IEEE J. Sel. Areas Commun.*, vol. 39, no. 6, pp. 1817–1832, June 2021.

[C2]. **A. Shafie**, N. Yang, Z. Sun, and S. Durrani, "Coverage analysis for 3D terahertz communication systems with blockage and directional antennas," in *Proc. IEEE Int. Conf. Commun. (ICC) Workshops*, Dublin, Ireland, June 2020, pp. 1–7.

Chapter 2

Spectrum Allocation with Adaptive Sub-band Bandwidth for THzCom Systems

2.1 Introduction

In this first technical chapter, we explore the benefits and the design of multi-band-based spectrum allocation with adaptive sub-band bandwidth (ASB) for terahertz (THz) band communication (THzCom) systems, by allowing to divide the to-be-allocated spectrum into sub-bands with unequal bandwidth. Due to the frequency- and distance-dependent nature of the molecular absorption loss, the variation in channel quality levels among the users that are assigned to sub-bands would be very high at the THz band when equal sub-band bandwidth (ESB) is considered as in the literature [32, 40, 45, 46, 51–54]. The consideration of ASB can significantly reduce this variation by allowing changes in the sub-band bandwidth, which leads to an overall improvement in the data rate performance.

We focus on a scenario where a single access point (AP) supports the downlink transmission of multiple users which demands high data rates. In this chapter, we consider the to-be-allocated spectrum exists entirely within a certain region of a transmission window (TW). For this system, we formulate an optimization problem, with the main emphasis on multi-band-based spectrum allocation with ASB,

while aiming to maximize the data rate under given constraints on sub-band bandwidth and power. This problem consists of the determination of the optimal sub-band bandwidth and transmit power. We then propose reasonable approximations, as well as transformations, and arrive at an approximate convex problem, which can be solved efficiently by using standard convex problem solvers. Aided by numerical results, we show that the proposed multi-band-based spectrum allocation with ASB achieves a significantly higher data rate compared to the multi-band-based spectrum allocation with ESB, due to the enhanced ASB capabilities. We also show that it is more beneficial to adopt ASB when the variation in molecular absorption loss within the to-be-allocated spectrum is high.

The rest of the chapter is organized as follows. Section 2.2 introduces the system model. Section 2.3 presents the resource allocation problem associated with the design of multi-band-based spectrum allocation with ASB. Section 2.4 presents the solution approach adopted to solve the formulated resource allocation problem. Section 2.5 presents the numerical results and Section 2.6 summarises the chapter.

2.2 System Model

In this section, we introduce the system model considered in this chapter. Specifically, we describe the system deployment, channel model, the THz spectrum, and the achievable data rate.

2.2.1 System Deployment

We consider a three-dimensional (3D) indoor THzCom system, as shown in Fig. 2.1, where a single access point (AP) supports the downlink transmission of n_{I} stationary users which demand high data rates. We consider that the AP is located at the center of the ceiling of the indoor environment of interest and model it to be of height h_{A}. We also consider that the users are stationary and distributed uniformly in this environment and are of heights h_{U}. Moreover, we assume that users in the system are equipped with tunable front-ends such that they can dynamically adjust their operating frequency and bandwidth to match those of their assigned sub-bands. We denote $\mathcal{I} = \{1, 2, \cdots, s, \cdots, n_{\mathrm{I}}\}$ as the set of the users and further

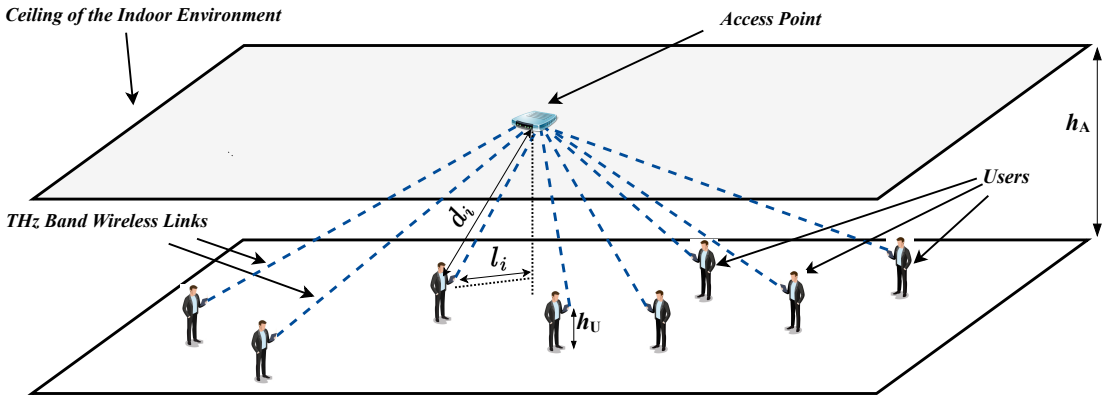

Figure 2.1: Illustration of the considered 3D multiuser THzCom system where a single AP supports the downlink transmission of multiple users.

denote l_i and $d_i = \sqrt{(h_{\mathrm{A}}-h_{\mathrm{U}})^2+l_i^2}$ as the horizontal and 3D distances between the AP and the ith user, respectively. For notational convenience, we consider that the elements in the set $\mathcal{I}$ are labeled such that $d_1 < d_2 < \cdots < d_{n_{\mathrm{I}}}$. Finally, we note that the impacts of blockages are ignored in this chapter.[1]

2.2.2 Channel Model

The signal propagation at the THz band is determined by the spreading loss and the molecular absorption loss. Considering this, the free space direct ray channel transfer function is obtained as [29][2]

$$H(f,d) = H_{\mathrm{spr}}(f,d)H_{\mathrm{abs}}(f,d), \tag{2.1}$$

where $H_{\mathrm{spr}}(f,d)$ and $H_{\mathrm{abs}}(f,d)$ represent the spreading loss and the molecular absorption loss, respectively, and are given by

$$H_{\mathrm{spr}}(f,d) = \frac{c}{4\pi f d}, \tag{2.2a}$$

[1]We clarify that despite the fact that the impacts of blockages are ignored in this chapter, the consideration of blockages can lead to a more accurate characterization of the considered THzCom system. Thus, in Chapters 4 and 5, we discuss in detail the impacts of different types of blockages on THzCom systems.

[2]In this thesis, we utilize the far field propagation model [29]. This is due to the fact that the transmission distances considered in this thesis are very high compared to the propagation wavelength of the THz signals.

$$H_{\text{abs}}(f,d) = e^{-k(f)d}. \tag{2.2b}$$

Here, c is the speed of light, f is the frequency, d is the communication distance, and $k(f)$ is the molecular absorption coefficient at f. We note that the molecular absorption loss is unique to the THz band and is the result of oxygen molecules and water vapor absorbing THz signal energies for their rotational transition energies.

For a given pressure-temperature-humidity setting, $k(f)$ can be found by using the HITRAN database [106], or the line by line radiative transfer model (LBLRTM) [107], or the International Telecommunication Union (ITU) model [108]. When the HITRAN database is utilized, the value of $k(f)$ is obtained from

$$k(f) = \frac{P}{P_{\text{STP}}} \frac{T_{\text{STP}}}{T} \sum_{\kappa,g} Q_1^{\kappa,g} Q_2^{\kappa,g}(f), \tag{2.3}$$

where P and T are the pressure and the temperature of the transmission environment, respectively, P_{STP} and T_{STP} are the standard pressure and temperature, respectively, and $Q_1^{\kappa,g}$ and $Q_2^{\kappa,g}(f)$ are the total number of molecules per unit volume and the absorption cross section for the isotopologue κ of gas g at the frequency f, respectively [29, 106].

2.2.3 THz Spectrum

2.2.3.1 Spectrum of Interest

As discussed in Chapter 1, the intermittent nature of $k(f)$ divides the entire THz band into multiple ultra-wideband TWs, as shown in Fig. 1.1. The entire spectrum regions that exist between neighboring $k(f)$ peaks are denoted by TWs [32]. In this chapter, we focus on the scenario where the to-be-allocated spectrum exists entirely in either a positive absorption coefficient slope region (PACSR) or a negative absorption coefficient slope region (NACSR) of a TW, as shown in Fig. 2.2. We note that PACSRs and NACSRs are defined as the spectrum regions within TWs where $k(f)$ shows an increasing and decreasing behavior, respectively, as shown in Fig. 2.2. We clarify that it is reasonable to focus on the allocation of the spectrum that exists either within a PACSR or an NACSR since the available bandwidths in each PACSR and NACSR at the THz band are in the order of tens up to hundreds

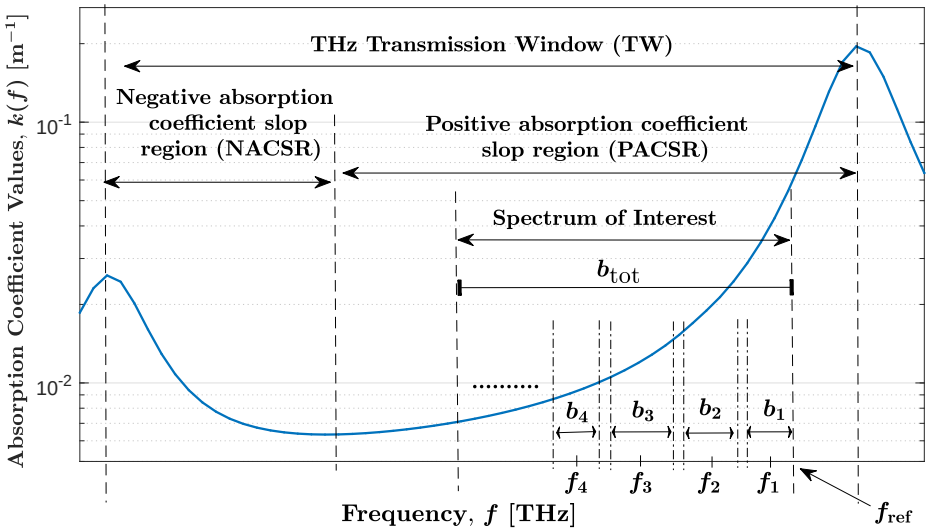

Figure 2.2: Illustration of the PACSR and the NACSR within a TW, and the arrangement of sub-bands within the PACSR.

of GHz, as shown in Table 2.1.[3]

We focus on multi-band-based spectrum allocation with ASB. Thus, we consider that the to-be-allocated spectrum is divided into sub-bands that are of unequal bandwidths. Also, we consider that these sub-bands are separated by guard bands [32, 46, 109]. We denote $\mathcal{S} = \{1, 2, \cdots, s, \cdots, n_{\text{S}}\}$ as the set of the sub-bands, where n_{S} is the total number of sub-bands. We further denote f_s and b_s as the center frequency and the bandwidth of the sth sub-band, respectively. For notational convenience, we consider that sub-bands in the set $\mathcal{S}$ are labeled such that $f_1 > f_2 > \cdots > f_{n_{\text{S}}}$, as shown in Fig. 2.2, if the to-be-allocated spectrum exists within a PACSR and $f_1 < f_2 < \cdots < f_{n_{\text{S}}}$ if the to-be-allocated spectrum exists within an NACSR. In this chapter, we optimally determine the value of b_s by solving the optimization problem that will be formulated in the subsequent section.

Since ASB is considered, we have

$$0 \leqslant b_s \leqslant b_{\max}, \qquad \forall s \in \mathcal{S}, \tag{2.4}$$

[3]We note that to fully harness the potential of the huge available bandwidths at the THz band, it would be more beneficial to focus on spectrum allocation when the to-be-allocated spectrum (i) exists anywhere within a TW and/or (ii) spans across multiple TWs. These considerations will be considered in Chapter 3.

Table 2.1: The PACSRs and NACSRs that exist within 0.32 THz and 1.1 THz and their bandwidths.

PACSR		**NACSR**	
Frequency Range (THz)	**Bandwidth (GHz)**	**Frequency Range (THz)**	**Bandwidth (GHz)**
$0.341 - 0.380$	39	$0.326 - 0.341$	15
$0.409 - 0.448$	39	$0.380 - 0.409$	29
$0.464 - 0.556$	92	$0.448 - 0.464$	16
$0.670 - 0.753$	83	$0.556 - 0.670$	114
$0.848 - 0.916$	68	$0.753 - 0.848$	95
$0.934 - 0.988$	54	$0.916 - 0.934$	18
$1.025 - 1.098$	73	$0.988 - 1.025$	37

where $b_{\max}$ denotes the upper bound on the sub-band bandwidth. We then denote B_{g} as the bandwidth of guard bands, which is considered to be fixed.[4] Considering this, we obtain

$$f_s = f_{\mathrm{ref}} - \eta \left(\sum_{\kappa=1}^{s} b_\kappa + (s-1)B_{\mathrm{g}} - \frac{b_s}{2} \right), \qquad \forall s \in \mathcal{S}, \tag{2.5}$$

where f_{ref} is the end-frequency of the to-be-allocated spectrum, as shown in Fig. 2.2, and $\eta = 1$ if the to-be-allocated spectrum exists within a PACSR, and f_{ref} is the start-frequency of the to-be-allocated spectrum and $\eta = -1$ if the to-be-allocated spectrum exists within an NACSR. Finally, we denote b_{tot} as the total available bandwidth within the to-be-allocated spectrum, and obtain it as

$$b_{\mathrm{tot}} = \sum_{s \in \mathcal{S}} b_s + (n_{\mathrm{S}} - 1)\, B_{\mathrm{g}}. \tag{2.6}$$

[4]To further improve the spectral efficiency, it may be beneficial to optimally design the values of B_{g}, instead of considering fixed and pre-defined values for B_{g}. When B_{g} is to be optimally designed, the impacts of intra-band interference (Intra-BI), interference cancelation capabilities of the users, quality-of-service (QoS) requirements of the users such as tolerable interference and required data rate, and the spectral efficiency of the system needs to be jointly considered. However, we note that designing the values of B_{g} is beyond the scope of this thesis, but will be considered in our future works.

2.2.3.2 Sub-band Assignment Strategy

In the considered system, we assume that the users in the system are served by separate sub-bands, which is also adopted in [32, 46, 50].[5] This assumption is made to (i) ensure the data transmission is free of Intra-BI and (i) eliminate the signal processing overhead and hardware complexity caused by frequency reuse in the system. Considering this assumption, we set the total number of sub-bands within the to-be-allocated spectrum to be equal to the total number of users in the system, i.e., $n_{\mathrm{S}} = n_{\mathrm{I}}$.

The distance-aware multi-carrier (DAMC)-based sub-band assignment was proposed in [46] to improve the throughput fairness among users in multiuser THzCom systems. The DAMC-based sub-band assignment assigns (i) the sub-bands with high absorption coefficients, $k(f)$, to the users with shorter distances and (ii) the sub-bands with low $k(f)$ to the users with longer distances. Following [32, 51, 52], is this chapter we adopt DAMC-based sub-band assignment.[6] In the considered to-be-allocated spectrum, we have $k(f_s) > k(f_{s+1}),\ \forall s \in \mathcal{S}$, irrespective of whether the to-be-allocated spectrum exists within a PACSR or an NACSR. Also, users are labeled in the ascending order of their distance to the APs in the set $\mathcal{I}$, i.e., $d_1 < d_2 < \cdots < d_{n_{\mathrm{I}}}$. Considering these, in order to assign sub-bands to users as per the DAMC principle, we assign the sth sub-band in the to-be-allocated spectrum to the sth user in the set $\mathcal{I}$.

2.2.4 Achievable Data Rate

Considering Shannon's capacity theorem [28], the data rate achieved by the user assigned to the sth sub-band is obtained as an integral of capacity on frequency,

[5] A higher spectral efficiency can be achieved by leveraging sub-band reuse during spectrum allocation. The consideration of frequency reuse and its impact on Intra-BI and reliability performance of THzCom systems will be discussed in Chapter 5.

[6] We will investigate the optimal sub-band assignment for multiuser THzCom systems and the optimality of DAMC-based sub-band assignment in Chapter 3.

given by

$$r_s = \int_{f_s-\frac{1}{2}b_s}^{f_s+\frac{1}{2}b_s} C(f)\ \mathrm{d}f$$
$$= \int_{f_{\mathrm{ref}}-\eta\left(\sum_{\kappa=1}^{s} b_\kappa+(s-1)B_{\mathrm{g}}-b_s\right)}^{f_{\mathrm{ref}}-\eta\left(\sum_{\kappa=1}^{s} b_\kappa+(s-1)B_{\mathrm{g}}\right)} \log_2\left(1+\frac{p_s G_{\mathrm{A}} G_{\mathrm{U}} |H(f,d_s)|^2}{N_0 b_s + \mathcal{I}_{\mathrm{agg},s}}\right)\mathrm{d}f, \qquad \forall s \in \mathcal{S}, \tag{2.7}$$

where $C(f)$ is the capacity when the frequency is f, p_s is the transmit power allocated by the AP to the user assigned to sub-band s, G_{A} and G_{U} are the antenna gains at the AP and users, respectively, f is the frequency, N_0 is the noise power density, $H(f,d)$ is given by (2.1), and $\mathcal{I}_{\mathrm{agg},s}$ is the interference experienced by the user assigned to the sth sub-band.

We note that any surface that has roughness comparable to the wavelength of the electromagnetic wave introduces high reflection, diffraction, and scattering losses. Due to this and the fact that the wavelength of THz signals is extremely low, surfaces that are considered smooth at lower frequencies become rough at the THz band, thereby causing high reflection, diffraction, and scattering losses at the THz band [34,46]. These lead to (i) the reduced number of significant non-line-of-sight (nLoS) rays that constitute a THz signal and (ii) the substantial attenuation of significant nLoS rays as compared to the line-of-sight (LoS) ray. Thus, similar to [62,69,72,73,75,86–88], we ignore the impact of nLoS rays and focus only on the LoS rays of THz signals.[7] Also, we omit the impact of fading in the THz channel as previous studies at the THz band [62, 69, 72–75, 86–88, 113].

The interference experienced by the user assigned to the sth sub-band, $\mathcal{I}_{\mathrm{agg},s}$, is obtained as the addition of the inter-band interference (Inter-BI) and Intra-BI. The Inter-BI at the THz band is caused by the power leakage from adjacent sub-bands,

[7]Despite our consideration of ignoring the impact of nLoS rays, there have been some recent studies on THzCom systems that leverage the strong reflections or even scattering to establish links, with certain reliability [110–112]. Thus, it may be beneficial to consider the impact of nLoS rays in certain scenarios at the THz band, e.g., when the LoS rays are totally blocked by blockers. This consideration is beyond the scope of this thesis, but will be considered in our future works.

due to harmonics generated in frequency multiplying chains during frequency up-shifting. Recently, Inter-BI suppression schemes that can suppress Inter-BI with minimal throughput degradation [68] and waveform designs that minimize power leakages to adjacent bands [69] were proposed. Due to these and the existence of guard bands between consecutive sub-bands in our spectrum allocation strategy, the impact of Inter-BI is not considered in this chapter [50, 114]. Also, we note that Intra-BI at the THz band is caused due to multiple users sharing the same sub-band. In this chapter, we assume that the users in the system are served by separate sub-bands. This assumption ensures Intra-BI-free data transmission[8]. These considerations allow us to set $\mathcal{I}_{\text{agg},s}$ in (2.7) to be zero, i.e., $\mathcal{I}_{\text{agg},s} = 0,\ \forall s \in \mathcal{S}$[9].

2.3 Optimal Resource Allocation

In this section, we present the resource allocation problem. It is of utmost importance to design novel and efficient spectrum allocation strategies to harness the potential of the THz band. With this in mind, we study a resource allocation problem for the considered multiuser THzCom system with the main emphasis on spectrum allocation with ASB. Particularly, we aim to maximize the achievable data rate under given constraints on sub-band bandwidth and power. This problem consists of sub-band bandwidth allocation and power control. Mathematically, the problem is formulated as

$$
\begin{aligned}
\mathbf{P_1^o}: \quad & \underset{p_s, b_s, \forall s \in \mathcal{S}}{\text{maximize}} \quad \mathcal{E}(r_1, r_2, \cdots, r_{n_{\text{S}}}) && && \text{(2.8a)}\\
& \text{subject to} \quad \sum_{s \in \mathcal{S}} p_s \leqslant p_{\text{tot}}, && && \text{(2.8b)}\\
& \qquad\qquad 0 \leqslant p_s \leqslant p_{\max}, && \forall s \in \mathcal{S}, && \text{(2.8c)}\\
& \qquad\qquad \sum_{s \in \mathcal{S}} b_s = \bar{b}_{\text{tot}}, && && \text{(2.8d)}\\
& \qquad\qquad 0 \leqslant b_s \leqslant b_{\max}, && \forall s \in \mathcal{S}. && \text{(2.8e)}
\end{aligned}
$$

[8] We will discuss the consideration of frequency reuse and Intra-BI, and their impacts on the reliability performance of THzCom systems in Chapter 5.

[9] Consideration of nLoS rays, fading, blockages, and Inter-BI can lead to a more accurate characterization of the considered THzCom system, which will be considered in our future works.

In $\mathbf{P_1^o}$, $\mathcal{E}(r_1, r_2, \cdots, r_{n_\mathrm{S}})$ is the objective function imposed by the considered data rate maximization strategy, which will be discussed in the next subsection. Moreover, (2.8b) reflects the power budget at the AP and (2.8c) ensures that the power allocated to each user is upper bounded by $p_{\max}$. Furthermore, the justifications of (2.8d) and (2.8e) are given in (2.6) and (2.4), respectively, and $\overline{b}_{\mathrm{tot}}$ in (2.8d) is given by $\overline{b}_{\mathrm{tot}} = b_{\mathrm{tot}} - (n_\mathrm{S} - 1)\, B_\mathrm{g}$. We assume that the distances between the AP and all users are readily available at the AP, such that AP can optimally determine the power and bandwidth to be allocated to each user by solving $\mathbf{P_1^o}$. We note that the AP can estimate the distances between the AP and all users by using the channel state information (CSI) of AP to all user links at a predefined frequency and the value of $k(f)$ at this predefined frequency.

The novelty of the considered resource allocation problem, $\mathbf{P_1^o}$, is as follows: In $\mathbf{P_1^o}$, we propose spectrum allocation with ASB, while to the best of our knowledge, recent studies in THz band spectrum allocation have only considered ESB [32, 46, 50–54]. In Section 2.5, we show the significance of this consideration using numerical results.

2.3.1 Objective Function

Depending on the application scenario and the QoS requirements of the system and users, three system objectives can be considered, namely, (i) max-min rate maximization, (ii) sum rate maximization, and (iii) proportional-fair rate maximization. In what follows, we discuss each of these system objectives.

2.3.1.1 Max-min Rate Maximization

The max-min rate maximization objective aims to prioritize fairness among users over the system performance. It attempts to guarantee strict rate fairness among users while maximizing the overall system rate performance. For the max-min rate maximization objective, the objective function, $\mathcal{E}(r_1, r_2, \cdots, r_{n_\mathrm{S}})$ is $\mathcal{E}(r_1, r_2, \cdots, r_{n_\mathrm{S}}) = \min\limits_{s\in\mathcal{S}}\{r_s\}$, and (2.8) becomes

$$\mathbf{P^o_{1,MM}}: \quad \underset{p_s, b_s, \forall s\in\mathcal{S}}{\text{maximize}} \quad \min_{s\in\mathcal{S}}\{r_s\}$$

$$\text{subject to} \quad (2.8\text{b}) - (2.8\text{e}). \tag{2.9}$$

2.3.1.2 Sum Rate Maximization

The sum rate maximization objective aims to prioritize the system rate efficiency over fairness among users. It attempts to achieve maximum spectral efficiency performance by fully exploiting ASB and power control. For sum rate maximization objective, $\mathcal{E}(r_1, r_2, \cdots, r_{n_\mathrm{S}}) = \sum_{s\in\mathcal{S}} r_s$ and (2.8) becomes

$$\begin{aligned} \mathbf{P^o_{1,SM}}: \quad & \underset{p_s, b_s, \forall s\in\mathcal{S}}{\text{maximize}} \quad \sum_{s\in\mathcal{S}} r_s \\ & \text{subject to} \quad (2.8\text{b}) - (2.8\text{e}). \end{aligned} \tag{2.10}$$

2.3.1.3 Proportional-fair Rate Maximization

The proportional-fair rate maximization objective aims to strike a balance between the system rate efficiency and rate fairness among the users. This objective achieves a certain level of fairness among users by providing each user with a performance that is proportional to its channel conditions. For the proportional-fair rate maximization objective, $\mathcal{E}(r_1, r_2, \cdots, r_{n_\mathrm{S}}) = \sum_{s\in\mathcal{S}} \log(r_s)$ and (2.8) becomes

$$\begin{aligned} \mathbf{P^o_{1,PF}}: \quad & \underset{p_s, b_s, \forall s\in\mathcal{S}}{\text{maximize}} \quad \sum_{s\in\mathcal{S}} \log(r_s) \\ & \text{subject to} \quad (2.8\text{b}) - (2.8\text{e}). \end{aligned} \tag{2.11}$$

Without loss of generality, we consider the max-min rate maximization objective in this chapter. The sum rate and the proportional-fair rate maximization objectives will be considered in the resource allocation problems that would be discussed in Chapters 3 and 4, respectively.

2.4 Solution Approach

In this section, we present the solution adopted to solve the formulated optimization problem $\mathbf{P^o_1}$. We note that it is extremely challenging to solve $\mathbf{P^o_1}$ in its current

form due to the difficulty in obtaining the data rate, r_s, as a tractable expression of the design variable b_ν, $\forall\ s, \nu \in \mathcal{S}$. On one hand, obtaining r_s as per (2.7) involves an integral and the limits of the integral depend on b_ν, $\forall\ s, \nu \in \mathcal{S}$. On the other hand, the values of molecular absorption coefficient, $k(f)$, for all frequencies within the to-be-allocated spectrum are required to obtain r_s, $\forall s \in \mathcal{S}$. Although $k(f)$ can be found by using the HITRAN database [106], LBLRTM [107], or the ITU model [108], there does not exist a tractable expression that maps f to $k(f)$. This implies that it is extremely difficult, if not impossible, to analytically solve $\mathbf{P_1^o}$ in its current form using the traditional optimization theory techniques [55]. Therefore, we need to render the problem $\mathbf{P_1^o}$ computationally tractable. Considering this, we make two reasonable modifications which enable us to obtain r_s using a tractable expression of the design variables b_ν, $\forall\ s, \nu \in \mathcal{S}$. We discuss the modifications in the next subsection.

2.4.1 Problem Reformulation

We first tackle the intractability caused by the lack of tractable expression for $k(f)$. To this end, we first obtain the values of $k(f)$ for all the values of f in the to-be-allocated spectrum and observe the behavior of its variation. We notice that the variation of $k(f)$ in the spectra that exist fully within PACSRs and NACSRs exhibits the behavior of an exponential function of f (see Fig. 2.2). Considering this, through curve fitting, we model $k(f)$ in the to-be-allocated spectrum using an exponential function of f, given by

$$\widehat{k}(f) = e^{\sigma_1 + \sigma_2 f} + \sigma_3, \tag{2.12}$$

where $\min\{f_{\text{ref}}, f_{\text{ref}} - \eta b_{\text{tot}}\} \leqslant f \leqslant \max\{f_{\text{ref}}, f_{\text{ref}} - \eta b_{\text{tot}}\}$, $r \in \mathcal{R}$, $\widehat{k}(f)$ is the approximated molecular absorption coefficient at f, and $\{\sigma_1, \sigma_2, \sigma_3\}$ are the model parameters obtained for the to-be-allocated spectrum. We note that there indeed exist many spectrum regions within the PACSRs and NACSRs where $k(f)$ can be modeled as an exponential function of frequency, e.g., the PACSR between 0.670 THz and 0.720 THz, where the maximum modeling approximation error is 0.47%. In Section 2.5, we discuss the approximation accuracy of the model for different spectral regions within the THz band through numerical results.

Utilizing the aforementioned modification, we obtain r_s in (2.7) as

$$r_s = \int_{f_s-\frac{1}{2}b_s}^{f_s+\frac{1}{2}b_s} C(f)\ \mathrm{d}f = \int_{f_s-\frac{1}{2}b_s}^{f_s+\frac{1}{2}b_s} \log_2\left(1+\frac{p_s\varrho e^{-d_s\left(e^{\sigma_1+\sigma_2 f}+\sigma_3\right)}}{f^2 d_s^2 b_s}\right)\mathrm{d}f, \tag{2.13}$$

where $\varrho = \frac{G_\mathrm{A}G_\mathrm{U}}{N_0}\left(\frac{c}{4\pi}\right)^2$, and $f_s = f_\mathrm{ref} - \eta\left(\sum_{\kappa\in\mathcal{S}} a_{s,\kappa}b_\kappa + (s-1)B_\mathrm{g}\right)$ with $a_{s,\kappa}$=1, if $\kappa < s$, $a_{s,\kappa}$=0.5, if κ=s, $a_{1,s,\kappa}$=0, otherwise, $\forall s, \kappa \in \mathbb{Z}^+$.

Second, we tackle the obstacle caused by obtaining r_s as in (2.13) using an integral. We observe that $C(f)$ in (2.13) is frequency selective within the entire to-be-allocated spectrum, as well as within each sub-band, since $k(f)$ is frequency selective. Despite this, we observe that $C(f)$ within the PACSR (or the NACSR) decreases (or increases) monotonically with frequency when $k(f)$ behaves according to (2.12). Although the monotonic decrease (or increase) in $C(f)$ cannot be approximated for the whole PACSR using a linear function of frequency, it can be approximated using a piecewise linear function of frequency with each sub-band modeled by a linear piece. This approximation allows to modify r_s in (2.13) as

$$\widehat{r}_s = \frac{b_s}{2}\left(C\left(f_s-\frac{b_s}{2}\right)+C\left(f_s+\frac{b_s}{2}\right)\right), \qquad \forall s\in\mathcal{S}, \tag{2.14}$$

and consider

$$\left(C\left(f_s-\frac{b_s}{2}\right)+C\left(f_s+\frac{b_s}{2}\right)\right) \approx 2C(f_s), \quad \forall s\in\mathcal{S}, \tag{2.15}$$

where $\widehat{r}_s$ in (2.14) is the approximate of r_s. Thereafter, substituting (2.15) into (2.14), we obtain the following tractable expression for rate, given by

$$\widehat{r}_s = b_s\log_2\left(1+\frac{p_s\varrho e^{-d_s\left(e^{\sigma_1+\sigma_2\left(f_\mathrm{ref}-\eta\left(\sum_{\kappa\in\mathcal{S}} a_{s,\kappa}b_\kappa+(s-1)B_\mathrm{g}\right)\right)}+\sigma_3\right)}}{\left(f_\mathrm{ref}-\eta\left(\sum_{\kappa\in\mathcal{S}} a_{s,\kappa}b_\kappa+(s-1)B_\mathrm{g}\right)\right)^2 d_s^2 b_s}\right), \qquad \forall s\in\mathcal{S}. \tag{2.16}$$

We clarify that for tractable system designs, several previous THz band studies such as [72,73,87–89] have adopted the expression in which the rate is not presented as an integral of frequency. In Section 2.5, we discuss the accuracy of this simplification through numerical results.

Utilizing the aforementioned modifications, the problem $\mathbf{P_1^o}$ in (2.8) is transformed into a tractable optimization problem, given by

$$\begin{aligned} \widehat{\mathbf{P}}_{\mathbf{1}}^{\mathbf{o}}: \quad & \underset{p_s, b_s, \forall s \in \mathcal{S}}{\text{maximize}} \quad \min_{s \in \mathcal{S}} \{\widehat{r}_s\} \\ & \text{subject to} \quad (2.8\text{b}) - (2.8\text{e}). \end{aligned} \tag{2.17}$$

2.4.2 Convex Optimization-based Solution

After the aforementioned modifications, although $\widehat{\mathbf{P}}_{\mathbf{1}}^{\mathbf{o}}$ in (2.17) is tractable, it is non-convex in its current form. In particular, the non-convexity in $\widehat{\mathbf{P}}_{\mathbf{1}}^{\mathbf{o}}$ arises due to two reasons. First, r_s in the objective function in $\widehat{\mathbf{P}}_{\mathbf{1}}^{\mathbf{o}}$ is not differentiable at $b_s = 0$, $\forall\ s \in \mathcal{S}$. Second, the objective function in $\widehat{\mathbf{P}}_{\mathbf{1}}^{\mathbf{o}}$ is non-convex with respect to (w.r.t.) the design variable b_ν, since r_s is not concave w.r.t. b_ν, $\forall\ s, \nu \in \mathcal{S}$. We next tackle these challenges as follows:

We first handle the non-differentiability of r_s at $b_s = 0$. To this end, we consider that b_s, $\forall s \in \mathcal{S}$, is lower bounded by a very small positive number [115]. In doing so, we transform $\widehat{\mathbf{P}}_{\mathbf{1}}^{\mathbf{o}}$ into the following problem, given by

$$\begin{aligned} \widetilde{\mathbf{P}}_{\mathbf{1}}^{\mathbf{o}}: \quad & \underset{p_s, b_s, \forall s}{\text{minimize}} \quad \max_{s \in \mathcal{S}} \{-r_s\} && \text{(2.18a)} \\ & \text{subject to} \quad (2.8\text{b}) - (2.8\text{d}), \\ & \qquad\qquad \delta_{\text{B}} \leqslant b_s \leqslant b_{\max}, \qquad \forall s \in \mathcal{S}, && \text{(2.18b)} \end{aligned}$$

where δ_{B} is a very small positive number. We note that the optimal value of $\widetilde{\mathbf{P}}_{\mathbf{1}}^{\mathbf{o}}$ converges to the optimal value of $\widehat{\mathbf{P}}_{\mathbf{1}}^{\mathbf{o}}$ when $\delta_{\text{B}} \to 0^+$, i.e., $\lim_{\delta_{\text{B}} \to 0^+} \widetilde{\mathbf{P}}_{\mathbf{1}}^{\mathbf{o}} = \widehat{\mathbf{P}}_{\mathbf{1}}^{\mathbf{o}}$ [55,115].

We next handle the non-concavity of r_s w.r.t. b_ν, $\forall\ s, \nu \in \mathcal{S}$. For this purpose, we seek substitutions for b_ν that would guarantee the concavity of r_s w.r.t. the new design variable that would replace b_ν. With this in mind, through careful inspection, we arrive at the following Lemma.

Lemma 2.1 *When the substitution for b_ν, given by $b_\nu = \xi_\nu + \omega_\nu \log(\varsigma_\nu z_\nu)$, is considered, $\widehat{r}_s$ becomes concave w.r.t. z_ν, $\forall s, \nu \in \mathcal{S}$. Here, $\xi_\nu, \omega_\nu, \varsigma_\nu$ are real constants and $1/\omega_\nu > \overline{\omega}$, where $\overline{\omega} = |\sigma_2| \left(\widehat{d}_{\max} \widehat{k}(f_{ref}) e^{\widehat{d}_{\max}\sigma_3} - 1 \right)$, $\widehat{d}_{\max} > d_{n_\mathrm{I}}$ [116].*

Proof: See Appendix A.1. ■

Following Lemma 2.1, we consider the following substitution for b_s, given by

$$b_s = \xi_s + \omega_s \log(\varsigma_s z_s), \quad \forall s \in \mathcal{S}, \tag{2.19}$$

where z_s is the new design variable that would replace b_s in the optimization problem, $\xi_s, \omega_s, \varsigma_s$ are real constants, and

$$1/\omega_s > \overline{\omega}, \quad \forall s \in \mathcal{S}, \tag{2.20}$$

where $\overline{\omega} = |\sigma_2| \left(\widehat{d}_{\max} \widehat{k}(f_{\mathrm{ref}}) e^{\widehat{d}_{\max}\sigma_3} - 1 \right)$ and $\widehat{d}_{\max} > d_{n_\mathrm{I}}$.Thereafter, substituting (2.19) into (2.16), we obtain

$$\widehat{r}_s = (\xi_s + \omega_s \log(\varsigma_s z_s)) \log_2 \left(1 + \frac{p_s \varrho e^{-d_s \left(e^{\sigma_1 + \sigma_2 f_s} + \sigma_3 \right)}}{f_s^2 d_s^2 (\xi_s + \omega_s \log(\varsigma_s z_s))} \right), \tag{2.21}$$

where

$$f_s = f_{\mathrm{ref}} - \eta \left(\sum_{\kappa \in \mathcal{S}} a_{s,\kappa} \left(\xi_\kappa + \omega_\kappa \log(\varsigma_\kappa z_\kappa) \right) + (s-1) B_{\mathrm{g}} \right). \tag{2.22}$$

We clarify that for any selected combination of real values for $\xi_s, \omega_s, \varsigma_s$, the feasible region of the term $\xi_s + \omega_s \log(\varsigma_s z_s)$ is the real domain, as long as z_s takes real values. Thus, the constraint introduced on ω_s in (2.20), does not add any restriction on the domain of the problem $\widetilde{\mathbf{P}}_\mathbf{1}^\mathbf{o}$.

After this substitution, we transform $\widetilde{\mathbf{P}}_\mathbf{1}^\mathbf{o}$ into the following equivalent problem, given by

$$\mathbf{P}_\mathbf{1F}^\mathbf{o}: \quad \underset{p_s, z_s, \forall s}{\text{minimize}} \quad \max_{s \in \mathcal{S}} \{-\widehat{r}_s\} \tag{2.23a}$$

$$\text{subject to} \quad \sum_{s \in \mathcal{S}} p_s \leqslant p_{\mathrm{tot}}, \tag{2.23b}$$

$$0 \leqslant p_s \leqslant p_{\max}, \quad \forall s \in \mathcal{S}, \tag{2.23c}$$

$$\prod_{s\in\mathcal{S}} z_s^{\omega_s} - \prod_{s\in\mathcal{S}} \varsigma_s^{-\omega_s} e^{\bar{b}_{\text{tot}} - \sum\limits_{s\in\mathcal{S}} \xi_s} \leqslant 0, \tag{2.23d}$$

$$z_{\min,s} \leqslant z_s \leqslant z_{\max,s}, \qquad \forall s \in \mathcal{S}, \tag{2.23e}$$

where $z_{\min,s} = \frac{1}{\varsigma_s} e^{\frac{\delta_{\text{B}} - \xi_s}{\omega_s}}$ and $z_{\max,s} = \frac{1}{\varsigma_s} e^{\frac{b_{\max} - \xi_s}{\omega_s}}$. We note that (2.23d) and (2.23e) are obtained by substituting (2.19) into (2.8d) and (2.18b), respectively. Finally, we note that after these modifications and transformations, $\mathbf{P^o_{1F}}$ is obtained as a standard convex optimization problem [55]. Thus, $\mathbf{P^o_{1F}}$ can be solved efficiently by using standard convex problem solvers [56, 117].

Complexity of the solution to $\mathbf{P^o_{1F}}$: We clarify that $\mathbf{P^o_{1F}}$ is solved using standard convex problem solvers with polynomial computational complexity. There are totally $n_{\text{D}} = 2n_{\text{I}}$ decision variables and $n_{\text{C}} = 2n_{\text{I}} + 2$ linear constraints in the convex problem $\mathbf{P^o_{1F}}$. Thus, solving $\mathbf{P^o_{1F}}$ requires a complexity of $\mathcal{O}\Big(n_{\text{D}}^3 n_{\text{C}}\Big) \approx \mathcal{O}\Big(n_{\text{I}}^4\Big)$ [118].

2.5 Numerical Results

2.5.1 Validation of the Modifications Introduced in Chapter 2.4.1

In this section, we examine the correctness of the two modifications introduced in Section 2.4.1 to obtain the data rate, r_s, using a tractable expression of the design variable b_ν, $\forall\ s, \nu \in \mathcal{S}$. We recall that in the first modification, the molecular absorption coefficient, $k(f)$, in the to-be-allocated spectrum is modeled using an exponential function of f, as in (2.12). In the second modification, the expression in (2.13), where the rate is obtained as an integral on frequency, is simplified into (2.16), where the rate is not presented as an integral of frequency.

In Table 2.2, we present the exponential model parameters and the accuracy of the model for different spectrum regions within the THz band. Some of the PACSRs and NACSRs given in Table 2.1 and the spectrum regions that exist within those PACSRs/NACSRs are examined. For clarity, we denote the PACSRs and the NACSRs as $\text{sr}_1^{\text{p}}, \text{sr}_2^{\text{p}}, \cdots$ and $\text{sr}_1^{\text{n}}, \text{sr}_2^{\text{n}}, \cdots$, respectively. We use the $k(f)$ values that

Table 2.2: Illustration of the exponential model parameters and the accuracy of the exponential model for different spectral regions within the THz band.

Spectrum Region	Frequencies (THz)	Band--width	σ_1	σ_2 $[10^{-10}]$	σ_3	Average approx--imation error %	Maximum of the app--roximation error %
PACSRs							
sr_1^p	0.341 - 0.380	39	-103.22	2.67	0.01	8.97	17.84
within sr_1^p	0.341 - 0.371	30	-64.86	1.64	0.01	1.79	3.49
within sr_1^p	0.341 - 0.361	20	-48.73	1.20	0.01	0.14	0.59
sr_2^p	0.409 - 0.448	39	-103.50	2.28	0.01	9.62	21.55
within sr_2^p	0.409 - 0.434	25	-43.16	0.89	0.01	3.15	10.81
within sr_2^p	0.409 - 0.425	16	-117.42	2.64	0.01	0.48	2.17
sr_3^p	0.464 - 0.556	92	-125.01	2.29	0.08	60.63	189.51
within sr_3^p	0.484 - 0.556	72	-125.76	2.30	0.10	56.85	183.71
within sr_3^p	0.484 - 0.544	60	-70.03	1.28	0.05	12.85	42.95
sr_4^p	0.670 - 0.753	83	-147.32	1.98	0.05	20.08	43.62
within sr_4^p	0.670 - 0.740	70	-89.18	1.19	0.05	7.98	17.90
within sr_4^p	0.670 - 0.730	60	-61.49	0.82	0.04	1.54	2.74
within sr_4^p	0.670 - 0.720	50	-52.95	0.70	0.04	0.24	0.47
NACSRs							
sr_1^n	0.326 - 0.341	15	117.10	-3.71	0.01	0.21	0.69
within sr_1^n	0.331 - 0.341	10	115.79	-3.67	0.01	0.12	0.36
sr_2^n	0.380 - 0.409	29	111.48	-2.97	0.01	3.60	6.27
within sr_3^n	0.389 - 0.409	20	80.47	-2.17	0.01	0.23	0.41
sr_3^n	0.448 - 0.464	16	156.12	-3.51	0.03	1.26	2.89
sr_4^n	0.556 - 0.670	114	129.01	-2.27	0.10	49.43	120.57
within sr_4^n	0.580 - 0.670	90	21.53	-0.40	0.04	17.97	62.27
within sr_4^n	0.556 - 0.611	55	130.60	-2.30	0.14	24.37	68.44

are calculated using the ITU model for the ambient temperature, atmospheric pressure, and atmospheric water vapor density of 15° C, 101.30 kPa, and 7.5 g/m^3, respectively. Also, we use the non-linear regression model available in Matlab to fit the $k(f)$ values to the exponential model.

We first observe that the exponential model parameter σ_2 is $\sigma_2 > 0$ when

the to-be-allocated spectrum exists within a PACSR and $\sigma_2 < 0$ when the to-be-allocated spectrum exists within an NACSR. This is expected since we consider PACSRs and NACSRs as the spectrum regions within TWs where $k(f)$ shows an increasing and decreasing behavior, respectively. Second, we observe that in many PACSRs/NACSRs within the THz band, such as sr_1^{n}, sr_2^{n}, and sr_3^{n}, $k(f)$ within the whole PACSRs/NACSRs can be approximated using the exponential model with ignorably small approximation errors. Third, we observe that in several other PACSRs/NACSRs within the THz band, such as sr_1^{p}, sr_2^{p}, and sr_4^{p}, $k(f)$ within the whole PACSRs/NACSRs can only be approximated with reasonable approximation errors. However, in spectrum regions within those PACSRs/NACSRs, $k(f)$ can be modeled with ignorably small approximation errors. Fourth, we observe that in several other PACSRs/NACSRs within the THz band, such as sr_3^{p} and sr_4^{n}, as well as in spectrum regions within those PACSRs/NACSRs, $k(f)$ cannot be modeled using the exponential model with reasonable approximation errors.

Based on these observations, we make several important conclusions. Specifically, based on the second and third observations, we conclude that there indeed exist many spectrum regions within the THz band where $k(f)$ can be modeled as an exponential function of frequency, and within those spectrum regions modification introduced in (2.12) is valid. Based on the fourth observation, we conclude that there exists a reasonable number of spectrum regions within the THz band where the variation of $k(f)$ is not simple such that it can be modeled as an exponential function of frequency. In such regions, the modification introduced in (2.12) is not valid and the spectrum allocation design introduced in this chapter cannot be applied to obtain the near-optimal solution to the spectrum allocation problem with ASB. Hence, emerging optimization techniques such as machine learning (ML) might need to be explored in such spectrum regions to attain near-optimal solutions. This consideration will be discussed in Chapter 4.

Next, to demonstrate the correctness of the rate simplification introduced in (2.16), in Table 2.3, we present the values of r_s obtained based on (2.13) and (2.16) within two NACSRs. We clarify that, on one hand, the values of Part A of Table 2.3 are obtained in the NACSR that exists between 0.753 THz and 0.848 THz, where $k(f)$ can be modeled as an exponential function of frequency with minimum approximation errors. On the other hand, the values of Part B of Table 2.3 are

Table 2.3: Illustration of the approximation error associated with the rate simplification introduced in (2.16).

Part A: Values obtained in the NACSR that exists between 0.753 and 0.848 THz						
Center Frequency of sub-band [THz]	0.810	0.783	0.773	0.778	0.797	0.801
Bandwidth of sub-band [GHz]	2.62	4.86	4.94	4.91	4.07	3.45
Rate without simplification [Gbps]	1.73	5.56	5.03	6.06	5.11	3.70
Rate with simplification [Gbps]	1.72	5.55	5.02	6.01	5.17	3.74
Approximation error [%]	0.20	0.29	0.17	0.86	1.01	0.97
Center Frequency of sub-band [THz]	0.816	0.818	0.820	0.812	0.814	0.783
Bandwidth of sub-band [GHz]	1.96	1.77	1.64	2.31	2.08	4.86
Rate without simplification [Gbps]	1.46	1.31	1.19	1.67	1.55	5.56
Rate with simplification [Gbps]	1.43	1.28	1.16	1.66	1.53	5.55
Approximation error [%]	1.83	2.45	3.00	0.86	1.35	0.86
Part B: Values obtained in the NACSR that exists between 0.556 and 0.670 THz						
Center Frequency of sub-band [THz]	0.646	0.622	0.612	0.617	0.634	0.637
Bandwidth of sub-band[GHz]	2.74	4.89	4.88	4.91	3.28	3.01
Rate without simplification [Gbps]	2.86	10.67	19.14	13.47	6.92	6.72
Rate with simplification [Gbps]	2.39	11.60	18.18	13.47	5.81	5.78
Approximation error [%]	19.43	8.01	5.30	0.03	19.02	16.35
Center Frequency of sub-band [THz]	0.64	0.653	0.656	0.658	0.648	0.651
Bandwidth of sub-band[GHz]	2.94	2.39	2.35	2.26	2.51	2.40
Rate without simplification [Gbps]	5.09	1.76	1.68	1.52	2.16	2.03
Rate with simplification [Gbps]	4.36	1.57	1.55	1.42	1.81	1.76
Approximation error [%]	16.77	12.20	8.06	6.81	19.65	15.7

obtained in the NACSR that exists between 0.556 THz and 0.67 THz, i.e., $\mathrm{sr}_4^{\mathrm{n}}$ as given in Table 2.2, where $k(f)$ cannot be modeled as an exponential function of frequency with minimum approximation errors. First, we observe that from Part A of Table 2.3 that when $k(f)$ can be modeled as an exponential function of frequency, the approximation error due to the rate simplification introduced in (2.16) is ignorably small and the considered simplification is reasonable. This validates our rate simplification introduced in (2.16). Based on this and the observation in Table 2.2, we conclude that *when $k(f)$ can be modeled as an exponential function of frequency with reasonable approximation accuracy, the spectrum allocation design introduced in this chapter can be utilized to obtain the solution to the spectrum*

allocation problem with ASB. Finally, from Part B of Table 2.3 we observe that when $k(f)$ cannot be modeled as an exponential function of frequency, the rate simplification introduced in (2.16) cannot be utilized. Based on this observation, we conclude that in such regions, the spectrum allocation design introduced in this chapter cannot be applied; hence, ML might need to be explored.

2.5.2 Performance of Multi-band-based Spectrum Allocation with ASB

In this section, we present numerical results to illustrate the performance of the proposed multi-band-based spectrum allocation with ASB, while considering the multi-band-based spectrum allocation with ESB as the benchmark [32]. The numerical results are obtained by considering a rectangular indoor environment of size 20 m $\times$ 20 m, where an AP at the center of the indoor environment serves 14 users. We consider that the 50 GHz spectrum that exists at the THz band between 0.670 and 0.720 THz is used to serve the users. We clarify that the considered 50 GHz spectrum exists within a PACSR. As in Section 2.5.1, we use the $k(f)$ values that are calculated using the ITU model for the ambient temperature, atmospheric pressure, and atmospheric water vapor density of 15° C, 101.30 kPa, and 7.5 g/m^3, respectively. The values of the rest of the parameters used for numerical results are summarized in Table 2.4, unless specified otherwise.

The problem $\mathbf{P^o_{1F}}$ is implemented in AMPL, which is popular for modeling optimization problems [117,119]. As for the approximation of $k(f)$ values in (2.12), the model parameters are $\sigma_1 = -52.951$, $\sigma_2 = 0.6964 \times 10^{-10}$, and $\sigma_3 = 0.0410$, as given in Table 2.2. As reflected in Table 2.2, these model parameters correspond to the average and maximum approximation errors of 0.24 % and 0.47 %, respectively. We also note that for the substitution introduced in (2.19), we consider $\xi_s = 5 \times 10^9$, $\omega_s = 5 \times 10^{10}$, and $\varsigma_s = 10^{-3}$, $\forall\, s \in \mathcal{S}$. We clarify that using $\widehat{d}_{\max} = 10\sqrt{2}$, $f_{\text{ref}} = 0.72 \times 10^9$, and $\widehat{k}(f_{\text{ref}}) = 0.1018$, we first obtain $\overline{\omega}$ as $\overline{\omega} = 1.0953{\times}10^{-10}$. Considering this, we then set ω_s to be $\omega_s = 0.5{\times}10^9$ such that the constraint (2.20) is satisfied. Thereafter, although it is possible to select any real values for ξ_s and ς_s, we set ξ_s and ς_s to be $5{\times}10^9$ and 10^{-3}, respectively, to ensure the domain of z_s defined by (2.23e) is within the numerical operating range of AMPL.

Table 2.4: Values of parameters used for numerical results in Section 2.5.2.

Parameter	**Symbol**	**Value**
Heights of the AP and users	h_{A}, h_{U}	3.0 m, 1.3 m
Antenna gains	G_{A}, B_{U}	35 dBi, 20 dBi
Noise power density	N_0	-174 dBm/Hz
Power budget at the AP	p_{tot}	-7.5 dBm
Upper bound on power per sub-band	$p_{\max}$	$\frac{4}{3}\frac{p_{\mathrm{tot}}}{n_{\mathrm{I}}}$
Upper bound on sub-band bandwidth	$b_{\max}$	4.5 GHz
Guard band bandwidth	B_{g}	0.5 GHz

Fig. 2.3 plots the aggregated multiuser data rate, $r_{\mathrm{AG}} = \sum_{s\in\mathcal{S}} r_s$, versus the power budget for the spectrum allocation schemes with ASB and ESB. Moreover, the data rate gain of adopting ASB relative to adopting ESB, Δr_{AG}, defined as

$$\Delta r_{\mathrm{AG}} = \frac{r_{\mathrm{AG}}|_{\mathrm{ASB}} - r_{\mathrm{AG}}|_{\mathrm{ESB}}}{r_{\mathrm{AG}}|_{\mathrm{ESB}}} \times 100, \tag{2.24}$$

is also plotted, where $r_{\mathrm{AG}}|_{\mathrm{ASB}}$ and $r_{\mathrm{AG}}|_{\mathrm{ESB}}$ are the aggregated multiuser data rates for spectrum allocation schemes with ASB and ESB, respectively. We first observe in Fig. 2.3 that the proposed spectrum allocation scheme with ASB achieves a significantly higher r_{AG} compared to spectrum allocation with ESB for different power budget levels. This is expected since, while spectrum allocation with ESB achieves a certain r_{AG}, the capability of the proposed spectrum allocation scheme with ASB to vary the sub-band bandwidths helps to further improve r_{AG}. Second, we observe that r_{AG} for spectrum allocation scheme with ASB improves when the upper bound on sub-band bandwidth, $b_{\max}$, increases. This is expected since a larger $b_{\max}$ gives more room to exploit the ASB capability, which improves the r_{AG}. These observations jointly demonstrate the significance of spectrum allocation with ASB, thereby validating the benefits of the proposed spectrum allocation strategy. We also observe that as expected, r_{AG} improves for spectrum allocation schemes with ASB and ESB when the power budget increases. Interestingly, in the higher power budget regime, the data rate gain of adopting ASB relative to adopting ESB, Δr_{AG}, is higher.

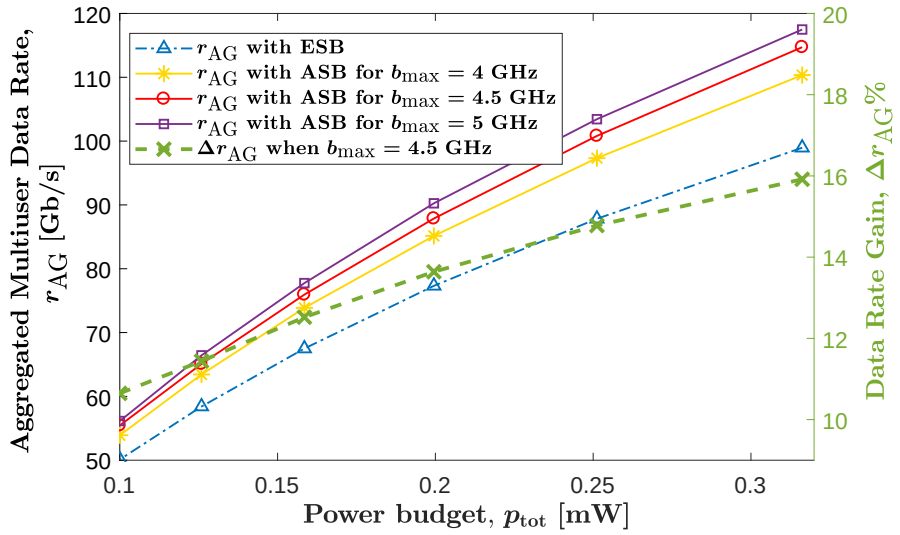

Figure 2.3: Aggregated multiuser data rate and the data rate gain versus the power budget at the AP.

We next investigate the impact of molecular absorption loss on the proposed spectrum allocation scheme with ASB. To this end, we consider several 50 GHz spectra within the first TW above 1 THz, and plot the r_{AG} for the spectrum allocation schemes with ASB and ESB within these spectra versus the end-frequency of these spectra, f_{ref}, in Fig. 2.4(a) when $p_{tot} = 5$ dBm. Also, the average of $k(f)$ values within the spectra, $E[k(f)]$, and the maximum difference between $k(f)$ values within the spectra are plotted in Fig. 2.4(b). We first observe in Fig. 2.4(a) that r_{AG} for the spectrum allocation schemes with ASB and ESB decreases when f_{ref} increases. This is due to the increase in $E[k_{abs}]$ when f_{ref} increases, as shown in Fig. 2.4(b), which in turn increases the molecular absorption loss in the sub-bands and reduces r_{AG}. We next observe in Fig. 2.4(a) that the data rate gain of adopting ASB relative to adopting ESB, Δr_{AG}, increases when f_{ref} increases. This is due to the fact that, as f_{ref} increases, the maximum difference between $k(f)$ values within the spectra increases as shown in Fig. 2.4(b). As a result, the variation in molecular absorption loss among the sub-bands would be very high when ESB is adopted, which in turn leads to more room to improve r_{AG} by adopting ASB. This observation indicates that it is more beneficial to adopt ASB when the variation in molecular absorption loss within the to-be-allocated spectrum is high.

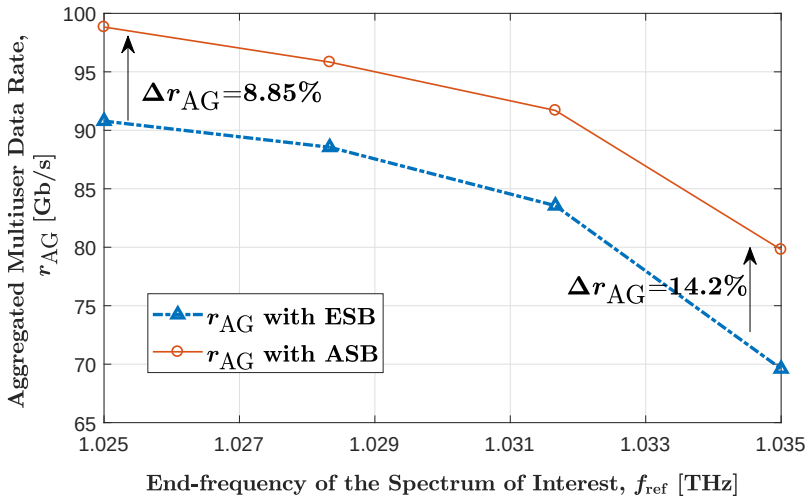

(a) Aggregated multiuser data rate versus the end-frequency of the to-be-allocated spectrum.

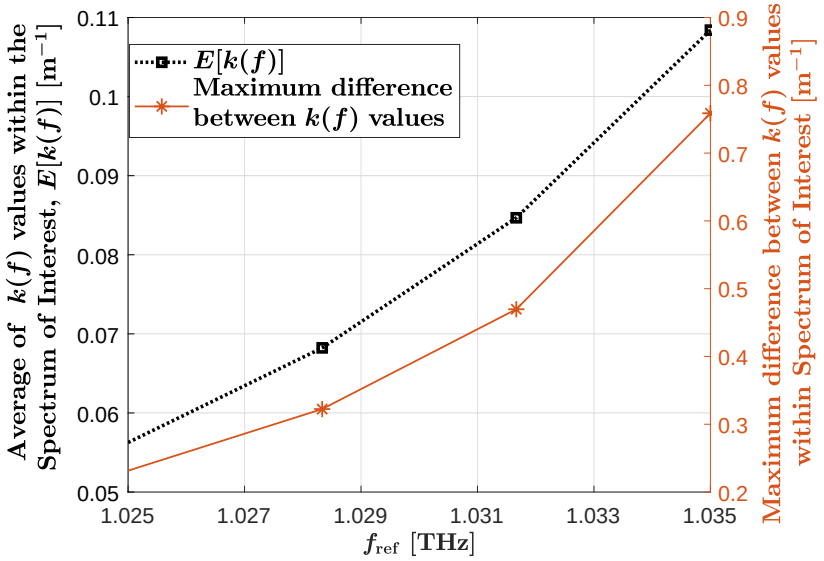

(b) The average and the maximum difference between $k(f)$ values within the spectra versus the end-frequency of the to-be-allocated spectrum.

Figure 2.4: Illustration of the impact of molecular absorption loss on the proposed spectrum allocation scheme.

2.6 Summary

In this chapter, we, for the first time, investigated the impacts of ASB in multi-band-based spectrum allocation at the THz band. To this end, we formulated an optimization problem, with the main focus on spectrum allocation, to determine the optimal sub-band bandwidth and transmit power. We then proposed approximations and transformations to solve the formulated problem. Aided by numerical results, we showed that by enabling ASB during spectrum allocation, a significantly higher rate can be achieved as compared to adopting ESB. We also showed that it is more beneficial to adopt ASB when the variation in molecular absorption loss within the to-be-allocated spectrum is high.

We clarify that implementation of the multi-band-based spectrum allocation scheme with ASB proposed in this chapter may need advancements beyond the current THz hardware capabilities. For example, very precise digital signal processing (DSP) filters, which are substantially expensive at THz frequencies, are necessary at THz transceivers, and THzCom users need to be equipped with tunable front-ends for adjusting their operating frequency and bandwidth. Despite so, we believe that the desire to realize the theoretically established benefits will inspire THz hardware researchers to expand the capability of current THz devices such that multi-band-based spectrum allocation schemes with ASB can be implemented using future THz devices.

We also clarify that the solution approach proposed in this chapter for the spectrum allocation problem with ASB is only applicable when (i) the to-be-allocated spectrum exists entirely in either a PACSR or an NACSR of the THz band and (ii) the variation of molecular absorption loss within the to-be-allocated spectrum is smooth such that it can be modeled as an exponential function of frequency with minimal approximation errors. Nevertheless, to harness the potential of the huge available bandwidths of TWs, it is necessary to develop a solution to the spectrum allocation problem with ASB when (i) the to-be-allocated spectrum spans multiple TWs and (ii) the molecular absorption coefficient varies in a highly non-linear manner. These considerations will be addressed in subsequent technical chapters.

Chapter 3

Spectrum Allocation Among Multiple Transmission Windows for THzCom Systems

3.1 Introduction

In this technical chapter, we explore the design of a novel spectrum allocation strategy for multiuser terahertz (THz) band communication (THzCom) systems when the to-be-allocated spectrum is composed of multiple transmission windows (TWs). This strategy explores the benefits of (i) sub-band assignment, (ii) avoiding using some spectra that exist at the edges of TWs where molecular absorption loss is very high, and (iii) allowing users to occupy sub-bands with unequal bandwidths, i.e., adaptive sub-band bandwidth (ASB). We clarify that the design in Chapter 2 is only applicable when the to-be-allocated spectrum exists entirely within a specific region of a TW. When the to-be-allocated spectrum spans multiple TWs, new challenges arise. On one hand, the number of sub-bands that exist within each TW, the set of users that are served by each TW, and the sub-band assignment policy need to be optimally decided. On the other hand, since molecular absorption loss is very high at the edges of TWs, it may be beneficial if some spectra at the edges of TWs are not used during spectrum allocation. These challenges have not been touched in Chapter 2, but need to be carefully addressed to exploit the

potential of the huge available bandwidth that spans multiple TWs at the THz band, which motivates this chapter.

We focus on a scenario where a single access point (AP) supports the downlink transmission of multiple users which demands high data rates. In this chapter, we consider the to-be-allocated spectrum spans across multiple TWs. For this system, we formulate an optimization problem, with the main emphasis on spectrum allocation. We aim to maximize the data rate of the multiuser THzCom system under given constraints on sub-band bandwidth, power, and rate. The problem consists of sub-band assignment, sub-band bandwidth allocation, determination of the unused spectra at the edges of TW, and power control. To solve the problem, we first propose modifications to the formulated problem and arrive at a mixed-integer non-linear problem. We then propose several transformations, including the binary variable to real variable transformation, and arrive at an approximate convex problem. Subsequently, we develop an iterative algorithm based on the successive convex approximation (SCA) technique to solve the approximate convex problem.

Aided by numerical results, we first show that the sub-band assignment design proposed in this chapter needs to be considered when the to-be-allocated spectrum is composed of multiple TWs, since the state-of-the-art distance-aware multi-carrier (DAMC)-based sub-band assignment is only readily applicable within a TW. We also show that when the to-be-allocated spectrum is composed of multiple TWs, enabling ASB achieves a significantly higher data rate as compared to adopting equal sub-band bandwidth (ESB). Moreover, we show that an additional gain can be obtained by optimally determining the unused spectra at the edges of TWs, as compared to avoiding using pre-defined spectra that exist at the edges of TWs. Finally, we show that the feasibility region of the resource allocation problem can be improved by adopting ASB and optimally determining the unused spectra at the edges of TWs.

The rest of the chapter is organized as follows. Section 3.2 introduces the system model. Section 3.3 presents the resource allocation problem associated with the design of the novel spectrum allocation strategy. Section 3.4 presents the solution approach adopted to solve the formulated resource allocation problem. Section 3.5 presents the numerical results and Section 3.6 summarises the chapter.

3.2 System Model

In this section, we introduce the system model considered in this chapter. Similar to that in Chapter 2, we consider a three-dimensional (3D) indoor THzCom system, as shown in Fig. 2.1, where a single AP, which is located at the center of the ceiling of the indoor environment, supports the downlink transmission of n_{I} users which demand high data rates. We consider that the users are stationary and distributed uniformly on the floor in this environment. We also assume that users in the system are equipped with tunable front-ends such that they can dynamically adjust their operating frequency and bandwidth to match those of their assigned sub-bands. We denote $\mathcal{I} = \{1, 2, \cdots, s, \cdots, n_{\mathrm{I}}\}$ as the set of users and further denote l_i and $d_i = \sqrt{(h_{\mathrm{A}} - h_{\mathrm{U}})^2 + l_i^2}$ as the horizontal and 3D distances of the link between the AP and the ith user, respectively, where h_{A} and h_{U} are the heights of the AP and users. Finally, we note that similar to that in Chapter 2, the impacts of blockages are ignored in this chapter.

3.2.1 THz Spectrum

In this chapter, we focus on the scenario where the to-be-allocated spectrum is composed of multiple TWs, as shown in Fig. 3.1. Similar to that in Chapter 2, positive absorption coefficient slope regions (PACSRs) and negative absorption coefficient slope regions (NACSRs) are defined as the spectrum regions within TWs with increasing and decreasing molecular absorption coefficients, respectively. Considering this, we find that the to-be-allocated spectrum is made of multiple PACSRs and NACSRs, as shown in Fig. 3.1. We denote $\mathcal{R}_{\mathrm{P}} = \{\mathrm{sr}_1^{\mathrm{p}}, \mathrm{sr}_2^{\mathrm{p}}, \cdots\}$ and $\mathcal{R}_{\mathrm{N}} = \{\mathrm{sr}_1^{\mathrm{n}}, \mathrm{sr}_2^{\mathrm{n}}, \cdots\}$ as the sets of the PACSRs and the NACSRs in the to-be-allocated spectrum, respectively. We further denote $\mathcal{R} = \{\tau, \tau \in \mathcal{R}_{\mathrm{P}} \cup \mathcal{R}_{\mathrm{N}}\}$ as the set of all regions in the to-be-allocated spectrum.

We focus on multi-band-based spectrum allocation. Thus, each region within the to-be-allocated spectrum is divided into sub-bands that are separated by guard bands. An illustration of the arrangement of sub-bands within a PACSR and an NACSR is depicted in Fig. 3.2. We denote $\mathcal{S}^{\tau} = \{1, 2, \cdots, s, \cdots, n_{\mathrm{S}}^{\tau}\}$ as the set of the sub-bands that exist in the region τ, where n_{S}^{τ} is the total number of sub-

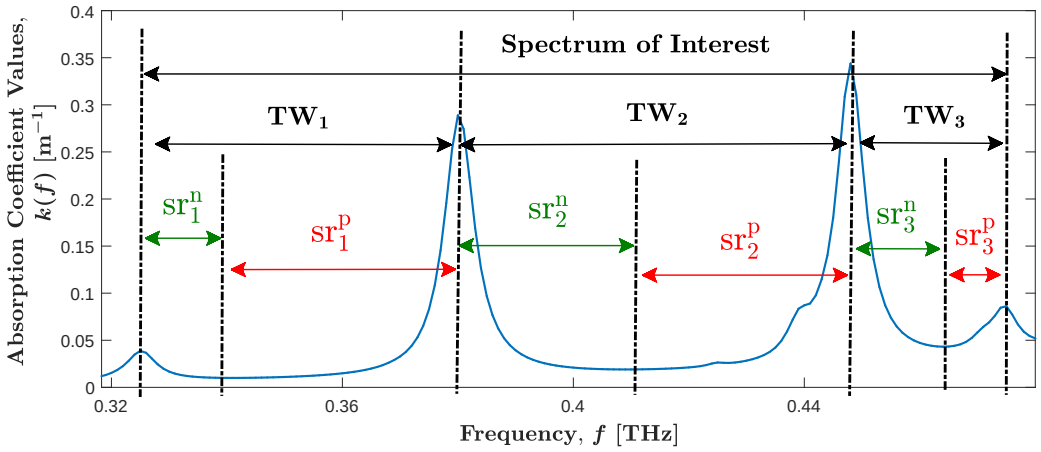

Figure 3.1: Illustration of TWs, PACSRs, and NACSRs that exist between 0.32 THz and 0.48 THz, with $\{\mathrm{TW}_1, \mathrm{TW}_2, \mathrm{TW}_3\}$, $\{\mathrm{sr}_1^{\mathrm{p}}, \mathrm{sr}_2^{\mathrm{p}}, \mathrm{sr}_3^{\mathrm{p}}\}$, and $\{\mathrm{sr}_1^{\mathrm{n}}, \mathrm{sr}_2^{\mathrm{n}}, \mathrm{sr}_3^{\mathrm{n}}\}$ denoting the TWs, PACSRs, and NACSRs, respectively.

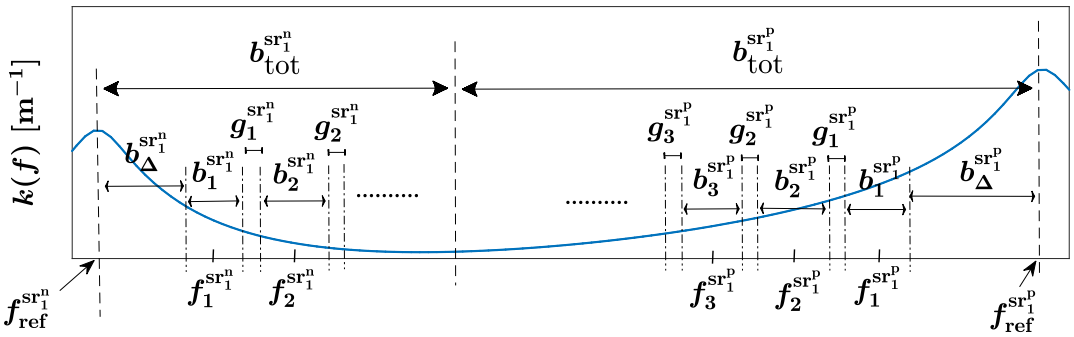

Figure 3.2: Illustration of sub-band arrangement within a PACSR and an NACSR.

bands in the region τ. We further denote b_s^τ and f_s^τ as the bandwidth and the center frequency of the sth sub-band that exists in the region τ, respectively. For notational convenience, we consider that sub-bands are labeled such that $f_1^\tau > f_2^\tau > \cdots > f_s^\tau > \cdots$ when $\tau \in \mathcal{R}_{\mathrm{P}}$ and $f_1^\tau < f_2^\tau < \cdots < f_s^\tau < \cdots$ when $\tau \in \mathcal{R}_{\mathrm{N}}$. Thus, f_s^τ can be expressed as

$$\begin{aligned} f_s^\tau &= f_{\mathrm{ref}}^\tau - \eta_\tau \left(b_\Delta^\tau + \sum_{\kappa=1}^{s} b_\kappa^\tau + \sum_{\kappa=1}^{s} g_\kappa^\tau - g_s^\tau - 0.5 b_s^\tau \right) \\ &= f_{\mathrm{ref}}^\tau - \eta_\tau \left(b_\Delta^\tau + \sum_{\kappa \in \mathcal{S}} \left(a_{1,s,\kappa} b_\kappa^\tau + a_{2,s,\kappa} g_\kappa^\tau \right) \right), \end{aligned} \tag{3.1}$$

where $s \in \mathcal{S}^\tau, \tau \in \mathcal{R}$, f^τ_{ref} is the end-frequency of the region τ when $\tau \in \mathcal{R}_{\text{P}}$ and the start-frequency of the region τ when $\tau \in \mathcal{R}_{\text{N}}$, as shown in Fig. 3.2. In addition, $\eta_\tau = 1$ when $\tau \in \mathcal{R}_{\text{P}}, \eta_\tau = -1$ when $\tau \in \mathcal{R}_{\text{N}}$, b^τ_Δ is the bandwidth of the unused spectrum that exists in the region τ, and g^τ_s is the bandwidth of the guard band that exists between the sth and the $(s-1)$th the sub-band in the region τ. Moreover, $a_{1,s,\kappa} = 1$, if $\kappa < s$, $a_{1,s,\kappa} = 0.5$, if $\kappa = s$, $a_{1,s,\kappa} = 0$, otherwise $\forall s, \kappa \in \mathbb{Z}^+$ and $a_{2,s,\kappa} = 1,$, if $\kappa < s$, $a_{2,s,\kappa} = 0$, otherwise $\forall s, \kappa \in \mathbb{Z}^+$. Since ASB is considered, we have

$$0 \leqslant b^\tau_s \leqslant b_{\max}, \qquad \forall s \in \mathcal{S}^\tau, \tau \in \mathcal{R}, \tag{3.2}$$

where $b_{\max}$ denotes the upper bound on the sub-band bandwidth. In this chapter, we optimally determine the value of b^τ_s by solving the optimization problem that will be formulated in the subsequent section. Also, we consider that the guard band bandwidth is fixed and is equal to B_{g}, i.e., $g^\tau_s = B_{\text{g}}$, $\forall s \in \mathcal{S}^\tau, \tau \in \mathcal{R}$.

Remark 3.1 *As shown in Figs. 3.1 and 3.2, the values of the molecular absorption coefficient are very high at the edges of TWs. Due to this, it may be beneficial if some spectra that exist at the edges of TWs are not utilized during spectrum allocation. To optimally determine the unused spectra at the edges of TW, we introduce a design variable b^τ_Δ in our spectrum allocation strategy, where b^τ_Δ denotes the unused spectra at the edge of each region where the molecular absorption coefficient is very high. It is reflected in* (3.1) *and depicted in Fig. 3.2.*

With all the aforementioned considerations, we express the total bandwidth available within the region τ as

$$b^\tau_{\text{tot}} = b^\tau_\Delta + \sum_{s \in \mathcal{S}^\tau} b^\tau_s + \sum_{s \in \mathcal{S}^\tau} g^\tau_s, \qquad \forall \tau \in \mathcal{R}. \tag{3.3}$$

Similar to that in [32, 46, 50] and Chapter 2, we assume that the users in the system are served by separate sub-bands. The justification behind this consideration is given in Section 2.2.3. Under this assumption, we set the total number of sub-bands in the to-be-allocated spectrum to be equal to the number of users in

the system, i.e.,

$$\sum_{\tau \in \mathcal{R}} n_{\mathrm{S}}^{\tau} = n_{\mathrm{I}}. \tag{3.4}$$

We note that although the total number of sub-bands in the to-be-allocated spectrum, i.e., $\sum_{\tau \in \mathcal{R}} n_{\mathrm{S}}^{\tau}$, is defined by (3.4), the number of sub-bands that exist within each region, i.e., $n_{\mathrm{S}}^{\tau},\ \forall \tau \in \mathcal{R}$, is unknown. Thus, n_{S}^{τ} should be carefully decided such that the spectra available within the regions are utilized optimally, while ensuring that the constraint (3.4) is satisfied.

Let us denote $x_{i,s}^{\tau}$ as the sub-band assignment indicator variable such that

$$x_{i,s}^{\tau} = \begin{cases} 1, & \text{if the } s\text{th sub-band in the region } \tau \text{ is assigned to the } i\text{th user,} \\ 0, & \text{otherwise,} \end{cases} \tag{3.5}$$

where $\forall i \in \mathcal{I}, s \in \mathcal{S}^{\tau}, \tau \in \mathcal{R}$. Under the assumption that the users in the system are served by separate sub-bands, we have

$$\sum_{\tau \in \mathcal{R}} \sum_{s \in \mathcal{S}^{\tau}} x_{i,s}^{\tau} = 1, \qquad \forall i \in \mathcal{I}, \tag{3.6a}$$

$$\sum_{i \in \mathcal{I}} x_{i,s}^{\tau} = 1, \qquad \forall s \in \mathcal{S}^{\tau}, \tau \in \mathcal{R}, \tag{3.6b}$$

where (3.6a) ensures that each user in the system is assigned one sub-band and (3.6b) ensures that each sub-band in the to-be-allocated spectrum is assigned to one user.

3.2.2 Achievable Data Rate

Considering the spreading loss and the frequency-selective molecular absorption loss at the THz band, the data rate achieved by the ith user in the sth sub-band

in region τ is obtained as [32]

$$r_{i,s}^{\tau} = \int_{f_s^{\tau}-\frac{1}{2}b_s^{\tau}}^{f_s^{\tau}+\frac{1}{2}b_s^{\tau}} C(f)\ \mathrm{d}f = \int_{f_s^{\tau}-\frac{1}{2}b_s^{\tau}}^{f_s^{\tau}+\frac{1}{2}b_s^{\tau}} \log_2\left(1+\frac{p_i \varrho e^{-k(f)d_i}}{(fd_i)^2 b_s^{\tau}}\right)\mathrm{d}f, \tag{3.7}$$

where $i \in \mathcal{I}, s \in \mathcal{S}^{\tau}, \tau \in \mathcal{R}$, $C(f)$ is the capacity when the frequency is f, p_i is the transmit power allocated to the ith user, f is the frequency, $k(f)$ is the molecular absorption coefficient at f, $\varrho = \frac{G_{\mathrm{A}}G_{\mathrm{U}}}{N_0}\left(\frac{c}{4\pi}\right)^2$, G_{A} and G_{U} are the antenna gains at the AP and users, respectively, c is the speed of light, and N_0 is the noise power density. It is noted that similar to that in Chapter 2, in this chapter, we (i) ignore the impact of non-line-of-sight (nLoS) rays and focus only on the line-of-sight (LoS) rays of THz signals [62,69,72,73,75,86–88], (ii) omit the impact of fading in the THz channel [62, 69, 72–75, 86–88, 113], and (iii) consider inter-band interference (Inter-BI) and intra-band interference (Intra-BI) free transmission [32,46,50,50,114]. The justifications behind these considerations are given in Section 2.2.4. Finally, the achievable data rate of the ith user is obtained as

$$r_i = \sum_{\tau\in\mathcal{R}}\sum_{s\in\mathcal{S}^{\tau}} x_{i,s}^{\tau} r_{i,s}^{\tau}, \qquad \forall i \in \mathcal{I}. \tag{3.8}$$

3.3 Optimal Resource Allocation

In this section, we present the resource allocation problem associated with multi-band-based spectrum allocation schemes when the to-be-allocated spectrum is composed of multiple TWs. We aim to maximize the sum data rate among all users under given constraints on sub-band bandwidth, power, and rate. Mathematically, this problem is formulated as

$$\mathbf{P_2^o}: \quad \underset{\substack{x_{i,s}^{\tau}, p_i, b_s^{\tau},\\ b_{\Delta}^{\tau}, \forall i,s,r}}{\text{maximize}} \quad \sum_{i\in\mathcal{I}} r_i \tag{3.9a}$$

$$\text{subject to} \quad \sum_{i\in\mathcal{I}} p_i \leqslant p_{\mathrm{tot}}, \tag{3.9b}$$

$$0 \leqslant p_i \leqslant p_{\max}, \quad \forall i \in \mathcal{I}, \tag{3.9c}$$

$$b_{\Delta}^{\tau} + \sum_{s \in \mathcal{S}^{\tau}} b_{s}^{\tau} + \sum_{s \in \mathcal{S}^{\tau}} g_{s}^{\tau} = b_{\text{tot}}^{\tau}, \quad \forall \tau \in \mathcal{R}, \tag{3.9d}$$

$$0 \leqslant b_{s}^{\tau} \leqslant b_{\max}, \quad \forall s \in \mathcal{S}^{\tau}, \tau \in \mathcal{R}, \tag{3.9e}$$

$$0 \leqslant b_{\Delta}^{\tau} \leqslant b_{\text{tot}}^{\tau}, \quad \forall \tau \in \mathcal{R}, \tag{3.9f}$$

$$r_{i} \geqslant r_{\text{thr}}, \quad \forall i \in \mathcal{I}, \tag{3.9g}$$

$$\sum_{\tau \in \mathcal{R}} n_{\text{S}}^{\tau} = n_{\text{I}}, \tag{3.9h}$$

$$\sum_{\tau \in \mathcal{R}} \sum_{s \in \mathcal{S}^{\tau}} x_{i,s}^{\tau} = 1, \quad \forall i \in \mathcal{I}, \tag{3.9i}$$

$$\sum_{i \in \mathcal{I}} x_{i,s}^{\tau} = 1, \quad \forall s \in \mathcal{S}^{\tau}, \tau \in \mathcal{R}, \tag{3.9j}$$

$$x_{i,s}^{\tau} \in \{0, 1\}, \quad \forall i \in \mathcal{I}, s \in \mathcal{S}^{\tau}, \tau \in \mathcal{R}. \tag{3.9k}$$

The problem consists of sub-band assignment, sub-band bandwidth allocation, determination of the unused spectra at the edges of TWs, and power control. The constraint (3.9b) reflects the power budget at the AP and (3.9c) ensures that the power allocated to each user is upper bounded by $p_{\max}$. Moreover, (3.9f) ensures that the unused spectra at the edges of TWs are upper bounded by b_{tot}^{τ} and (3.9g) ensures that the data rate achieved by each user is greater than the threshold r_{thr}. Furthermore, the justifications of (3.9d), (3.9e), (3.9h), (3.9i), (3.9j), and (3.9k) are given by (3.3) and (3.2), (3.4), (3.6a), (3.6b), and (3.5), respectively.

The novelty of the considered resource allocation problem, $\mathbf{P_2^o}$, is three-fold. First, we propose spectrum allocation with ASB for the scenario when the to-be-allocated spectrum is composed of multiple TWs. To the best of our knowledge, recent studies in THz band spectrum allocation for the scenario when the to-be-allocated spectrum is composed of multiple TWs have only considered ESB [32, 46, 50–54]. Second, we consider sub-band assignment in multiuser THzCom systems when the to-be-allocated spectrum is composed of multiple TWs, while the previous relevant studies in THz band spectrum allocation have only considered DAMC-based sub-band assignment, which is only readily applicable when the to-be-allocated spectrum is within a TWs. Third, we optimally determine the spectra at the edges of TWs that need to be avoided during spectrum allocation. To the best of our knowledge, previous relevant studies in THz band spectrum allocation

have only considered the unused spectra at the edges of TWs to be either zeros or chosen to be fixed and arbitrarily [40, 68]. In Section 3.5, we show the significance of these considerations using numerical results.

3.4 Solution Approach

We now present the solution to the optimization problem $\mathbf{P_2^o}$. We note that it is extremely difficult to use traditional optimization theory techniques to solve $\mathbf{P_2^o}$ in its current form. This is because of four challenges. We categorize the four challenges as **Challenges A, B, C,** and **D** as follows:

> **Challenge A:** Although the total number of sub-bands in the to-be-allocated spectrum, i.e., $\sum_{\tau \in \mathcal{R}} n_{\mathrm{S}}^{\tau}$, is defined by (3.9h), the number of sub-bands that exist within each region, i.e., $n_{\mathrm{S}}^{\tau},\ \forall \tau \in \mathcal{R}$, is unknown. This leads to the fact that (i) the number of design variables $x_{i,s}^{\tau}$ is unknown and (ii) the number of design variables b_s^{τ} corresponding to each region is unknown.
>
> **Challenge B:** It is difficult to obtain the data rate, $r_{i,s}^{\tau}$, as a tractable expression of the design variable $b_{\nu}^{\tau},\ \forall\ i \in \mathcal{I},\ s, \nu \in \mathcal{S},\ \tau \in \mathcal{R}$. On one hand, obtaining $r_{i,s}^{\tau}$ as per (3.7) involves an integral and the limits of the integral depend on $b_{\nu}^{\tau},\ \forall\ s, \nu \in \mathcal{S},\ \tau \in \mathcal{R}$. On the other hand, the values of $k(f)$ for all frequencies within the to-be-allocated spectrum are required to obtain $r_s^{\tau},\ \forall s \in \mathcal{S},\ \tau \in \mathcal{R}$.
>
> **Challenge C:** The $r_{i,s}^{\tau}$ is non-concave with respect to (w.r.t.) the design variables b_{ν}^{τ}, b_{Δ}^{τ},$g_{\nu}^{\tau},\ \forall\ i \in \mathcal{I}, s, \nu \in \mathcal{S}^{\tau}, \tau \in \mathcal{R}$.
>
> **Challenge D:** In $\mathbf{P_2^o}$, the design variable $x_{i,s}^{\tau}$ is binary. Thus, $\mathbf{P_2^o}$ is a mixed-integer non-linear problem, which is non-convex [55].

We note that **Challenges A** and **B** demand appropriate modifications to the problem $\mathbf{P_2^o}$. Furthermore, **Challenges C** and **D** demand appropriate transformations to the modified problem to arrive at a standard convex optimization problem. In the subsequent subsections, we discuss the modifications and the transformations introduced to the problem $\mathbf{P_2^o}$.

3.4.1 Problem Reformulation

We first handle **Challenge A**, i.e., the intractability caused in $\mathbf{P_2^o}$ due to the number of sub-bands that exist within each region being unknown. To this end, we first consider that there exist n_{I} sub-bands within each region, i.e., $n_{\mathrm{S}}^{\tau} = n_{\mathrm{I}}$, $\forall\, \tau \in \mathcal{R}$. This implies that there would be $n_{\mathrm{R}} \times n_{\mathrm{I}}$ sub-bands in the entire to-be-allocated spectrum, where n_{R} is the total number of regions in the to-be-allocated spectrum. Out of these $n_{\mathrm{R}} \times n_{\mathrm{I}}$ sub-bands, we ensure that only some of the sub-bands are used by at most one user, while the remaining sub-bands are not assigned to any user. To reflect this modification, we replace (3.9h) and (3.9j) in $\mathbf{P_2^o}$ with

$$n_{\mathrm{S}}^{\tau} = n_{\mathrm{I}}, \qquad \forall \tau \in \mathcal{R}, \tag{3.10a}$$

$$\sum_{i \in \mathcal{I}} x_{i,s}^{\tau} \leqslant 1, \qquad \forall s \in \mathcal{S}^{\tau}, \tau \in \mathcal{R}. \tag{3.10b}$$

After this modification, although the intractability of $\mathbf{P_2^o}$ caused by the unknown number of design variables $x_{i,s}^{\tau}$ and b_s^{τ} can be solved, a new challenge arises due to the existence of guard bands in each region. Specifically, our spectrum allocation strategy considers that guard bands with a bandwidth of B_{g} exist between sub-bands. Thus, $(n_{\mathrm{I}} - 1)$ guard bands appear in each region as each region consists of n_{I} sub-bands after the modification. This would result in guard bands existing even between sub-bands that have zero bandwidth, which must be avoided. To overcome this challenge, we first consider that the bandwidths of guard bands, g_s^{τ}, are variables such that

$$0 \leqslant g_s^{\tau} \leqslant B_{\mathrm{g}}, \qquad \forall s \in \mathcal{S}, \tau \in \mathcal{R}. \tag{3.11}$$

Then, we ensure that there exists exactly one guard band with the bandwidth of B_{g} between sub-bands that have non-zero bandwidth, and the remaining guard bands have zero bandwidth. This is achieved by ensuring that the guard band between the sth and the $(s-1)$th sub-band in a given region has non-zero bandwidth only if the sth sub-band of this region has non-zero bandwidth. Mathematically, this is

expressed as

$$g_s^\tau = \begin{cases} B_{\mathrm{g}}, & b_s^\tau \neq 0, \\ 0, & \text{otherwise}, \end{cases} \qquad \forall s \in \mathcal{S}^\tau, \tau \in \mathcal{R}. \tag{3.12}$$

We then note that $b_s^\tau \neq 0$ when $\sum_{i \in \mathcal{I}} x_{i,s}^\tau = 1$. Considering this, (3.12) is equivalently expressed as

$$B_{\mathrm{g}} \sum_{i \in \mathcal{I}} x_{i,s}^\tau \leqslant g_s^\tau \leqslant B_{\mathrm{g}} \sum_{i \in \mathcal{I}} x_{i,s}^\tau, \qquad \forall s \in \mathcal{S}^\tau, \tau \in \mathcal{R}. \tag{3.13}$$

We next handle **Challenge B**, i.e., the intractability caused in $\mathbf{P_2^o}$ due to the difficulty in obtaining $r_{i,s}^\tau$ as a tractable expression of b_ν^τ, $i \in \mathcal{I}$, $s, \nu \in \mathcal{S}$, $\tau \in \mathcal{R}$. To this end, we utilize the two-step procedure similar to that adopted in Chapter 2. In the first step, through curve fitting, we model the values of $k(f)$ corresponding to the to-be-allocated spectrum using a piecewise exponential function of f with each region modeled by a separate exponential function piece. In particular, we approximate $k(f)$ in the region τ as

$$\widehat{k}^\tau(f) = e^{\sigma_1^\tau + \sigma_2^\tau f} + \sigma_3^\tau, \tag{3.14}$$

where $\min\{f_{\mathrm{ref}}^\tau, f_{\mathrm{ref}}^\tau - \eta_r b_{\mathrm{tot}}^\tau\} \leqslant f \leqslant \max\{f_{\mathrm{ref}}^\tau, f_{\mathrm{ref}}^\tau - \eta_r b_{\mathrm{tot}}^\tau\}$, $\tau \in \mathcal{R}$ and $\{\sigma_1^\tau, \sigma_2^\tau, \sigma_3^\tau\}$ are the model parameters obtained for the region τ. Thereafter, in the second step, we approximate the monotonically decreasing (or increasing) behavior of $C(f)$ in (3.7) within the PACSR (or the NACSR) using a piecewise linear function. This approximation allows to modify $r_{i,s}^\tau$ in (3.7) into a simplified expression, given by

$$r_{i,s}^\tau = b_s^\tau \log_2 \left(1 + \frac{p_i \varrho e^{-\left(e^{\sigma_1^\tau + \sigma_2^\tau f_s^\tau} + \sigma_3^\tau\right) d_i}}{(f_s^\tau d_i)^2 b_s^\tau} \right). \tag{3.15}$$

With these aforementioned modifications, we transform $\mathbf{P_2^o}$ into the following tractable optimization problem, given by

$$\widehat{\mathbf{P}}_{\mathbf{2}}^{\mathbf{o}}: \quad \underset{\substack{x_{i,s}^\tau, p_i, b_\Delta^\tau, \\ b_s^\tau, g_s^\tau, \forall i,s,r}}{\text{minimize}} \quad -\sum_{i \in \mathcal{I}} \sum_{\tau \in \mathcal{R}} \sum_{s \in \mathcal{S}^\tau} x_{i,s}^\tau r_{i,s}^\tau \tag{3.16}$$

$$\text{subject to} \quad (3.9b)-(3.9g),(3.9i),(3.9k),(3.10a),(3.10b),(3.13).$$

where $r_{i,s}^{\tau}$ is given by (3.15).

3.4.2 Convex Optimization-based Solution

We note that after addressing **Challenges A and B**, although $\widehat{\mathbf{P}}_{\mathbf{2}}^{\mathbf{o}}$ is tractable, it is non-convex in its current form. This is due to (i) **Challenge C**, i.e., the non-concavity of $r_{i,s}^{\tau}$ w.r.t. the design variables b_{ν}^{τ}, b_{Δ}^{τ},g_{ν}^{τ}, $\forall\, i \in \mathcal{I}, s, \nu \in \mathcal{S}^{\tau}, \tau \in \mathcal{R}$, and (ii) **Challenge D**, i.e., the design variable $x_{i,s}^{\tau}$ in $\widehat{\mathbf{P}}_{\mathbf{2}}^{\mathbf{o}}$ is binary. We handle these challenges as follows:

To handle **Challenge C**, we utilize the procedure similar to that adopted in Chapter 2. Specifically, we introduce the following substitutions for b_{s}^{τ}, b_{Δ}^{τ}, and g_{s}^{τ}, given by

$$b_{s}^{\tau} = \xi_{1,s}^{\tau} + \omega_{1,s}^{\tau}\log(\varsigma_{1,s}^{\tau} z_{1,s}^{\tau}), \quad \forall s \in \mathcal{S}^{\tau}, \tau \in \mathcal{R}, \tag{3.17a}$$

$$b_{\Delta}^{\tau} = \xi_{1,0}^{\tau} + \omega_{1,0}^{\tau}\log(\varsigma_{1,0}^{\tau} z_{1,0}^{\tau}), \quad \forall \tau \in \mathcal{R}, \tag{3.17b}$$

$$g_{s}^{\tau} = \xi_{2,s}^{\tau} + \omega_{2,s}^{\tau}\log(\varsigma_{2,s}^{\tau} z_{2,s}^{\tau}), \quad \forall s \in \mathcal{S}^{\tau}, \tau \in \mathcal{R}, \tag{3.17c}$$

where $\xi_{\phi,s}^{\tau}, \omega_{\phi,s}^{\tau}, \varsigma_{\phi,s}^{\tau}$ are real constants with $\phi \in \Phi = \{1,2\}$ and $z_{\phi,s}^{\tau}$, $\forall \phi \in \Phi,\ s \in \mathcal{S}_{\phi}^{\tau}, \tau \in \mathcal{R}$, are the new design variables that replace b_{s}^{τ}, b_{Δ}^{τ}, g_{s}^{τ} in the optimization problem, with $\mathcal{S}_{1}^{\tau} = \mathcal{S}^{\tau} \cup \{0\}$ and $\mathcal{S}_{2}^{\tau} = \mathcal{S}^{\tau}$. We note that following Lemma 2.1, $\omega_{\phi,s}^{\tau}$ in (3.17a)-(3.17c) are selected such that $1/\omega_{\phi,s}^{\tau} > \overline{\omega}^{\tau}$, $\forall\ s \in \mathcal{S}_{\phi}^{\tau}, \tau \in \mathcal{R}$, $\phi \in \Phi$, where

$$\overline{\omega}^{\tau} = |\sigma_{2}^{\tau}| \left(\widehat{d}_{\max} \widehat{k}^{\tau}(f_{\text{ref}}^{\tau}) e^{\widehat{d}_{\max}\sigma_{3}^{\tau}} - 1 \right), \tag{3.18}$$

with $\widehat{d}_{\max} > d_{\max}$, and $d_{\max}$ is the maximum of the link distances, i.e., $d_{\max} = \max_{i\in\mathcal{I}}\{d_i\}$ [116]. Considering these replacements, we transform $\widehat{\mathbf{P}}_{\mathbf{2}}^{\mathbf{o}}$ into the following equivalent problem, given by

$$\widetilde{\mathbf{P}}_{\mathbf{2}}^{\mathbf{o}}: \underset{\substack{x_{i,s}^{\tau}, p_i, z_{\phi,s}^{\tau}, \\ \forall i,s,r,\phi}}{\text{minimize}} \quad -\sum_{i\in\mathcal{I}}\sum_{\tau\in\mathcal{R}}\sum_{s\in\mathcal{S}^{\tau}} x_{i,s}^{\tau} r_{i,s}^{\tau} \tag{3.19a}$$

$$\text{subject to} \quad (3.9b),(3.9c),(3.9g),(3.9i),(3.9k),(3.10a),(3.10b),$$

$$\prod_{\phi\in\Phi}\prod_{s\in\mathcal{S}^\tau_\phi}(z^\tau_{\phi,s})^{\omega^\tau_{\phi,s}}-\prod_{\phi\in\Phi}\prod_{s\in\mathcal{S}^\tau_\phi}\frac{e^{b^\tau_{\text{tot}}-\sum_{\phi\in\Phi}\sum_{s\in\mathcal{S}^\tau}\xi^\tau_{\phi,s}}}{(\varsigma^\tau_{\phi,s})^{\omega^\tau_{\phi,s}}}\leqslant 0,\ \forall\tau\in\mathcal{R}, \tag{3.19b}$$

$$z^\tau_{\min,\phi,s}\leqslant z^\tau_{\phi,s}\leqslant z^\tau_{\max,\phi,s},\qquad \forall s\in\mathcal{S}^\tau.\tau\in\mathcal{R},\phi\in\Phi, \tag{3.19c}$$

In $\widetilde{\mathbf{P}}^{\mathbf{o}}_{\mathbf{2}}$,

$$z^\tau_{\min,1,s}=z^\tau_{\text{ref},1,s}e^{\frac{\delta_{\text{B}}}{\omega^\tau_{1,s}}}, \tag{3.20}$$

$$z^\tau_{\text{ref},\phi,s}=(\varsigma^\tau_{\phi,s})^{-1}e^{\frac{-\xi^\tau_{\phi,s}}{\omega^\tau_{\phi,s}}}, \tag{3.21}$$

$$z^\tau_{\max,1,s}=z^\tau_{\text{ref},1,s}e^{\frac{b_{\max}}{\omega^\tau_{1,s}}}, \tag{3.22}$$

$$z^\tau_{\min,2,s}=z^\tau_{\max,2,s}=z^\tau_{\text{ref},2,s}\big(1+\sum_{i\in\mathcal{I}}x^\tau_{i,s}\big(e^{\frac{B_{\text{g}}}{\omega^\tau_{2,s}}}-1\big)\big), \tag{3.23}$$

and δ_{B} is a very small positive number. We note that in $\widetilde{\mathbf{P}}^{\mathbf{o}}_{\mathbf{2}}$, (3.19b) and (3.19c) are obtained by substituting (3.17a)-(3.17c) into (3.9d)-(3.9f) and (3.13).

We next handle **Challenge D**, i.e., the non-convexity of $\widetilde{\mathbf{P}}^{\mathbf{o}}_{\mathbf{2}}$ caused by the binary constraint function (3.9k). To this end, we first relax the binary variables in $\widetilde{\mathbf{P}}^{\mathbf{o}}_{\mathbf{2}}$ into real variables [118–120]. Let us denote $\widetilde{x}^\tau_{i,s}$ as the real variables that would replace $x^\tau_{i,s}$ in the optimization problem. We then rewrite the binary constraint function (3.9k) equivalently as the combination of two constraints, given by

$$0\leqslant\widetilde{x}^\tau_{i,s}\leqslant 1,\qquad\qquad \forall i\in\mathcal{I},s\in\mathcal{S}^\tau,\tau\in\mathcal{R}, \tag{3.24a}$$

$$\sum_{i\in\mathcal{I}}\sum_{\tau\in\mathcal{R}}\sum_{s\in\mathcal{S}^\tau}\Big(\widetilde{x}^\tau_{i,s}\big(1-\widetilde{x}^\tau_{i,s}\big)\Big)\leqslant 0. \tag{3.24b}$$

We note that although $\widetilde{x}^\tau_{i,s}$ is relaxed to be real between zero and one in (3.24a), the constraint (3.24b) guarantees that $\widetilde{x}^\tau_{i,s}$ can only be zero or one, since $\widetilde{x}^\tau_{i,s}\big(1-\widetilde{x}^\tau_{i,s}\big)\geq 0,\forall i\in\mathcal{I},s\in\mathcal{S},\tau\in\mathcal{R}$. Thereafter, considering (3.24a) and (3.24b), we transform $\widehat{\mathbf{P}}^{\mathbf{o}}_{\mathbf{2}}$ into the following equivalent problem, given by

$$\widetilde{\mathbf{P}}^{\mathbf{o}}_{\mathbf{2}}:\underset{\substack{\widetilde{x}^\tau_{i,s},p_i,z^\tau_{\phi,s},\\ \forall i,s,r,\phi}}{\text{minimize}}\quad -\sum_{i\in\mathcal{I}}\sum_{\tau\in\mathcal{R}}\sum_{s\in\mathcal{S}^\tau}\widetilde{x}^\tau_{i,s}r^\tau_{i,s} \tag{3.25a}$$

$$\text{subject to} \quad (3.9b), (3.9c), \widetilde{(3.9g)}, (3.10a), \widetilde{(3.10b)}, (3.19b), \widetilde{(3.19c)}, (3.24a), (3.24b),$$

where $\widetilde{(3.9g)}$, $\widetilde{(3.10b)}$, and $\widetilde{(3.19c)}$ are the constraints obtained by replacing $x_{i,s}^{\tau}$ with $\widetilde{x}_{i,s}^{\tau}$ in (3.9g), (3.10b), and (3.19c), respectively.

After this transformation, we note that (3.24b) is non-convex w.r.t. $\widetilde{x}_{i,s}^{\tau}$. To handle this non-convexity, we consider the Taylor approximation of the function $\Xi(x) = x(1-x)$ [119]. We observe that the Taylor approximation of $\Xi(x)$ is convex and it provides an upper bound on $\Xi(x)$. Considering this, we obtain

$$F_{\mathrm{p}}^{(q)} = \sum_{i\in\mathcal{I}}\sum_{\tau\in\mathcal{R}}\sum_{s\in\mathcal{S}^{\tau}} \left(\widetilde{x}_{i,s}^{\tau}\big(1-2\widetilde{x}_{i,s}^{\tau(q)}\big) + \big(\widetilde{x}_{i,s}^{\tau(q)}\big)^2\right) \geqslant \sum_{i\in\mathcal{I}}\sum_{s\in\mathcal{S}}\sum_{\tau\in\mathcal{R}} \left(\widetilde{x}_{i,s}^{\tau}\big(1-\widetilde{x}_{i,s}^{\tau}\big)\right), \tag{3.26}$$

where $\widetilde{x}_{i,s}^{\tau(q)}$ is the qth approximation of $\widetilde{x}_{i,s}^{\tau}$. Finally, using (3.26), we relax the constraint (3.24b) and include it as a penalty function in the objective function [118, 120]. In doing so, we transform $\widetilde{\mathbf{P}}_{\mathbf{2}}^{\mathbf{o}}$ as

$$\begin{aligned}
\mathbf{P}_{\mathbf{2F}}^{\mathbf{o}}: \underset{\substack{\widetilde{x}_{i,s}^{\tau}, p_i, z_{\phi,s}^{\tau},\\ \forall i,s,r,\phi}}{\text{minimize}} \quad & \mathcal{E}_{2\mathrm{F}}^{(q)}\left(\widetilde{x}_{i,s}^{\tau}, p_i, z_{\phi,s}^{\tau}\right) && (3.27a)\\
\text{subject to} \quad & \sum_{i\in\mathcal{I}} p_i \leqslant p_{\mathrm{tot}}, && (3.27b)\\
& 0 \leqslant p_i \leqslant p_{\max}, \quad \forall i \in \mathcal{I}, && (3.27c)\\
& \sum_{\tau\in\mathcal{R}}\sum_{s\in\mathcal{S}^{\tau}} \widetilde{x}_{i,s}^{\tau(q)} r_{i,s}^{\tau} \geqslant r_{\mathrm{thr}}, \quad \forall i \in \mathcal{I}, && (3.27d)\\
& n_{\mathrm{S}}^{\tau} = n_{\mathrm{I}}, \qquad \forall \tau \in \mathcal{R}, && (3.27e)\\
& \sum_{i\in\mathcal{I}} \widetilde{x}_{i,s}^{\tau(q)} \leqslant 1, \qquad \forall s \in \mathcal{S}^{\tau}, \tau \in \mathcal{R}, && (3.27f)\\
& \prod_{\phi\in\Phi}\prod_{s\in\mathcal{S}_{\phi}^{\tau}} \left(z_{\phi,s}^{\tau}\right)^{\omega_{\phi,s}^{\tau}} - \prod_{\phi\in\Phi}\prod_{s\in\mathcal{S}_{\phi}^{\tau}} \frac{e^{b_{\mathrm{tot}}^{\tau} - \sum_{\phi\in\Phi}\sum_{s\in\mathcal{S}^{\tau}} \xi_{\phi,s}^{\tau}}}{\left(\varsigma_{\phi,s}^{\tau}\right)^{\omega_{\phi,s}^{\tau}}} \leqslant 0, \ \forall \tau \in \mathcal{R}, && (3.27g)\\
& z_{\min,\phi,s}^{\tau} \leqslant z_{\phi,s}^{\tau} \leqslant z_{\max,\phi,s}^{\tau}, \qquad \forall s \in \mathcal{S}^{\tau}, \tau \in \mathcal{R}, \phi \in \Phi, && (3.27h)\\
& \sum_{i\in\mathcal{I}}\sum_{\tau\in\mathcal{R}}\sum_{s\in\mathcal{S}^{\tau}} \left(\widetilde{x}_{i,s}^{\tau(q)}\big(1-\widetilde{x}_{i,s}^{\tau(q)}\big)\right) \leqslant 0. && (3.27i)
\end{aligned}$$

Algorithm 1 Iterative Approach for Solving the Problem $\mathbf{P^o_{2F}}$

1: **Initialization**: Set iteration count $q = 0$. Set initial point for $\widetilde{x}_{i,s}^{\tau(q)} = 0.5$, $\forall i \in \mathcal{I}, \tau \in \mathcal{R}, s \in \mathcal{S}^\tau$. Select a high penalty factor $\Lambda_{\mathrm{P}} = 200$ and a low tolerance value $\delta_{\mathrm{T}} = 10^{-6}$.
2: **While** $F_{\mathrm{p}}^{(q)} \geqslant \delta_{\mathrm{T}}$
3: Solve $\mathbf{P^o_{2F}}$ in (3.27) using the point $\widetilde{x}_{i,s}^{\tau(q)}$, and obtain $p_i^*, \widetilde{x}_{i,s}^{\tau*}, z_{\phi,s}^{\tau*}$ and $\mathcal{E}_{2\mathrm{F}}^{(q)}\left(\widetilde{x}_{i,s}^{\tau*}, p_i^*, z_{\phi,s}^{\tau*}\right)$.
4: Update $\widetilde{x}_{i,s}^{\tau(q+1)} = \widetilde{x}_{i,s}^{\tau*}$, $\forall i \in \mathcal{I}, \tau \in \mathcal{R}, s \in \mathcal{S}^\tau$.
5: Update point iteration count $q = q + 1$.
6: **End While**

In $\mathbf{P^o_{2F}}$, $\mathcal{E}_{2\mathrm{F}}^{(q)}\left(\widetilde{x}_{i,s}^{\tau}, p_i, z_{\phi,s}^{\tau}\right) = -\sum_{i\in\mathcal{I}}\sum_{\tau\in\mathcal{R}}\sum_{s\in\mathcal{S}^\tau}\widetilde{x}_{i,s}^{\tau} r_{i,s}^{\tau} + \Lambda_{\mathrm{P}} F_{\mathrm{p}}^{(q)}$ is the qth approximation of the objective function of $\mathbf{P^o_{2F}}$, and $\Lambda_{\mathrm{P}} \geqslant 0$ is the constant penalty factor. We note that $\mathbf{P^o_{2F}}$ is obtained as a standard convex optimization problem [55]. Thus, by using the SCA technique, we propose an iterative algorithm to solve $\mathbf{P^o_{2F}}$, which is summarized in Algorithm 1 [56, 117].

Convergence of Algorithm 1: We clarify that in Step 3 of Algorithm 1, $\mathcal{E}_{2\mathrm{F}}^{(q)}$ is optimized for the given $\widetilde{x}_{i,s}^{\tau(q)}$. This yields [121, 122]

$$\mathcal{E}_{2\mathrm{F}}^{(q+1)}\left(\widetilde{x}_{i,s}^{\tau(q+1)}, p_i^{(q+1)}, z_{\phi,s}^{\tau(q+1)}\right) \leqslant \mathcal{E}_{2\mathrm{F}}^{(q)}\left(\widetilde{x}_{i,s}^{\tau(q)}, p_i^{(q)}, z_{\phi,s}^{\tau(q)}\right), \qquad \forall q. \tag{3.28}$$

Thus, Algorithm 1 produces a monotone sequence of improved feasible solutions to the problem $\mathbf{P^o_{2F}}$, $\left\{\mathcal{E}_{2\mathrm{F}}^{(q)}\left(\widetilde{x}_{i,s}^{\tau(q)}, p_i^{(q)}, z_{\phi,s}^{\tau(q)}\right)\right\}$, once $\widetilde{x}_{i,s}^{\tau(q)}$ is initialized from a feasible point, e.g., $x_{i,s}^{\tau(q)} = 0.5$, $\forall i \in \mathcal{I}, \tau \in \mathcal{R}, s \in \mathcal{S}^\tau$. Moreover, $\left\{\mathcal{E}_{2\mathrm{F}}^{(q)}\left(\widetilde{x}_{i,s}^{\tau(q)}, p_i^{(q)}, z_{\phi,s}^{\tau(q)}\right)\right\}$ is bounded by constraints (3.27d) and (3.27h). Based on these, it can be concluded that the convergence of Algorithm 1 is guaranteed, i.e., $\left(\mathcal{E}_{2\mathrm{F}}^{(q+1)}\left(\widetilde{x}_{i,s}^{\tau(q+1)}, p_i^{(q+1)}, z_{\phi,s}^{\tau(q+1)}\right)\right.$ $\left.-\mathcal{E}_{2\mathrm{F}}^{(q)}\left(\widetilde{x}_{i,s}^{\tau(q)}, p_i^{(q)}, z_{\phi,s}^{\tau(q)}\right)\right) \longrightarrow 0$ as $\kappa \longrightarrow \infty$ [121, 122]. A detailed proof of convergence of a similar algorithm can be found in [121].

Complexity of Algorithm 1: By checking the operations of Algorithm 1, we find that the same steps are executed in each iteration; thus, we focus only on the complexity of one iteration. The dominating computational complexity of the algorithm arises from Step 3, where $\mathbf{P^o_{2F}}$ is solved to obtain $p_i^*, \widetilde{x}_{i,s}^{\tau*}, z_{\phi,s}^{\tau*}$ and $\mathcal{E}_{2\mathrm{F}}^{(q)}\left(\widetilde{x}_{i,s}^{\tau*}, p_i^*, z_{\phi,s}^{\tau*}\right)$. Thus, solving each iteration of Algorithm 1 requires a complexity

of $\mathcal{O}\Big(n_{\mathrm{D}}^3 n_{\mathrm{C}}\Big)$ [118], since there are $n_{\mathrm{D}} = \big(n_{\mathrm{I}}^2 n_{\mathrm{R}} + 2n_{\mathrm{I}} n_{\mathrm{R}} + n_{\mathrm{I}}\big)$ decision variables and $n_{\mathrm{C}} = \big(n_{\mathrm{I}}^2 n_{\mathrm{R}} + 3n_{\mathrm{I}} n_{\mathrm{R}} + 3n_{\mathrm{I}} + n_{\mathrm{R}} + 1\big)$ convex constraints in $\mathbf{P^o_{2F}}$.

Remark 3.2 *As can be observed, the computational complexity of Algorithm 1 may be very high, especially when the number of users and spectrum regions in the considered system are very high. We note that the high complexity in Algorithm 1 arises due to sub-band assignment. However, as will be shown using numerical results in the next section of this chapter, according to the optimal sub-band assignment configuration, the users with longer distances are assigned to center sub-bands where the absorption loss is low while the users with shorter distances are assigned to edge sub-bands where the absorption loss is high. This insight can be used to heuristically assign sub-bands to users during real-time implementation of the algorithm, thereby avoiding the high complexity that arises due to the consideration of sub-band assignment. This insight can only be obtained by developing Algorithm 1, thereby highlighting the significance of our proposed algorithm, although it is computationally very intensive.*

3.5 Numerical Results

In this section, we present numerical results to examine the performance of the proposed multi-band-based spectrum allocation scheme. Specifically, we consider an indoor environment of size 20 m × 20 m, where an AP at the center of the indoor environment serves 30 users. We also consider that the spectrum that exists between 0.325 THz and 0.448 THz is used to serve the users. We clarify that the considered spectrum spans across two TWs and each of the TW is composed of a PACSR and an NACSR. We denote the two TWs and the four regions by $\{\mathrm{TW}_2, \mathrm{TW}_3\}$ and $\{\mathrm{sr}_2^{\mathrm{p}}, \mathrm{sr}_2^{\mathrm{n}}, \mathrm{sr}_3^{\mathrm{p}}\, \mathrm{sr}_3^{\mathrm{n}}\}$, respectively, as depicted in Fig. 3.1. Unless otherwise stated, the values of the other parameters used for numerical results are as follows: $B_{\mathrm{g}} = 1$ GHz, $b_{\max} = 4.5$ GHz, $p_{\mathrm{tot}} = -12.5$ dBm, $p_{\max} = \frac{4p_{\mathrm{tot}}}{3n_{\mathrm{I}}}$, $r_{\mathrm{thr}} = 2$ Gbps, $h_{\mathrm{A}} = 3$ m, $h_{\mathrm{U}} = 1$ m, $G_{\mathrm{A}} = 35$ dBi, $G_{\mathrm{U}} = 20$ dBi, $N_0 = -174$ dBm/Hz, $\xi_{\phi,s}^{\tau} = 10^{9.7}$, $\omega_{\phi,s}^{\tau} = 10^{10.7}$, and $\varsigma_{\phi,s}^{\tau} = 10^{-3}$.

In Fig. 3.3, we plot the performance gain achieved by (i) considering ASB when the to-be-allocated spectrum is composed of multiple TWs, i.e., $0 \leqslant b_s^{\tau} \leqslant$

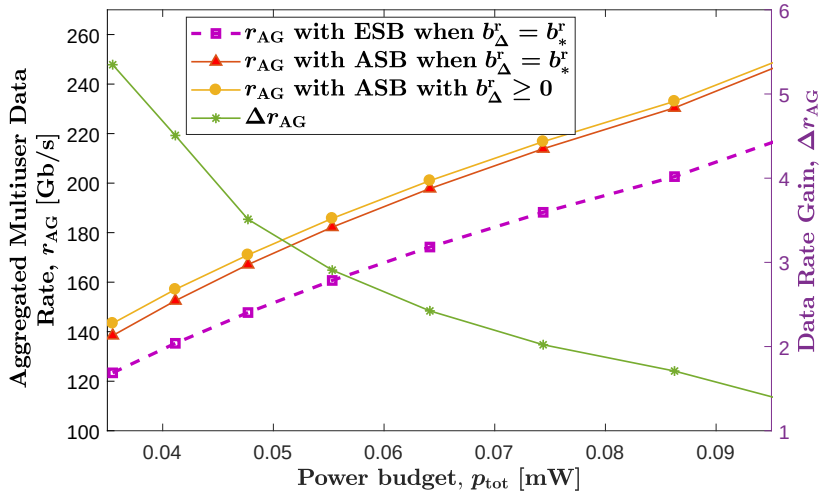

(a) Aggregated multiuser data rate versus the power budget.

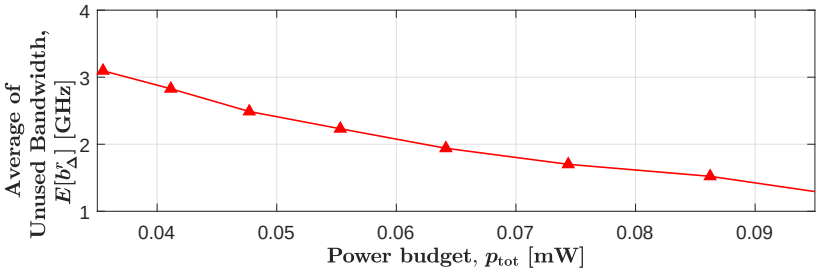

(b) The average of unused bandwidth versus the power budget.

Figure 3.3: Illustration of the performance achieved by the proposed spectrum allocation scheme.

$b_{\max}$, $\forall s \in \mathcal{S}^{\tau}, \tau \in \mathcal{R}$, and (ii) optimally determining the unused spectra that exist at the edge of TWs, i.e., $b^{\tau}_{\Delta} \geq 0$, $\forall \tau \in \mathcal{R}$. In Fig. 3.3(a), we first observe the aggregated multiuser data rate, $r_{\text{AG}} = \sum_{i \in \mathcal{I}} r_i$, achieved by the proposed spectrum allocation scheme with ASB while considering the proposed spectrum allocation scheme with ESB as the benchmark. We clarify that in the benchmark scheme, (i) ESB is considered, (ii) the sub-bands are optimally assigned to users while satisfying the constraints (3.9i), (3.9j), and (3.9k), and (iii) the transmit power is allowed to vary while satisfying the constraints (3.9b) and (3.9c). We clarify that for the two schemes, b^{τ}_{Δ} is fixed at b^{τ}_{*}, where b^{τ}_{*} denotes the bandwidth of the spectrum at the edges of each region where the molecular absorption coefficient is higher than

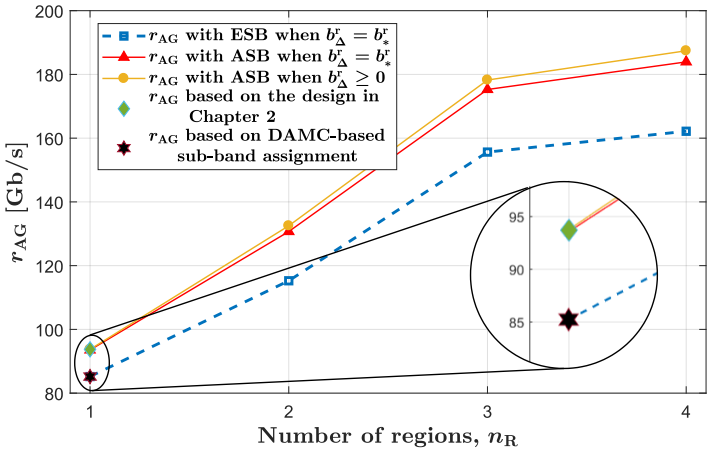

Figure 3.4: Aggregated multiuser data rate versus the number of spectrum regions within the to-be-allocated spectrum.

0.3 [68]. We observe that for all power budget values, a significantly higher r_{AG} (between 12% and 15%) can be achieved by adopting ASB by varying the sub-band bandwidths. Next, we compare r_{AG} achieved by the proposed spectrum allocation scheme with ASB when $b^{\tau}_{\Delta} \geq 0$ and $b^{\tau}_{\Delta} = b^{\tau}_{*}$, and then plot the data rate gain of considering $b^{\tau}_{\Delta} \geq 0$ relative to considering $b^{\tau}_{\Delta} = b^{\tau}_{*}$, Δr_{AG}. We observe that although Δr_{AG} is marginal when the power budget is high, a noticeable data rate gain Δr_{AG} ($\approx 5\%$) exists when the power budget constraint is stringent. These two observations show the significance of considering ASB and $b^{\tau}_{\Delta} \geq 0$. We further observe in Fig. 3.3(b) that the average value of the unused bandwidth within regions, $E[b^{\tau}_{\Delta}]$, increases when the power budget decreases, which explains the increasing Δr_{AG} when the power budget decreases.

In order to examine the efficiency of the sub-band assignment design introduced in the proposed spectrum allocation scheme, we plot r_{AG} versus the number of regions, n_R, in Fig. 3.4.[1] We also plot r_{AG} achieved by (i) the proposed spectrum allocation scheme while considering ESB for all n_R values, (ii) the spectrum

[1]Here, the regions corresponding to n_R of 1, 2, 3, and 4 are $\{sr_2^p\}$, $\{sr_2^p + sr_2^n\}$, $\{sr_2^p + sr_2^n + sr_3^p\}$, and $\{sr_2^p + sr_2^n + sr_3^p + sr_3^n\}$, respectively. For the sake of fairness, we made the number of users in the system to be proportional to the total available bandwidth within the to-be-allocated spectrum. More precisely, the number of users corresponding to n_R of 1, 2, 3, and 4 are 10, 17, 27, and 30, respectively.

allocation scheme proposed in [32] where DAMC-based sub-band assignment is considered, and (iii) using the design presented in Chapter 2. We first observe that when $n_{\mathrm{R}} = 1$, r_{AG} achieved by the proposed spectrum allocation scheme while considering ESB, is equal to that achieved by the spectrum allocation scheme that considers DAMC-based sub-band assignment. This shows that although DAMC-based sub-band assignment is a heuristic technique, it is applicable to obtain the near-optimal solution to the sub-band assignment problem at the THz band when the to-be-allocated spectrum is entirely within a TW. Despite this, we clarify that DAMC-based sub-band assignment is only readily applicable within a TW; thus, the sub-band assignment design introduced in the proposed spectrum allocation scheme needs to be considered when the to-be-allocated spectrum is composed of multiple TWs. We next observe that when $n_{\mathrm{R}} = 1$, r_{AG} achieved by the proposed scheme in this chapter is equal to that achieved by the design presented in Chapter 2, which is only applicable when the to-be-allocated spectrum is entirely within a region. This shows that the scheme investigated in Chapter 2 is a special case of the proposed multi-band-based spectrum allocation scheme in this chapter. Finally, similar to that in Fig. 3.3, we observe that (i) consideration of ASB leads to a significantly higher data rate as compared to the consideration of ESB and (ii) an additional gain can be achieved by considering $b_{\Delta}^{\tau} \geq 0$ as compared to $b_{\Delta}^{\tau} = b_{*}^{\tau}$.

In Fig. 3.5, we show how the spectral resources are allocated according to the proposed multi-band-based allocation scheme. We plot the allocation of spectral resources within the transmission window, TW_2. We note that the gray bars represent the sub-bands and the width and the height of the bars represent the bandwidth of the sub-bands and the transmission distance of the users assigned to the sub-bands, respectively. We first observe that, according to the optimal sub-band assignment configuration, the users with longer distances are assigned to center sub-bands where the absorption loss is low while the users with shorter distances are assigned to edge sub-bands where the absorption loss is high. This shows that, since the absorption loss increases exponentially with distance, the data rate gain achieved by the users with longer distances, through occupying the center sub-bands as compared to occupying the edge sub-bands, is higher than the data rate loss incurred by the users with shorter distances, through occupying the edge sub-bands as compared to occupying the center sub-bands. We clarify that

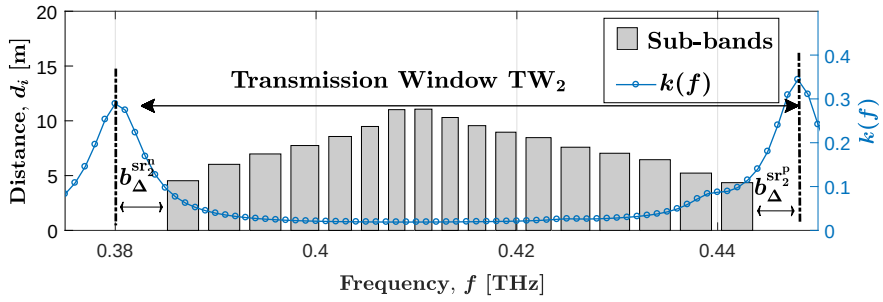

Figure 3.5: Illustration of the allocation of spectral resources within the transmission window TW_2.

this sub-band assignment configuration is similar to the DAMC-based sub-band assignment scheme proposed in [32] which is only readily applicable within a TW. We also observe that although the edge sub-bands experience higher absorption losses, a wider bandwidth is allocated to the edge sub-bands compared to the center sub-bands, since the edge sub-bands are occupied by the users with shorter distances.

Finally, we illustrate the improvement in the feasibility region of the problem $\mathbf{P_2^o}$ that occurs as a result of considering ASB and $b_\Delta^\tau \geq 0$. To this end, Fig. 3.6 plots the percentage of simulation trails for which the problem $\mathbf{P_2^o}$ is feasible, Ψ, for the proposed spectrum allocation scheme while considering (i) ASB and $b_\Delta^\tau \geq 0$, (ii) ASB and $b_\Delta^\tau = b_*^\tau$, and (iii) ESB and $b_\Delta^\tau = b_*^\tau$. We first observe that Ψ increases when power budget, p_{tot}, and rate threshold, r_{thr}, increases and decreases, respectively. This is expected because the increase in p_{tot} and the decrease in r_{thr} will lead to the constraints (3.9b) and (3.9g) in $\mathbf{P_2^o}$ to be less stringent, thereby leading to more opportunities to attain a feasible solution to $\mathbf{P_2^o}$. Second, we observe that our consideration of ASB increases Ψ as compared to considering ESB. Third, we observe that our consideration of $b_\Delta^\tau \geq 0$ increases Ψ as compared to considering $b_\Delta^\tau = b_*^\tau$. The second and third observations are due to the fact that considering ASB and $b_\Delta^\tau \geq 0$ allows sub-band bandwidth to vary and some spectra that exist at the edges of TWs to be avoided from utilization during spectrum allocation, respectively, if that can yield a feasible solution point. This again shows the importance of our considerations of ASB and $b_\Delta^\tau \geq 0$ during spectrum allocation.

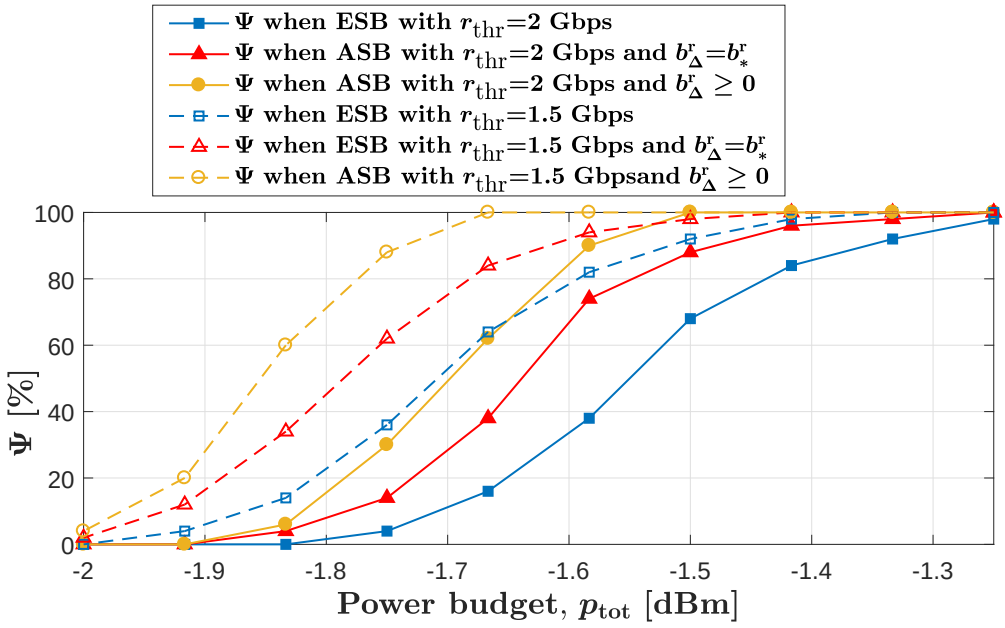

Figure 3.6: Illustration of the variation of the percentage of the simulation trails for which the problem $\mathbf{P_2^o}$ is feasible, Ψ, versus the power budget.

3.6 Summary

This chapter investigated the benefits of sub-band assignment, ASB, and optimally determining the unused spectra at the edges of TWs during multi-band-based spectrum allocation in THzCom systems when the to-be-allocated spectrum is composed of multiple TWs. We first formulated an optimization problem, with the main focus on spectrum allocation. Thereafter, to solve the formulated problem, we proposed transformations, as well as modifications, and developed iterative algorithms based on the SCA technique. Using numerical results, we showed that the sub-band assignment design proposed in this chapter needs to be considered when the to-be-allocated spectrum is composed of multiple TWs, since DAMC-based sub-band assignment is only readily applicable within a TW. We also showed that additional gains can be obtained by adopting ASB and optimally determining the unused spectra at the edges of TWs as compared to adopting ESB and avoiding using pre-defined spectra that exist at the edges of TWs, respectively. We finally showed that the feasibility region of the resource allocation problem can be im-

proved by adopting ASB and optimally determining the unused spectra at the edges of TWs.

We clarify that the solution to the spectrum allocation problem with ASB proposed in this chapter is only applicable when the molecular absorption coefficient within TWs can be modeled using exponential functions of the frequency with minimal approximation errors. Nevertheless, to harness the potentials of all TWs/spectrum regions within the THz band, it is necessary to develop a solution to the spectrum allocation problem with ASB when the molecular absorption coefficient varies in a highly non-linear manner within TWs and cannot be modeled using exponential functions of frequencies, which is the case in many spectrum regions within the THz band. This consideration will be addressed in the subsequent technical chapter.

Chapter 4

An Unsupervised Learning Approach for Spectrum Allocation in THzCom Systems

4.1 Introduction

In this technical chapter, we explore the design of multi-band-based spectrum allocation with adaptive sub-band bandwidth (ASB) for multiuser terahertz (THz) band communication systems when the molecular absorption coefficient varies in a highly non-linear manner such that it cannot be modeled as a piecewise exponential function of frequencies. We clarify that designs in Chapters 2 and 3 are only applicable when the molecular absorption coefficient within the to-be-allocated spectrum is simple such that it can be modeled as a piecewise exponential function of frequency with minimal approximation errors. As discussed in Section 2.5.1, in many spectrum regions within the THz band, the molecular absorption coefficient varies in a highly non-linear manner; thus, it cannot be modeled as a piecewise exponential function of frequencies in such spectrum regions. This motivates this chapter, where we resort to unsupervised learning to obtain a near-optimal solution to the multi-band-based spectrum allocation problem with ASB.

We focus on a scenario where a single access point (AP) supports the downlink transmission of multiple users in the presence of dynamic human blockers. In this

chapter, we do not put any limitation on whether or not the variation of molecular absorption loss within the to-be-allocated spectrum can be modeled as an exponential function of frequency with minimal approximation errors. For this system, we formulate an optimization problem, with the main emphasis on multi-band-based spectrum allocation with ASB, while aiming to maximize the throughput of the multiuser THzCom system under given constraints on sub-band bandwidth and power. We then propose an unsupervised learning-based approach to obtaining a near-optimal solution to the formulated optimization problem. In the proposed approach, we first train a deep neural network (DNN) where a loss function inspired by the Lagrangian of the formulated optimization problem is used. Thereafter, using the trained DNN, we approximate the near-optimal solution to the formulated optimization problem. Using numerical results, we demonstrate that when the values of the molecular absorption coefficient within the to-be-allocated spectrum can be modeled as an exponential function of frequency, the throughput obtained by the proposed unsupervised learning-based approach converges to that achieved by the convex-optimization-based designs presented in Chapters 2 and 3. We also demonstrate that when the values of the molecular absorption coefficient within the to-be-allocated spectrum change rapidly and thus cannot be modeled as an exponential function of frequency, the proposed unsupervised learning-based approach outperforms the existing approximate approaches. We also show that the throughput of the spectrum allocation strategy decreases with the increasing density of human blockers.

The rest of the chapter is organized as follows. Section 4.2 introduces the system model and the associated resource allocation problem. Section 4.3 presents the unsupervised learning-based solution approach adopted to solve the formulated resource allocation problem. Section 4.4 presents the numerical results and Section 4.5 summarises the chapter.

4.2 System Model and Problem Formulation

In this section, we first introduce the notations used in this chapter. We then introduce the system model by specifying the system deployment, THz spectrum, achievable data rate, and performance metrics of interest. Finally, we introduce

the considered resource allocation problem.

4.2.1 Notations

Matrices and column vectors are denoted by uppercase and lowercase boldface symbols, respectively. Scalar variables are denoted by italic symbols. Given a matrix $\mathbf{A}$, $\mathbf{A}_{\mathrm{m}}$ denotes the mth row vector of $\mathbf{A}$. Given a column vector $\mathbf{a}$, $\mathbf{a}^{\mathrm{T}}$ and a_{m} denote the transpose and the mth element of $\mathbf{a}$, respectively. Moreover, $\mathbf{I}_m$ and $\mathbf{L}_m$ denote $m \times m$ identity matrix and $m \times m$ lower triangular matrix with all non-zero values as 1, respectively. Furthermore, $\mathbf{1}_m$ denotes the $m \times 1$ vector with all entries as 1. The curled inequality symbols, e.g., $\preceq$, denote generalized inequalities, i.e., componentwise inequality between vectors.

4.2.2 System Deployment

We consider a three-dimensional (3D) indoor THzCom system, as shown in Fig. 1.3, where the high data rate demands of n_{I} users are supported by a single AP. We consider that the users are stationary and distributed uniformly on the floor in the indoor environment. We denote $\mathbf{l}$ and $\mathbf{d}$ as the $n_{\mathrm{I}} \times 1$ the horizontal and 3D communication distance vectors of the AP-user channels, with $d_i = \sqrt{(h_{\mathrm{A}} - h_{\mathrm{U}})^2 + l_i^2}$, and h_{A} and h_{U} are the heights of AP and the users, respectively. For notational convenience, we consider that the elements in $\mathbf{d}$ are ordered such that $d_1 < d_2 < \cdots < d_{n_{\mathrm{I}}}$.

The extremely short wavelengths of THz signals make the THz signal propagation to be highly vulnerable to blockages [29]. In our system, we consider moving humans act as potential impenetrable blockers. We model the human blockers by rectangular absorbing screens (commonly referred to as the double knife-edge (DKE) model) with heights h_{B} and widths $L_{\mathrm{B},1}$ and $L_{\mathrm{B},2}$ [123, 124]. Furthermore, we assume that the locations of humans form a Poisson point process (PPP) with the density of λ_{B} and their mobility follows the random directional (RD) model [125]. Based on the RD model, a moving human randomly selects a direction in $(0, 2\pi)$ to travel in and a duration for this travel. At the end of this duration, another independent direction to travel in and a time duration for this travel are selected, and the pattern continues. Following [71, 82, 126, 127], we assume that the

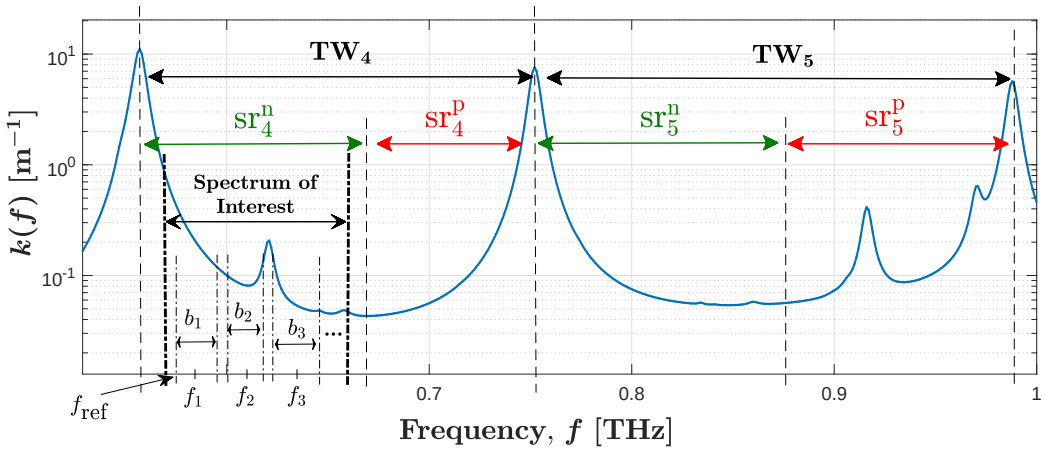

Figure 4.1: Illustration of (i) PACSRs and NACSRs that exist between 0.5 THz and 1 THz with $\{\text{TW}_4, \text{TW}_5\}$, $\{\text{sr}_4^{\text{p}}, \text{sr}_5^{\text{p}}\}$, and $\{\text{sr}_4^{\text{n}}, \text{sr}_5^{\text{n}}\}$ denoting the TWs, PACSRs, and NACSRs, respectively, and (ii) sub-band arrangement within the to-be-allocated spectrum.

moving speeds of all human blockers are v_{B}. Also, for the sake of practicality, we assume that $h_{\text{A}} > h_{\text{B}} > h_{\text{U}}$ in the considered system.

4.2.3 THz Spectrum

Without loss of generality, in this chapter, we focus on the scenario when the to-be-allocated spectrum exists within a negative absorption coefficient slope region (NACSR) of a transmission window (TW), as depicted in Fig. 4.1. However, we note that the design principles presented in this chapter can be extended even if the to-be-allocated spectrum exists within a positive absorption coefficient slope region (PACSR) or spans multiple TWs.

We focus on multi-band-based spectrum allocation with ASB. Thus, we divide the to-be-allocated spectrum into n_{S} sub-bands that are of unequal bandwidths and separated by guard bands. We denote $\mathbf{b}$ and $\mathbf{f}$ as the $n_{\text{S}} \times 1$ vectors of the bandwidth and the center frequency of the sub-bands, respectively. For notational convenience, we label the sub-bands such that $f_1 < f_2 < \cdots < f_{n_{\text{S}}}$, as shown in

Fig. 4.1. Thus, we have

$$\begin{aligned} f_s &= f_{\text{ref}} + \sum_{k=1}^{s} b_k + (s-1)B_{\text{g}} - \frac{1}{2}b_s \\ &= \mathbf{A}_s\mathbf{b} + \widetilde{f}_{\text{ref},s}, \end{aligned} \tag{4.1}$$

where B_{g} is the fixed bandwidth of guard bands, and f_{ref} is the start frequency of the to-be-allocated spectrum, as shown in Fig. 4.1, and $\widetilde{f}_{\text{ref},s} = f_{\text{ref}} - (s-1)B_{\text{g}}$. Here, $\mathbf{A}$ is an $n_{\text{S}} \times n_{\text{S}}$ matrix with $\mathbf{A} = \mathbf{L}_{n_{\text{S}}} - \frac{1}{2}\mathbf{I}_{n_{\text{S}}}$. Due to the consideration of ASB, we have

$$0 \preceq \mathbf{b} \preceq b_{\max}, \tag{4.2}$$

where $b_{\max}$ denotes the upper bound on bandwidth of the sub-band. We then denote b_{tot} as the total available bandwidth within the to-be-allocated spectrum and express it as[1]

$$b_{\text{tot}} = \mathbf{1}_{n_{\text{S}}}^{\text{T}}\mathbf{b} + (n_{\text{S}} - 1)B_{\text{g}}. \tag{4.3}$$

Similar to that in [32, 46, 50] and Chapters 2 and 3, we assume that the users in the system are served by separate sub-bands. The justification behind this consideration is given in Section 2.2.3. Considering this assumption, we set the total number of sub-bands within the to-be-allocated spectrum to be equal to the total number of users in the system, i.e., $n_{\text{S}} = n_{\text{I}}$. Also, following [32, 51, 52] and Chapter 2, we adopt in this chapter distance-aware multi-carrier (DAMC)-based sub-band assignment to improve the throughput fairness among users. The DAMC-based sub-band assignment assigns (i) the sub-bands with high absorption coefficients to the users with shorter distances and (ii) the sub-bands with low absorption coefficients to the users with longer distances.

[1] Without of loss of generality, in this chapter we consider that the to-be-allocated spectrum is fully utilized during spectrum allocation. However, we note that the design principles presented in this chapter can be extended even if the spectrum that is to be utilized is determined optimally for spectrum allocation, as in Chapter 3.

4.2.4 Achievable Data Rate

The instantaneous achievable rate by the user assigned to sth sub-band is obtained as

$$r_s(t) = \begin{cases} r_s^{\mathrm{nb}}, & \text{with the probability of } \rho_s^{\mathrm{nb}}, \\ r_s^{\mathrm{b}}, & \text{with the probability of } (1-\rho_s^{\mathrm{nb}}), \end{cases} \qquad \forall s \in \mathcal{S}, \tag{4.4}$$

where r_s^{nb} and r_s^{b} are the achievable rates of the user assigned to sth sub-band, when the AP to the user link is not blocked and blocked by dynamic blockers, respectively. We clarify that $r_s^{\mathrm{b}} = 0$ since it is considered that the blockers are impenetrable.

Considering the spreading and molecular absorption loss, r_s^{nb} is written as [29]

$$r_s^{\mathrm{nb}} = \int_{f_s-\frac{1}{2}b_s}^{f_s+\frac{1}{2}b_s} \log_2\left(1 + \frac{p_s \varrho e^{-k(f)d_s}}{f^2 d_s^2 b_s}\right) \mathrm{d}f, \tag{4.5}$$

where $\varrho = \frac{G_{\mathrm{A}} G_{\mathrm{U}}}{N_0}\left(\frac{c}{4\pi}\right)^2$, G_{A} and G_{U} are the antenna gains at the AP and users, respectively, N_0 is the noise power density, c is the speed of light, and $k(f)$ is the molecular absorption coefficient at f. Furthermore, $\mathbf{p}$ denotes the $n_{\mathrm{S}} \times 1$ transmit power vector. It is noted that similar to that in Chapters 2 and 3, in this chapter, we (i) ignore the impact of non-line-of-sight (nLoS) rays and focus only on the line-of-sight (LoS) rays of THz signals [62, 69, 72, 73, 75, 86–88], (ii) omit the impact of fading in the THz channel [62, 69, 72–75, 86–88, 113], and (iii) consider inter-band interference (Inter-BI) and intra-band interference (Intra-BI) free transmission [32, 46, 50, 50, 114]. The justifications behind these considerations are given in Section 2.2.4.

4.2.5 Performance Metrics of Interest

4.2.5.1 Non-blockage Probability

We denote $\boldsymbol{\rho}$ as the $n_{\mathrm{S}} \times 1$ non-blockage probability vector of users and obtain the values of its elements using the following lemma.

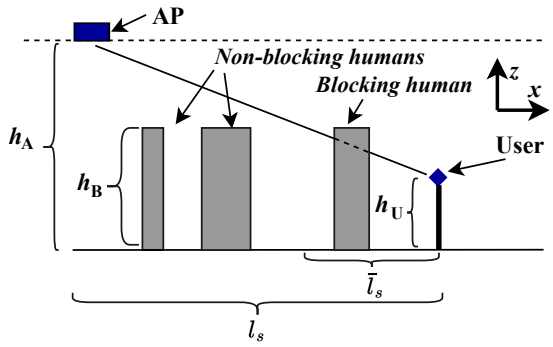

(a) Side view

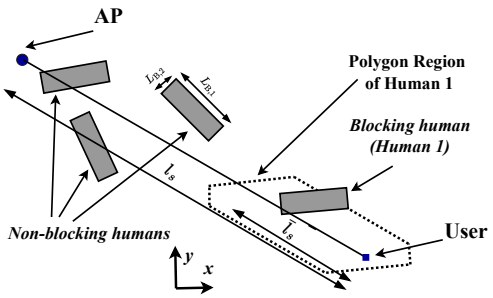

(b) Top view

Figure 4.2: Illustration of the AP to a single user link in the presence of dynamic human blockers.

Lemma 4.1 *The non-blockage probability of the link between the AP and the user assigned to sth sub-band is derived as*

$$\rho_s^{nb} = \zeta e^{-\widetilde{\lambda}_B l_s}, \tag{4.6}$$

where $\zeta = e^{-2L_{B,1}L_{B,2}\lambda_B}$ *and* $\widetilde{\lambda}_B = \frac{2(L_{B,1}+L_{B,2})\lambda_B(h_B-h_U)}{\pi(h_A-h_U)}$.

Proof: The proof is based on Fig. 4.2 and is presented in Appendix B.1. ■

4.2.5.2 Throughput

We denote $\mathbf{r}$ as the $n_{\mathrm{S}} \times 1$ long-term[2] throughput vector of users. Considering (4.4), the long-term throughput achieved by the user assigned to sth sub-band can be derived from

$$r_s = \lim_{T\to\infty} \frac{1}{T} \int_0^T r_s(t)\ \mathrm{d}t, \qquad \forall i \in \mathcal{I}, \tag{4.7}$$

where T is time. We next substitute (4.4) in (4.7) to obtain

$$\begin{aligned} r_s &= \lim_{T\to\infty} \frac{1}{T} \int_0^T r_s(t)\ \mathrm{d}t \\ &= \left(\rho_s^{\mathrm{nb}} r_s^{\mathrm{nb}} + \left(1-\rho_s^{\mathrm{nb}}\right)\right) r_s^{\mathrm{b}}\big) \\ &= \rho_s^{\mathrm{nb}} r_s^{\mathrm{nb}}, \end{aligned} \tag{4.8}$$

where ρ_s^{nb} and r_s^{nb} are given in (4.6) and (4.5), respectively.

4.2.6 Optimal Resource Allocation

We now design an efficient spectrum allocation strategy to harness the potential of the THz band. To this end, we study spectrum allocation with ASB to maximize the long-term throughput under given constraints on sub-band bandwidth and power. Mathematically, the problem is formulated as

$$\begin{aligned} \mathbf{P_3^o}: \quad & \underset{\mathbf{p},\mathbf{b}}{\text{maximize}} && \mathcal{E}(\mathbf{d},\mathbf{p},\mathbf{b}) && \text{(4.9a)} \\ & \text{subject to} && \mathbf{1}_{n_{\mathrm{S}}}^{\mathrm{T}}\mathbf{p} \leqslant p_{\mathrm{tot}}, && \text{(4.9b)} \\ & && 0 \preceq \mathbf{p} \preceq p_{\max}, && \text{(4.9c)} \\ & && \mathbf{1}_{n_{\mathrm{S}}}^{\mathrm{T}}\mathbf{b} = \overline{b}_{\mathrm{tot}}, && \text{(4.9d)} \\ & && 0 \preceq \mathbf{b} \preceq b_{\max}. && \text{(4.9e)} \end{aligned}$$

[2]We define the long-term value of a function as the average of the instantaneous values of this function over a relatively long-time duration. Specifically, the long-term value of the function Υ is given by $\Upsilon = \lim_{T\to\infty} \frac{1}{T}\int_0^T \Upsilon(t)\ \mathrm{d}t$, where $\Upsilon(t)$ is the instantaneous value of the function Υ at time instant t.

In $\mathbf{P_3^o}$, $\mathcal{E}(\mathbf{d}, \mathbf{p}, \mathbf{b})$ is the objective function of the considered long-term throughput maximization strategy. In this chapter, we consider proportional-fair long-term throughput maximization, which leads to $\mathcal{E}(\mathbf{d}, \mathbf{p}, \mathbf{b}) = \mathbf{1}_{n_S}^{\mathrm{T}} \log(\mathbf{r})$. Moreover, (4.9b) and (4.9c) are the power budget at the AP and the upper bound on the power allocated to each user, respectively. Finally, the justifications on (4.9d) and (4.9e) are given by (4.3) and (4.2), respectively, where $\overline{b}_{\mathrm{tot}} = b_{\mathrm{tot}} - (n_S - 1)B_g$.

We clarify that in Chapters 2 and 3, the multi-band-based spectrum allocation with ASB was studied and solution approaches to optimization problems similar to $\mathbf{P_3^o}$ were discussed. However, we note that the designs in Chapters 2 and 3 are only applicable when $k(f)$ within the to-be-allocated spectrum is simple such that it can be modeled as a piecewise exponential function of frequency with minimal approximation errors. As discussed in Section 2.5.1, in many spectrum regions within the THz band, $k(f)$ varies in a highly non-linear manner; thus, it cannot be modeled as a piecewise exponential function of frequencies in such spectrum regions. It follows that designs in Chapters 2 and 3 cannot be adopted in such spectrum regions. Motivated by this, in this chapter, we resort to unsupervised learning to obtain the near-optimal solution to $\mathbf{P_3^o}$ [66, 67]. In the next section, we present the unsupervised learning-based solution adopted in this chapter.

4.3 Unsupervised Learning-based Solution

In this section, we present an unsupervised learning-based approach to solving problem $\mathbf{P_3^o}$ in (4.5). In this approach, we first employ an *offline training phase* to train a DNN, utilizing (i) a loss function which is inspired by the objective function of the dual problem of $\mathbf{P_3^o}$ and (ii) a batch of realizations of distance vectors. Thereafter, during the *implementation phase*, we use the trained DNN to approximate the optimal solution to $\mathbf{P_3^o}$ for the given distance vector. Next, we will discuss the architecture of the adopted DNN in Section 4.3.1, and the unsupervised learning model used in the training phase in Section 4.3.2.

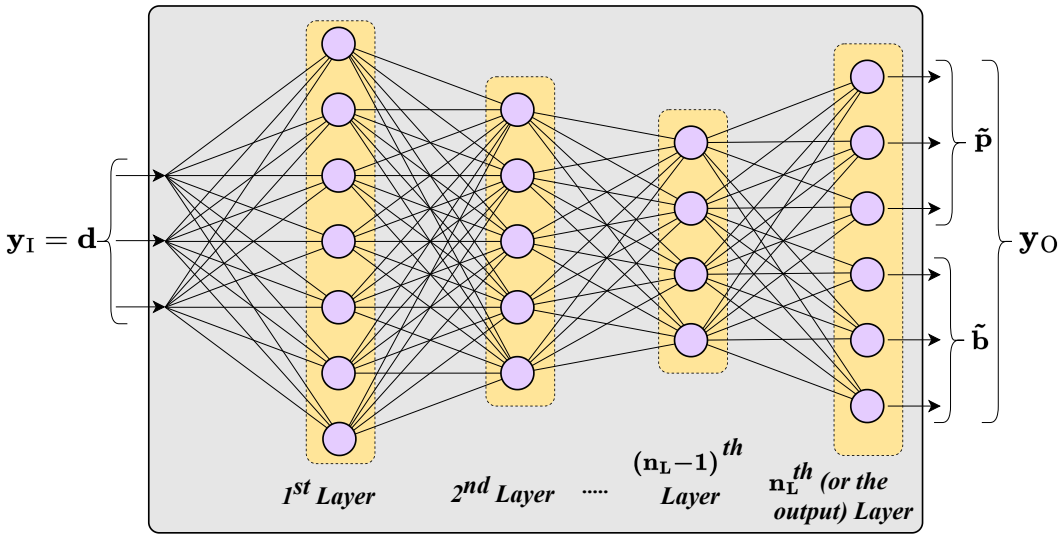

Figure 4.3: Illustration of the general architecture of the DNN when $n_\mathrm{L} = 4$ and $n_\mathrm{S} = 3$.

4.3.1 Architecture of the DNN

The general architecture of the adopted DNN is presented in Fig. 4.3. The DNN consists of n_L fully-connected layers with multiple neurons in every layer. Each neuron in the network contains a linear operation, which is followed by a point-wise non-linearity, also known as an activation function. Considering this, the output of the network, $\mathbf{y}_\mathrm{O}$, is expressed as a non-linear function to the input of the network, $\mathbf{y}_\mathrm{I}$, which is given by

$$\mathbf{y}_\mathrm{O} = \mathcal{N}(\mathbf{y}_\mathrm{I}, \boldsymbol{\Theta}) = \digamma_\mathrm{L}^{(n_\mathrm{L})}\left(\digamma_\mathrm{L}^{(n_\mathrm{L}-1)}\left(\cdots \digamma_\mathrm{L}^{(1)}\left(\mathbf{y}_\mathrm{I}\right)\right)\right). \tag{4.10}$$

Here, $\boldsymbol{\Theta} = \{\boldsymbol{\varpi}^{(\ell)}, \beta^{(\ell)}, \ell \in \{1, 2, \cdots, n_\mathrm{L}\}\}$, denotes the set of parameters (i.e., weights and biases) of the DNN, and $\boldsymbol{\varpi}^{(\ell)}$ and $\beta^{(\ell)}$ are the weights vector and the bias of the ℓth layer, respectively, and $\digamma^{(\ell)}(\cdot)$ is the function that maps the input and output of the ℓth layer. Also, we have

$$\digamma^{(\ell)}(\boldsymbol{\chi}) = \digamma_\mathrm{A}^{(\ell)}\left((\boldsymbol{\varpi}^{(\ell)})^\mathrm{T}\boldsymbol{\chi} + \beta^{(\ell)}\right), \tag{4.11}$$

where $\digamma_\mathrm{A}^{(\ell)}(\cdot)$ is the activation function of the ℓth layer.

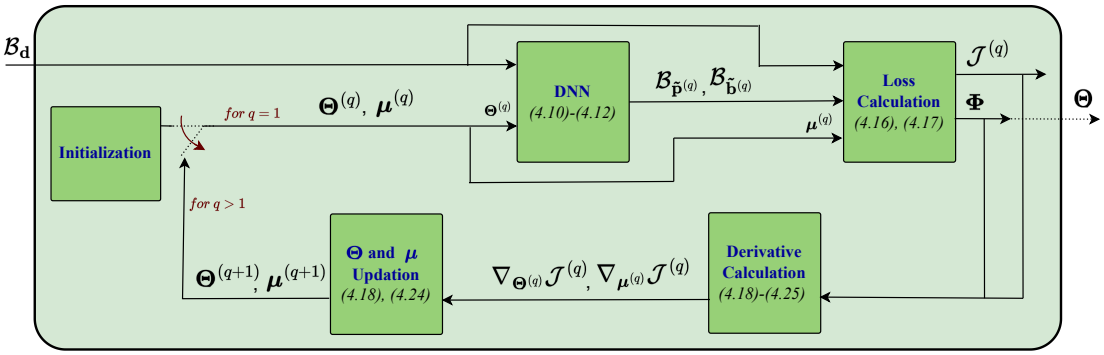

Figure 4.4: Block diagram representation of the unsupervised learning model. Here, $\mathcal{B}_{\widetilde{\mathbf{p}}^{(q)}}$ and $\mathcal{B}_{\widetilde{\mathbf{b}}^{(q)}}$ are the batches of $\widetilde{\mathbf{p}}$ and $\widetilde{\mathbf{b}}$ obtained as the output of DNN at the qth iteration, and $\boldsymbol{\Phi} = \{\mathcal{B}_{\widetilde{\mathbf{p}}^{(q)}}, \mathcal{B}_{\widetilde{\mathbf{b}}^{(q)}}, \boldsymbol{\Theta}^{(q)}, \boldsymbol{\mu}^{(q)}\}$ denotes the cache of the unsupervised learning model.

During the *implementation phase*, we provide $\mathbf{d}$ as the input to the DNN and obtain the output as the approximated values of the optimization variables of $\mathbf{P}^{\mathbf{o}}_{\mathbf{3}}$, which are denoted by $\widetilde{\mathbf{p}}$ and $\widetilde{\mathbf{b}}$. Therefore, we have

$$\mathbf{y}_{\mathrm{I}} = \mathbf{d} \quad \text{and} \quad \mathbf{y}_{\mathrm{O}} = \begin{bmatrix} \widetilde{\mathbf{p}} \\ \widetilde{\mathbf{b}} \end{bmatrix}. \tag{4.12}$$

4.3.2 Unsupervised Learning Model

The block diagram representation of the unsupervised learning model used in the training phase is depicted in Fig. 4.4. The unsupervised learning model takes a batch of realization of the distance vector, $\mathcal{B}_{\mathbf{d}}$, as the input, and delivers the trained $\boldsymbol{\Theta}$ as the output. We note that the unsupervised learning model iteratively updates $\boldsymbol{\Theta}$ to ensure the best mapping being obtained between $\mathcal{B}_{\mathbf{d}}$ and the near-optimal solution to $\mathbf{P}^{\mathbf{o}}_{\mathbf{3}}$ for the given $\mathcal{B}_{\mathbf{d}}$.

4.3.2.1 Loss Function

The loss function of the unsupervised learning model is inspired by the objective function of the dual problem of $\mathbf{P}^{\mathbf{o}}_{\mathbf{3}}$. Specifically, the dual problem of $\mathbf{P}^{\mathbf{o}}_{\mathbf{3}}$ is given

by

$$\mathbf{P^o_{3,D}}: \ \underset{\boldsymbol{\mu},\boldsymbol{\Gamma}}{\text{maximize}} \ \min_{\mathbf{p},\mathbf{b}} \mathcal{L}_{\text{o}} \tag{4.13a}$$

$$\text{subject to} \quad (4.9\text{b}) - (4.9\text{e})$$

$$\boldsymbol{\mu}, \boldsymbol{\Gamma} \succeq 0, \tag{4.13b}$$

where

$$\begin{aligned}\mathcal{L}_{\text{o}} &= \mathcal{L}_{\text{o}}(\mathbf{d}, \mathbf{p}, \mathbf{b}, \boldsymbol{\mu}, \boldsymbol{\Gamma}) \\ &= -\mathcal{E}(\mathbf{d}, \mathbf{p}, \mathbf{b}) + \mu_1 \left(\mathbf{1}_{n_{\text{S}}}^{\text{T}} \mathbf{p} - p_{\text{tot}}\right) + \mu_2 \left(\mathbf{1}_{n_{\text{S}}}^{\text{T}} \mathbf{b} - \overline{b}_{\text{tot}}\right) + \boldsymbol{\Gamma}_1^{\text{T}}(0 - \mathbf{p}) \\ &\quad + \boldsymbol{\Gamma}_2^{\text{T}}(\mathbf{p} - p_{\max}) + \boldsymbol{\Gamma}_3^{\text{T}}(0 - \mathbf{b}) + \boldsymbol{\Gamma}_4^{\text{T}}(\mathbf{b} - b_{\max}),\end{aligned} \tag{4.14}$$

is the Lagrangian of $\mathbf{P^o_3}$, and $\boldsymbol{\mu} = [\mu_1, \mu_2]^{\text{T}}$ and $\boldsymbol{\Gamma} = [\boldsymbol{\Gamma_1}, \boldsymbol{\Gamma_2}, \boldsymbol{\Gamma_3}, \boldsymbol{\Gamma_4}]$ are the Lagrange multipliers associated with the constraints of $\mathbf{P^o_3}$. In our unsupervised learning model, using the DNN which is parameterized by $\boldsymbol{\Theta}$, the design variables $\mathbf{p}$ and $\mathbf{b}$ are approximated as $\widetilde{\mathbf{p}}$ and $\widetilde{\mathbf{b}}$, respectively. Considering this, the problem $\mathbf{P^o_{3,D}}$ can be formulated into the following variable optimization as

$$\widehat{\mathbf{P}}^{\mathbf{o}}_{\mathbf{3}}: \ \underset{\boldsymbol{\mu}}{\text{maximize}} \ \min_{\boldsymbol{\Theta}} \widehat{\mathcal{L}}_{\text{o}} \tag{4.15a}$$

$$\text{subject to} \quad (4.9\text{b}), (4.9\text{d}),$$

$$\boldsymbol{\mu} \succeq 0, \tag{4.15b}$$

where

$$\begin{aligned}\widehat{\mathcal{L}}_{\text{o}} &= \widehat{\mathcal{L}}_{\text{o}}(\mathbf{d}, \widetilde{\mathbf{p}}, \widetilde{\mathbf{b}}, \boldsymbol{\mu}) \\ &= -\mathcal{E}(\mathbf{d}, \widetilde{\mathbf{p}}, \widetilde{\mathbf{b}}) + \mu_1 \left(\mathbf{1}_{n_{\text{S}}}^{\text{T}} \widetilde{\mathbf{p}} - p_{\text{tot}}\right) + \mu_2 \left(\mathbf{1}_{n_{\text{S}}}^{\text{T}} \widetilde{\mathbf{b}} - \overline{b}_{\text{tot}}\right).\end{aligned} \tag{4.16}$$

In (4.16), $\widehat{\mathcal{L}}_{\text{o}}$ is obtained as a simplified version of $\mathcal{L}_{\text{o}}$ given in (4.14). This is because the satisfaction of constraints (4.9c) and (4.9e) can be guaranteed by carefully choosing appropriate activation functions for the neurons in the n_{L}th (or the output) layer of the DNN, e.g., $\digamma_{\text{A}}^{(n_{\text{L}})}(\cdot) = \Xi \times S(\cdot)$, where $S(\cdot)$ is the sigmoid function, and $\Xi = p_{\max}$ and $\Xi = b_{\max}$ for the first and the second n_{S} neurons of the

output layer, respectively.

We note that the optimal value of $\mathbf{P}^{\mathbf{o}}_{\mathbf{3},\mathbf{D}}$ might be a loose global lower bound on the optimal value of $\mathbf{P}^{\mathbf{o}}_{\mathbf{3}}$, since $\mathbf{P}^{\mathbf{o}}_{\mathbf{3}}$ is not a convex optimization problem. However, we also note that the design variables of $\mathbf{P}^{\mathbf{o}}_{\mathbf{3},\mathbf{D}}$ are approximated using a DNN in our unsupervised learning model, and $\widehat{\mathbf{P}}^{\mathbf{o}}_{\mathbf{3}}$ aims to optimize the DNN parameters, $\boldsymbol{\Theta}$. Thus, it can be concluded based on the universal approximation theorem that the optimal value of $\widehat{\mathbf{P}}^{\mathbf{o}}_{\mathbf{3}}$ provides a tight lower bound on the optimal value of $\mathbf{P}^{\mathbf{o}}_{\mathbf{3}}$ [66,67]. Based on this conclusion and considering that a batch of realization of $\mathbf{d}$, $\mathcal{B}_{\mathbf{d}}$, that is used during the training phase, we define the loss function of the unsupervised learning model, $\mathcal{J}$. Specifically, for each realization of $\mathbf{d}$ in $\mathcal{B}_{\mathbf{d}}$, we obtain the corresponding $\widehat{\mathcal{L}}_{\mathrm{o}}$, and then derive $\mathcal{J}$ as the mean of $\widehat{\mathcal{L}}_{\mathrm{o}}$ values. Mathematically, $\mathcal{J}$ is obtained as

$$\mathcal{J} = \mathcal{J}(\boldsymbol{\Theta}, \boldsymbol{\mu}) = \frac{1}{n_{\mathrm{T}}} \sum_{\mathbf{d} \in \mathcal{B}_{\mathbf{d}}} \widehat{\mathcal{L}}_{\mathrm{o}}, \tag{4.17}$$

where n_{T} is the total number of realizations of $\mathbf{d}$ in $\mathcal{B}_{\mathbf{d}}$. We then iteratively update $\boldsymbol{\Theta}$ and $\boldsymbol{\mu}$ with the objective of minimizing $\mathcal{J}$ to arrive at the near-optimal solution to $\mathbf{P}^{\mathbf{o}}_{\mathbf{3}}$.

4.3.2.2 Updating DNN Parameters and Lagrangian Multipliers

The DNN parameters, $\boldsymbol{\Theta}$, are updated according to

$$\begin{aligned} \boldsymbol{\Theta}^{(q+1)} &= \boldsymbol{\Theta}^{(q)} - \phi_{\Theta} \, \nabla_{\boldsymbol{\Theta}^{(q)}} \mathcal{J}^{(q)} \\ &= \boldsymbol{\Theta}^{(q)} - \frac{\phi_{\Theta}}{n_{\mathrm{T}}} \sum_{\mathbf{d} \in \mathcal{B}_{\mathbf{d}}} \left[\nabla_{\boldsymbol{\Theta}} \widehat{\mathcal{L}}_{\mathrm{o}} \right]_{\substack{\boldsymbol{\Theta}=\boldsymbol{\Theta}^{(q)}, \widetilde{\mathbf{p}}=\widetilde{\mathbf{p}}^{(q)}, \\ \widetilde{\mathbf{b}}=\widetilde{\mathbf{b}}^{(q)}, \boldsymbol{\mu}=\boldsymbol{\mu}^{(q)}}} \end{aligned} \tag{4.18}$$

where ϕ_{Θ} is the learning rate and $\boldsymbol{\Psi}^{(q)}$ is the qth iteration value of $\boldsymbol{\Psi}$, with $\boldsymbol{\Psi} \in \{\boldsymbol{\Theta}, \mathcal{J}, \widetilde{\mathbf{p}}, \widetilde{\mathbf{b}}, \boldsymbol{\mu}\}$. Considering the chain rule, we express $\nabla_{\boldsymbol{\Theta}} \widehat{\mathcal{L}}_{\mathrm{o}}$ in (4.18) as

$$\nabla_{\boldsymbol{\Theta}} \widehat{\mathcal{L}}_{\mathrm{o}} = \nabla_{\boldsymbol{\Theta}} \mathbf{y}_{\mathrm{O}} \begin{bmatrix} \nabla_{\widetilde{\mathbf{p}}} \widehat{\mathcal{L}}_{\mathrm{o}} \\ \nabla_{\widetilde{\mathbf{b}}} \widehat{\mathcal{L}}_{\mathrm{o}} \end{bmatrix}. \tag{4.19}$$

In (4.19), $\nabla_{\widetilde{\mathbf{p}}}\widehat{\mathcal{L}}_{\mathrm{o}}$ and $\nabla_{\widetilde{\mathbf{b}}}\widehat{\mathcal{L}}_{\mathrm{o}}$ can be derived as

$$\nabla_{\widetilde{\mathbf{p}}}\widehat{\mathcal{L}}_{\mathrm{o}} = -\nabla_{\widetilde{\mathbf{p}}}\mathcal{E}(\mathbf{d},\widetilde{\mathbf{p}},\widetilde{\mathbf{b}}) + \mu_1, \tag{4.20}$$

and

$$\nabla_{\widetilde{\mathbf{b}}}\widehat{\mathcal{L}}_{\mathrm{o}} = -\nabla_{\widetilde{\mathbf{b}}}\mathcal{E}(\mathbf{d},\widetilde{\mathbf{p}},\widetilde{\mathbf{b}}) + \mu_2, \tag{4.21}$$

respectively. Also, note that in (4.20) and (4.21), it is impossible to analytically derive $\nabla_{\widetilde{\mathbf{p}}}\mathcal{E}(\mathbf{d},\widetilde{\mathbf{p}},\widetilde{\mathbf{b}})$ and $\nabla_{\widetilde{\mathbf{b}}}\mathcal{E}(\mathbf{d},\widetilde{\mathbf{p}},\widetilde{\mathbf{b}})$, respectively. Hence, we numerically calculate the values of $\nabla_{\widetilde{\mathbf{p}}}\mathcal{E}(\mathbf{d},\widetilde{\mathbf{p}},\widetilde{\mathbf{b}})$ and $\nabla_{\widetilde{\mathbf{b}}}\mathcal{E}(\mathbf{d},\widetilde{\mathbf{p}},\widetilde{\mathbf{b}})$ by using

$$\nabla_{\widetilde{\mathbf{p}}}\mathcal{E}(\mathbf{d},\widetilde{\mathbf{p}},\widetilde{\mathbf{b}}) = \frac{\mathcal{E}(\mathbf{d},\widetilde{\mathbf{p}}+\delta_{\mathrm{D}}\widetilde{\mathbf{p}},\widetilde{\mathbf{b}}) - \mathcal{E}(\mathbf{d},\widetilde{\mathbf{p}},\widetilde{\mathbf{b}})}{\delta_{\mathrm{D}}\widetilde{\mathbf{p}}}, \tag{4.22}$$

and

$$\nabla_{\widetilde{\mathbf{b}}}\mathcal{E}(\mathbf{d},\widetilde{\mathbf{p}},\widetilde{\mathbf{b}}) = \frac{\mathcal{E}(\mathbf{d},\widetilde{\mathbf{p}},\widetilde{\mathbf{b}}+\delta_{\mathrm{D}}\widetilde{\mathbf{b}}) - \mathcal{E}(\mathbf{d},\widetilde{\mathbf{p}},\widetilde{\mathbf{b}})}{\delta_{\mathrm{D}}\widetilde{\mathbf{b}}}, \tag{4.23}$$

respectively, where δ_{D} is a very small positive number. We also note that in (4.19), $\nabla_{\boldsymbol{\Theta}}\mathbf{y}_{\mathrm{O}}$ can be calculated as a function of $\boldsymbol{\Theta}^{(q)}$ utilizing the chain rule. As for the Lagrangian multiplier, $\boldsymbol{\mu}$, it can be updated according to

$$\begin{aligned}\boldsymbol{\mu}^{(q+1)} &= \left[\boldsymbol{\mu}^{(q)} + \phi_\mu \, \nabla_{\boldsymbol{\mu}^{(q)}}\mathcal{J}^{(q)}\right]^+ \\ &= \left[\boldsymbol{\mu}^{(q)} + \frac{\phi_\mu}{n_{\mathrm{T}}}\sum_{\mathbf{d}\in\mathcal{B}_{\mathbf{d}}}\left[\nabla_\mu\widehat{\mathcal{L}}_{\mathrm{o}}\right]_{\widetilde{\mathbf{p}}=\widetilde{\mathbf{p}}^{(q)},\widetilde{\mathbf{b}}=\widetilde{\mathbf{b}}^{(q)}}\right]^+,\end{aligned} \tag{4.24}$$

where $[\chi]^+ = \max\{0,\chi\}$ and ϕ_μ is the learning rate. In (4.24), $\nabla_{\boldsymbol{\mu}}\widehat{\mathcal{L}}_{\mathrm{o}}$ can be derived as

$$\nabla_{\boldsymbol{\mu}}\widehat{\mathcal{L}}_{\mathrm{o}} = \begin{bmatrix}\mathbf{1}_{n_{\mathrm{S}}}^{\mathrm{T}}\widetilde{\mathbf{p}} - p_{\mathrm{tot}} \\ \mathbf{1}_{n_{\mathrm{S}}}^{\mathrm{T}}\widetilde{\mathbf{b}} - \overline{b}_{\mathrm{tot}}\end{bmatrix}. \tag{4.25}$$

Finally, we note that based on (4.18) and (4.24), we can iteratively update $\boldsymbol{\Theta}$ and $\boldsymbol{\mu}$ in the unsupervised learning model.

Table 4.1: Values of parameters used for numerical results in Section 4.4.

Parameter	**Value**
System Parameters	
Heights of the AP and users, h_{A}, h_{U}	3.0 m, 1.3 m
Antenna gains, G_{A}, G_{U}	30 dBi, 20 dBi
Noise power density, N_0	-174 dBm/Hz
Power budget at the AP, p_{tot}	-5 dBm
Upper bound on power per sub-band, $p_{\max}$	$\frac{5}{4}\frac{p_{\mathrm{tot}}}{n_{\mathrm{I}}}$
Upper bound on sub-band bandwidth, $b_{\max}$	5 GHz
Height and radius of blockers, h_{B}, r_{B}	1.7 m, 0.3 m
Density of wall blockers, λ_{B}	0.2 m^{-2}
Hyper-Parameters of the Unsupervised Learning Model	
Learning rates, ϕ_Θ ϕ_μ	0.05, 0.025
Number of iterations	500
Total number of realizations of $\mathbf{d}$, n_{T}	300
Activation function of 1st to 4th layer, $F_{\mathrm{A}}^{(\ell)}(\ \cdot\ )$	ReLU
Activation function of the 5th layer, $F_{\mathrm{A}}^{(\ell)}(\ \cdot\ )$	$\Xi\cdot$ sigmoid, $\Xi \in \{p_{\max}, b_{\max}\}$
Parameters used for the Convex Optimization-based Approach	
Exponential model parameters in $\mathrm{sr}_4^{\mathrm{n}}$, $\sigma_1, \sigma_2, \sigma_3$	$10^{1.83}$,-$10^{-10.04}$,$10^{-1.23}$
Exponential model parameters in $\mathrm{sr}_5^{\mathrm{n}}$, $\sigma_1, \sigma_2, \sigma_3$	$10^{0.89}$,-$10^{-10.8}$,-$10^{-1.53}$
Transformation model parameters, $\xi_s, \omega_s, \varsigma_s$	$10^{9.7}$,$10^{10.7}$,10^{-3}

Remark 4.1 *The training phase of the unsupervised learning-based solution is computationally very intensive. However, since training is carried out offline before the implementation phase where the optimal solution to the problem is approximated for the given distance vector, the high computational complexity of the training phase would not impact the real-time applicability of the proposed unsupervised learning-based approach. The complexity characterization of the training phase of the unsupervised learning-based approach is beyond the scope of this thesis, but will be considered in our future works.*

4.4 Numerical Results

In this section, we present numerical results to illustrate the performance of the proposed spectrum allocation strategy and the proposed unsupervised learning-based approach. We consider the convex optimization-based approach presented in Chapter 2 as the benchmark for demonstrating the effectiveness and benefits of the proposed unsupervised learning-based approach.

The numerical results are obtained by considering a rectangular indoor environment of size 25 m $\times$ 25 m where an AP, which is located at the center of the ceiling of the indoor environment, serves 15 users. We consider the spectrum with a bandwidth of 50 GHz that exists in either (i) the NACSR between 0.556 THz and 0.67 THz or (ii) the NACSR between 0.753 THz and 0.848 THz. We denote the two NACSR as sr_4^{n} and sr_5^{n}, respectively, as depicted in Fig. 4.1. We clarify that on one hand, the molecular absorption coefficient, $k(f)$, in sr_5^{n} can be modeled as an exponential function of frequency with minimal approximation errors. Hence, the resource allocation problem in sr_5^{n} is a special case of the general resource allocation problem considered in this chapter. On the other hand, $k(f)$ in sr_4^{n} cannot be modeled as an exponential function of frequency.

We implement the unsupervised learning model presented in Section 4.3 in Python. We utilize a five-layer DNN for the unsupervised learning model, which has 100, 100, 50, 25, and 30 neurons in the first, second, third, fourth, and fifth layers, respectively. The initial weights of the DNN are Gaussian random variables with zero mean and unit variance, and the initial biases are set to 0. The initial values of $\boldsymbol{\mu}$ are set to a small constant of 0.1. The values of other system parameters, hyper-parameters of the unsupervised learning model, and the parameters of the convex optimization-based approach used for numerical results are summarized in Table 4.1.

In Fig. 4.5, we show the convergence of the proposed unsupervised learning-based approach when $k(f)$ within the to-be-allocated spectrum can be modeled as an exponential function of frequency. To this end, we plot the aggregated multiuser throughput, $r_{\text{AG}} = \mathbf{1}_{n_{\text{S}}}^{\text{T}}\mathbf{r}$, the value of $\mathbf{1}_{n_{\text{S}}}^{\text{T}}\mathbf{p} - p_{\text{tot}}$, and the value of $\mathbf{1}_{n_{\text{S}}}^{\text{T}}\mathbf{b} - \overline{b}_{\text{tot}}$ obtained from the unsupervised learning-based approach in Figs. 4.5(a), 4.5(b), and 4.5(c), respectively, when the resource allocation problem is implemented in

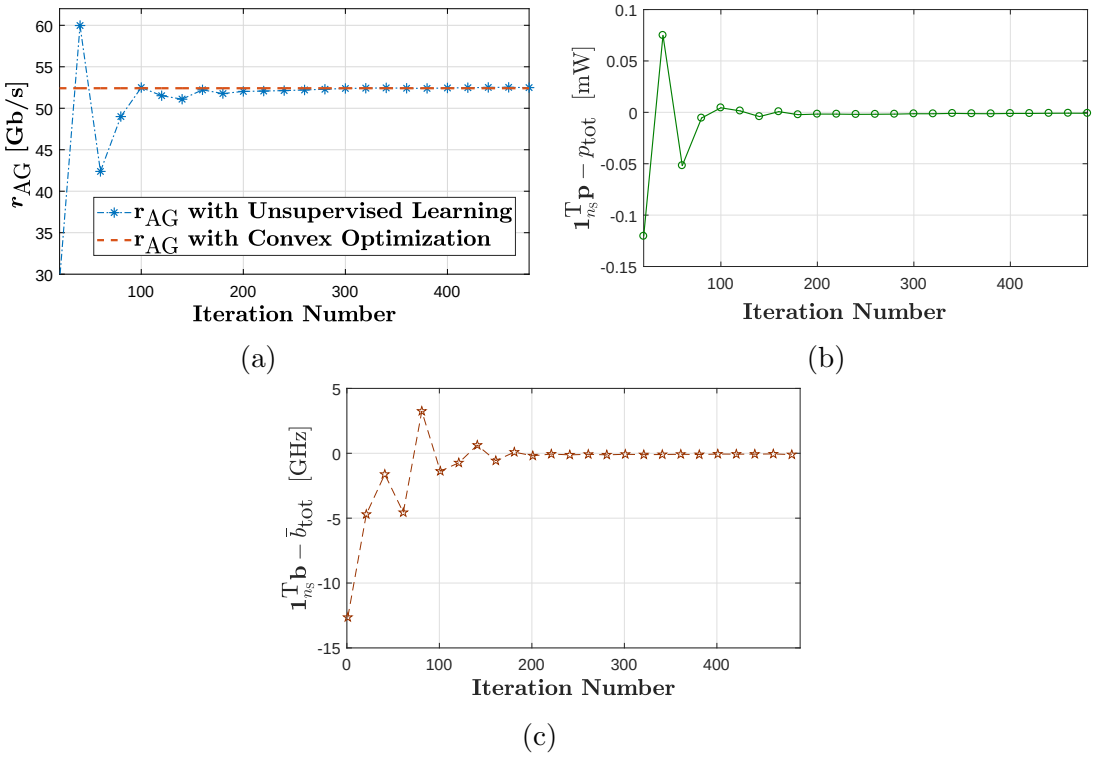

Figure 4.5: The aggregated multiuser throughput, r_{AG}, and total power and bandwidth constraints satisfaction when $k(f)$ within the to-be-allocated spectrum can be modeled as an exponential function of frequency, i.e., in the special case system investigated in Chapter 2.

$\mathrm{sr}_5^{\mathrm{n}}$ while considering $\lambda_{\mathrm{B}} = 0$. Also, the value of r_{AG} obtained using the convex optimization-based approach presented in Chapter 2, is plotted in Fig. 4.5(a). We first observe from Fig. 4.5(a) that for several initial iterations, the value of r_{AG} obtained using the unsupervised learning-based approach is higher than that obtained using the convex optimization-based approach. This is due to the occasional violation of the constraints (4.9b) and (4.9d) that occur at corresponding initial iterations, which can be validated by observing $\mathbf{1}_{n_{\mathrm{S}}}^{\mathrm{T}}\mathbf{p} - p_{\mathrm{tot}}$ and $\mathbf{1}_{n_{\mathrm{S}}}^{\mathrm{T}}\mathbf{b} - \bar{b}_{\mathrm{tot}}$ in Figs. 4.5(b) and 4.5(c), respectively. Moreover, after 200 iterations, we observe that the value of r_{AG} obtained using the unsupervised learning-based approach converges to the optimal value obtained using the convex optimization-based approach, which shows the correctness of the proposed unsupervised learning-based approach. Finally, we observe from Figs. 4.5(b) and 4.5(c) that after 200 iterations,

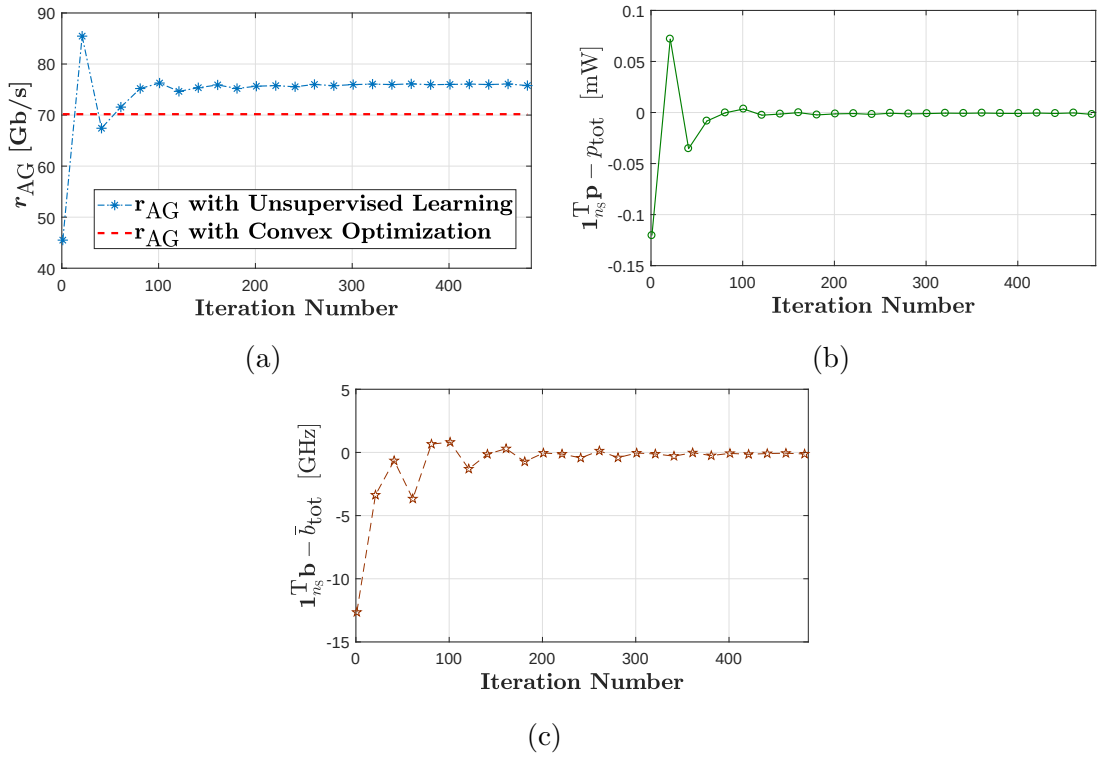

Figure 4.6: The aggregated multiuser throughput and total power and bandwidth constraints satisfaction when $k(f)$ within the to-be-allocated spectrum cannot be modeled as an exponential function of frequency.

the values of $\mathbf{1}_{n_{\mathrm{S}}}^{\mathrm{T}}\mathbf{p}-p_{\mathrm{tot}}$ and $\mathbf{1}_{n_{\mathrm{S}}}^{\mathrm{T}}\mathbf{b}-\bar{b}_{\mathrm{tot}}$ of the proposed unsupervised learning-based approach are very close to zero, which reflects that constraints (4.9b) and (4.9d) are satisfied when the proposed unsupervised learning-based approach is used.

We next show the convergence of the proposed unsupervised learning-based approach when $k(f)$ within the to-be-allocated spectrum cannot be modeled as an exponential function of frequency. To this end, we plot r_{AG}, $\mathbf{1}_{n_{\mathrm{S}}}^{\mathrm{T}}\mathbf{p}-p_{\mathrm{tot}}$, and $\mathbf{1}_{n_{\mathrm{S}}}^{\mathrm{T}}\mathbf{b}-\bar{b}_{\mathrm{tot}}$ in Figs. 4.6(a), 4.6(b), and 4.7(c), respectively, when the resource allocation problem is implemented in $\mathrm{sr}_4^{\mathrm{n}}$ while considering $\lambda_{\mathrm{B}} = 0$. We clarify that in $\mathrm{sr}_4^{\mathrm{n}}$, $k(f)$ cannot be modeled as an exponential function of frequency with minimal approximation errors. However, for the sake of comparison, we obtain approximate solutions to the resource allocation problem in $\mathrm{sr}_4^{\mathrm{n}}$ using the convex optimization approach presented in Chapter 2 while utilizing an inaccurate approximation for $k(f)$ in $\mathrm{sr}_4^{\mathrm{n}}$, and plot the resulting r_{AG} in Fig. 4.6(a). Once again, we observe the

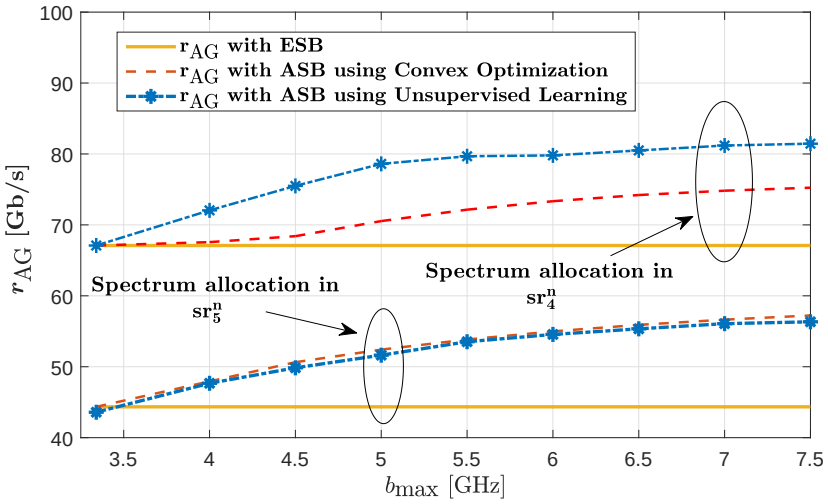

Figure 4.7: The aggregated multiuser throughput versus the upper bound on sub-band bandwidth, $b_{\max}$, when spectrum allocation in $\mathrm{sr}_4^{\mathrm{n}}$ and $\mathrm{sr}_5^{\mathrm{n}}$.

overshoot in r_{AG}, $\mathbf{1}_{n_{\mathrm{S}}}^{\mathrm{T}}\mathbf{p} - p_{\mathrm{tot}}$, and $\mathbf{1}_{n_{\mathrm{S}}}^{\mathrm{T}}\mathbf{b} - \bar{b}_{\mathrm{tot}}$ for several initial iterations and the satisfaction of the constraints (4.9b) and (4.9d) after 200 iterations in Figs. 4.6(a)-4.6(c), which are similar to Figs. 4.5(a)-4.5(c). Apart from them, we further observe that the value of r_{AG} obtained using the unsupervised learning-based approach converges to a value higher than that obtained using the convex optimization-based approach. This is because when the convex optimization-based approach is used, where an exponential function with high approximation errors is used to model $k(f)$, only the sub-optimal r_{AG} is obtained. This shows the significance of the proposed unsupervised learning-based approach, i.e., it gives much higher r_{AG} for the resource allocation problem when $k(f)$ within the to-be-allocated spectrum cannot be modeled as an exponential function of frequency.

We next plot r_{AG} achieved by the spectrum allocation strategy with ESB [32] and the spectrum allocation strategy with ASB that is obtained from both convex optimization and unsupervised learning-based approaches, versus the upper bound on sub-band bandwidth, $b_{\max}$, while considering $\lambda_{\mathrm{B}} = 0$ in Fig. 4.7. We first observe that the proposed spectrum strategy with ASB achieves a significantly higher r_{AG} compared to the strategy with ESB for different $b_{\max}$, which demonstrates the benefits of the proposed strategy with ASB. Second, we observe that

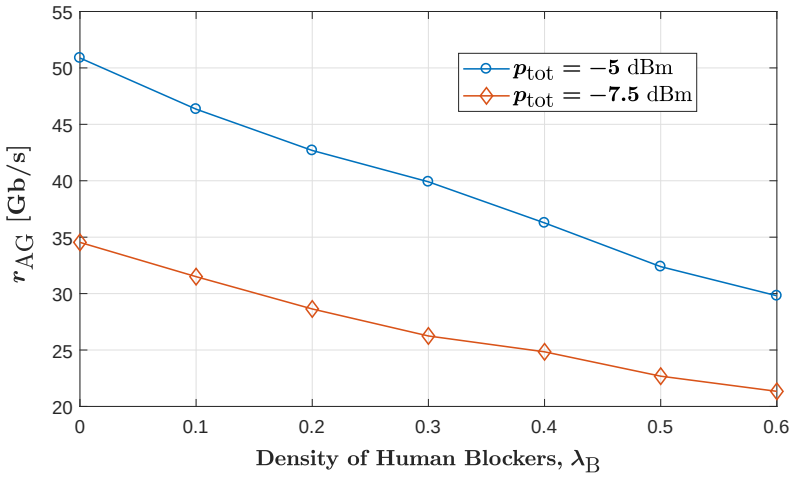

Figure 4.8: The aggregated multiuser throughput versus the density of human blockers, λ_{B}.

in $\mathrm{sr}_4^{\mathrm{n}}$, the value of r_{AG} obtained using the unsupervised learning-based approach converges to values higher than that obtained using the convex optimization-based approach for all $b_{\max}$. This again shows the significance of the proposed unsupervised learning-based approach to obtain higher r_{AG}, especially when $k(f)$ within the to-be-allocated spectrum cannot be modeled as an exponential function of frequency.

We finally examine the impact of human blockers on the proposed spectrum allocation strategy. To this end, Fig. 4.8 plots r_{AG} versus the density of human blockers, λ_{B}. We observe that for different power budget levels, r_{AG} of the spectrum allocation strategy decreases with the increasing λ_{B}. This is due to the decrease in the time during which the AP to user links are available for data transmission when λ_{B} increases. This observation emphasizes the importance of carefully selecting the system parameters, e.g., power budget and maximum sub-band bandwidth, for achieving the desired throughput and reliability performance, depending on the density of human blockers in the indoor environment.

4.5 Summary

We investigated the design challenges of (i) multi-band-based spectrum allocation with ASB for multiuser THzCom systems when the molecular absorption coefficient varies in a highly non-linear manner and (ii) the modeling and analysis of the impact of human blockages on THz band spectrum allocation. We first formulated a resource allocation problem and then proposed an unsupervised learning-based approach to obtaining near-optimal sub-band bandwidth and transmit power. In the proposed unsupervised learning-based approach, we first employed an offline training phase to train a DNN while utilizing a loss function inspired by the Lagrangian of the formulated problem. Then, using the trained DNN, we approximated the near-optimal solutions to the optimization problem for the given distance vector. Numerical results showed that when the values of the molecular absorption coefficient within the spectrum cannot be modeled as an exponential function of frequency, the throughput obtained by the proposed unsupervised learning-based approach outperforms that obtained by the existing approximate approaches. We also showed that the throughput of the spectrum allocation strategy decreases with the increasing density of human blockers. Thus, system parameters, e.g., power budget and maximum sub-band bandwidth, have to be carefully selected for achieving the desired throughput and reliability performance, depending on the density of human blockers in the indoor environment.

Chapter 5

Blockage and Coverage Analysis for 3D THzCom Systems

5.1 Introduction

In this technical chapter, we conduct a novel blockage and reliability analysis of three dimensional (3D) terahertz (THz) band communication (THzCom) system. Specifically, we investigate (i) the modeling and analysis of different types of blockages and (ii) the reliability analysis of downlink transmission in an indoor THzCom system when frequency reuse is considered. Different from existing studies, we characterize the joint impact of blockages caused by the user itself, moving humans, and wall blockers in a 3D THzCom environment. Then, we derive the blockage probabilities associated with a point-to-point THzCom link. Thereafter, considering the 3D directional antennas at both access points (APs) and user equipments (UEs), and the impacts of the blockage, we develop a tractable analytical framework to derive a new expression for the coverage probability by examining the regions where dominant interferers[1] (i.e., those can cause outage by themselves) can exist, and the average number of interferers existing in these regions. Using numerical results, we first verify our analysis. We then demonstrate that network densification deteriorates the reliability of THzCom systems and that it is

[1]The intra-band interference discussed in Chapters 1, 2,, 3, and 4 is commonly referred to as interference in this chapter.

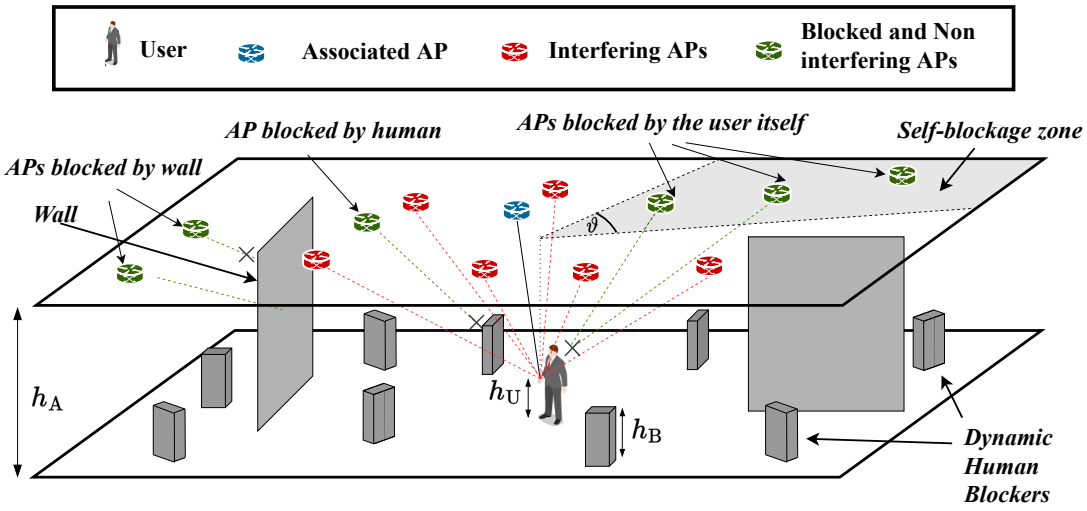

Figure 5.1: Illustration of the 3D THzCom system where a typical user associates with a non-blocked (blue) AP in the presence of interfering (red) APs. The non-interfering APs include those (green) blocked by self-blockage, dynamic human, and wall blockers.

necessary to carefully select the AP densities to obtain the desired reliability performance depending on the communication environment of interest. We also find that an increase in the density of human blockers slightly improves the coverage probability when the transmission link of interest is in line-of-sight (LoS), but reduces the overall coverage probability. Finally, we show that the vertical heights of the THz devices profoundly impact the coverage probability in THzCom systems; therefore, ignoring their impacts leads to a substantial underestimation of system reliability.

The rest of the chapter is organized as follows. In Section 5.2, we describe the system model. In Section 5.3, we evaluate the impact of blockages and 3D directional antennas. In Section 5.4, we present the analytical framework that is used to derive the coverage probability when frequency reuse is considered. In Section 5.5, numerical and simulation results are provided. Finally, in Section 5.6 we conclude the chapter.

Table 5.1: Summary of the main system parameters used in Chapter 5.

	Symbol	Description
System Parameters	***Network Model Parameters***	
	h_{A}, h_{U}	Heights of APs and UEs
	λ_{A}	Density of APs
	l_{ij}, $d(l_{ij})$	2D and 3D distances of AP_i to UE_j link
	Blockage Model Parameters	
	ϑ	Self-blockage angle
	h_{B}	Height of human blockers
	$L_{\mathrm{B},1}$, $L_{\mathrm{B},2}$	Widths of human blockers
	v_{B}	Speed of human blockers
	L_{W}	Length of wall blockers
	λ_{B}, λ_{W}	Densities of human and wall blockers
	Antenna Model Parameters ($\Psi \in \{\mathrm{A}, \mathrm{U}\}$)	
	G_{Ψ}^{m}, G_{Ψ}^{s}	Antenna gains of the main lobe and side lobes
	$\varphi_{\Psi,\mathrm{H}}$, $\varphi_{\Psi,\mathrm{V}}$	Horizontal and vertical beamwidths of the antenna
	$\Omega_{\Psi}^{\mathrm{m}}$, $\Omega_{\Psi}^{\mathrm{s}}$	Solid angles of the main lobe and the side lobes
	Propagation Model Parameters	
	p^{t}	Transmit power
	$p_{\kappa,\iota}^{\mathrm{r}}(l_{ij})$	Received power at UE_j from AP_i
	N_0	Noise power density
	b	Bandwidth of the spectrum of interest
	f	Operating frequency
	$k(f)$	Molecular absorption coefficient
	Υ_{thr}	SINR threshold

*A is for AP, U is for UE, B is for human blocker, W is for wall blocker, H is for horizontal, V is for vertical, m is for main lobe, and s is for side lobes.

5.2 System Model

Fig. 5.1 depicts the 3D THzCom system considered in this chapter. We focus on the downlink signal propagation of a typical user who is at the center of a typical indoor environment. The summary of the main system parameters used in this chapter is given in Table 5.1.

5.2.1 Network Deployment

We consider that the THz APs are mounted on the ceiling. Hence, we model them as having fixed height h_{A} and their locations follow a Poisson point process (PPP) in $\mathbb{R}^2$ with the density of λ_{A}. We also assume that UEs, all of which are of fixed height h_{U}, are distributed uniformly within the circle with the radius L_{T} centered at each AP. Although multiple UEs may exist in each circle, we assume that each AP in the system associates with a single UE, and the link between the AP and its associated UE is not blocked by wall blockers.

For the purpose of analysis, we select a UE-AP pair, among the multiple UE-AP pairs, such that the UE in that pair is located at the center of the indoor environment [84]. We denote the UE and the AP in that pair by UE_0 and AP_0, respectively. Also, we assume that all the UE-AP pairs share the same frequency channel[2]; hence, apart from AP_0, all the other APs in the indoor environment of interest act as "interferers" to UE_0. We denote these interfering APs by AP_i, where $i = 1, 2, \ldots$, and the UEs that associate with these APs by UE_j, where $j = 1, 2, \ldots$, with $i = j$ for UE and the AP in a specific UE-AP pair. Moreover, we denote l_{ij} and $d(l_{ij}) = \sqrt{h_{\epsilon}^2 + l_{ij}^2}$ as the horizontal and 3D distances between AP_i and UE_j, respectively, with $h_{\epsilon} = h_{\mathrm{A}} - h_{\mathrm{U}}$.

5.2.2 Blockage Model

In our system, we consider that the blockage of a UE-AP link can be caused by (i) the user itself, referred to as self-blockage, and/or (ii) the dynamic human blockers, and/or (iii) static wall blockers.

5.2.2.1 Self-blockage

Self-blockage plays a significant role in determining THz system performance. Notably, self-blockage may lead to the fact that signals from some APs surrounding a UE are totally blocked, even if the APs are within close proximity. We define the zone which is blocked by the UEs themselves as "self-blockage zone" [71, 77], as shown in Fig. 5.1 with a self-blockage angle of ϑ.

[2]We note that the frequency channel would be a single sub-band if multi-band-based spectrum allocation is considered.

5.2.2.2 Dynamic Human Blockers

Humans moving in the area of the considered system can act as blockers. Specifically, they can potentially block the desired signals from AP_0 to UE_0, as well as the interference signals from other APs to UE_0. Similar to that in Chapter 4, we model the human blockers by rectangular absorbing screens (commonly referred to as the double knife-edge (DKE) model) with heights h_{B} and widths $L_{\mathrm{B},1}$ and $L_{\mathrm{B},2}$ [124]. Furthermore, we assume that the locations of humans form a PPP with the density of λ_{B} and their mobility follows the random directional (RD) model [125]. Based on the RD model, a moving human randomly selects a direction in $(0, 2\pi)$ to travel in and a duration for this travel. At the end of this duration, another independent direction to travel in and a time duration for this travel are selected, and the pattern continues. Following [71, 82, 126, 127], we assume that the moving speeds of all human blockers are v_{B}.

5.2.2.3 Wall Blockers

We employ a tractable Boolean scheme of straight lines to generate wall blockers in the indoor environment [128,129]. We assume that the lengths of walls, L_{W}, follow an arbitrary probability density function (PDF) of $\Gamma_{L_{\mathrm{W}}}(L_{\mathrm{W}})$ with mean $\mathbb{E}[L_{\mathrm{W}}]$, and the centers of walls form a PPP of density λ_{W}. We ignore the widths of walls as the widths are much smaller compared to the lengths of walls.[3]. Moreover, we assume that the orientations of walls are binary choices of either 0 or $\pi/2$ with equal probability to ensure that walls are parallel or orthogonal to each other. Furthermore, we assume that the heights of walls are fixed and are same as those of the APs, i.e., $h_{\mathrm{W}} = h_{\mathrm{A}}$.

5.2.3 Antenna Model

In this chapter, we assume that 3D beams are utilized at the APs and the UEs. The 3D antenna beams are approximated by a 3D pyramidal-plus-sphere sectored

[3]The penetration losses of THz signals over wood, brick, plastic and glass materials are expected to be significantly higher due to the very small wavelength of THz signals [33, 35] Thus, the proposed analysis can be extended even if glass or/and plywood walls are considered in the system model despite the fact that our analysis in this chapter primarily considers brick walls.

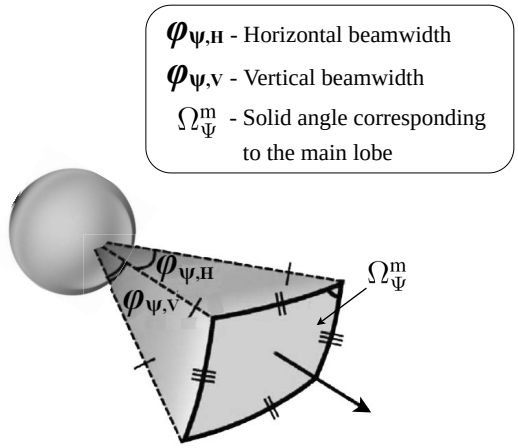

Figure 5.2: 3D sectored antenna radiation model.

antenna model, as shown in Fig. 5.2 [72, 130]. In this model, the pyramidal zone accounts for the main lobe of the antenna beam, and the sphere accounts for the side lobes of the antenna beam.[4] We also consider that the main lobe of APs and their associated UEs are tilted downwards and upwards, respectively, towards each other as shown in Fig. 5.3. This guarantees beam alignment between APs and their associated UEs.

Based on the principles of antenna theory, the antenna gains of the main lobe and the side lobes are expressed as

$$G_{\Psi}^{\mathrm{m}} = \frac{p_{\Psi,\mathrm{m}}^{\mathrm{rad}}/\Omega_{\Psi}^{\mathrm{m}}}{p_{\Psi}^{\mathrm{rad}}/4\pi} \tag{5.1}$$

and

$$G_{\Psi}^{\mathrm{s}} = \frac{p_{\Psi,\mathrm{s}}^{\mathrm{rad}}/\Omega_{\Psi}^{\mathrm{s}}}{p_{\Psi}^{\mathrm{rad}}/4\pi}, \tag{5.2}$$

respectively, where $\Psi \in \{\mathrm{A}, \mathrm{U}\}$ with A is for AP and U is for UE, $p_{\Psi,\mathrm{m}}^{\mathrm{rad}}$ and $p_{\Psi,\mathrm{s}}^{\mathrm{rad}}$

[4]We clarify that sectored antenna models are widely used in the previous studies at the mmWave and THz bands for tractable analysis [72–75,77,83,86,87,89,130,131]. More importantly, the considered 3D sectored antenna model closely resembles the antenna radiation patterns that are observed in typical THz band horn antennas and graphene-based antennas [33, 34]. However, the consideration of complex 3D antenna models such as the 3D sync model [132] or the 3D multi-cone model [133] can further improve the accuracy of the results; thus will be considered in our future works.

are the power concentrated along the main lobe and side lobes, respectively, with $p_{\Psi}^{\mathrm{rad}} = p_{\Psi,\mathrm{m}}^{\mathrm{rad}} + p_{\Psi,\mathrm{s}}^{\mathrm{rad}}$, and $\Omega_{\Psi}^{\mathrm{m}}$ and $\Omega_{\Psi}^{\mathrm{s}}$ are the solid angles corresponding to the main lobe and the side lobes, respectively.

Using the "standard formula of rectangular plane" given by the HCR's Theory of Polygon [134], $\Omega_{\Psi}^{\mathrm{m}}$ in (5.1) can be expressed as

$$\Omega_{\Psi}^{\mathrm{m}} = 4 \arcsin\left(\tan\left(\frac{\varphi_{\Psi,\mathrm{H}}}{2}\right)\tan\left(\frac{\varphi_{\Psi,\mathrm{V}}}{2}\right)\right) \tag{5.3}$$

where $\varphi_{\Psi,\mathrm{H}}$ and $\varphi_{\Psi,\mathrm{V}}$ are the horizontal and vertical beamwidths of the antenna, respectively. In addition, following the fact that the solid angle of the sphere is 4π, we obtain $\Omega_{\Psi}^{\mathrm{s}}$ in (5.2) as $\Omega_{\Psi}^{\mathrm{s}} = 4\pi - \Omega_{\Psi}^{\mathrm{m}}$. Finally, we obtain the antenna gains of the main lobe and the side lobes in (5.1) and (5.2) as

$$G_{\Psi}^{\mathrm{m}} = \frac{4\pi}{\left(\left(p_{\Psi,\mathrm{s}}^{\mathrm{rad}}/p_{\Psi,\mathrm{m}}^{\mathrm{rad}}\right)+1\right)\Omega_{\Psi}^{\mathrm{m}}} \tag{5.4}$$

and

$$G_{\Psi}^{\mathrm{s}} = \frac{4\pi}{\left(1+\left(p_{\Psi,\mathrm{m}}^{\mathrm{rad}}/p_{\Psi,\mathrm{s}}^{\mathrm{rad}}\right)\right)\left(4\pi-\Omega_{\Psi}^{\mathrm{m}}\right)}, \tag{5.5}$$

respectively.

5.2.4 Propagation Model

The signal propagation at the THz band is determined by spreading loss and molecular absorption loss [29]. Therefore, the received power at UE_j from AP_i in the 3D channel is

$$p_{\kappa,\iota}^{\mathrm{r}}(l_{ij}) = \widehat{\varrho}_{\kappa,\iota}\left(d(l_{ij})\right)^{-2} e^{-k(f)d(l_{ij})}, \tag{5.6}$$

where $\widehat{\varrho}_{\kappa,\iota} \triangleq p^{\mathrm{t}} G_{\mathrm{A}}^{\kappa} G_{\mathrm{U}}^{\iota} \left(c/4\pi f\right)^2$, p^{t} is the transmit power, G_{A}^{κ} and G_{U}^{ι} are the effective antenna gains at AP_i and UE_j, respectively, corresponding to link between AP_i and UE_j with $\kappa \in \{\mathrm{m,s}\}$ and $\iota \in \{\mathrm{m,s}\}$ where m is for main lobe and s is for side lobes, c is the speed of light, f is the operating frequency, and $k(f)$ is the molecular absorption coefficient of the transmission medium. Following [72, 73, 87–89], we consider the received power while considering that the molecular absorption

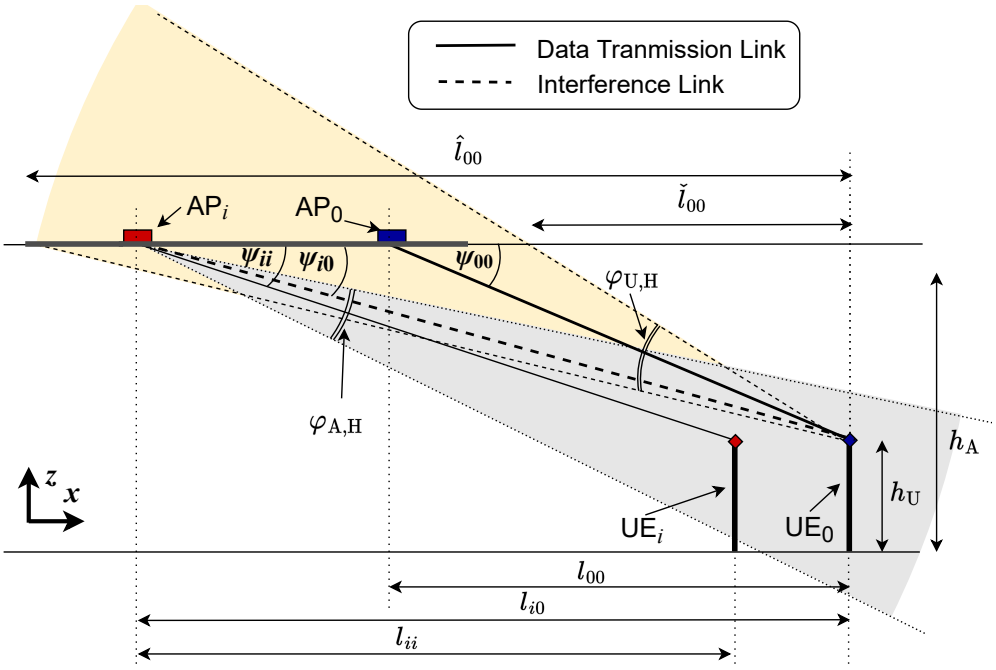

Figure 5.3: Illustration of the side view of the UE_0-AP_0 link.

coefficient remains unchanged within the bandwidth of interest, which is similar to that considered in Chapters 2 and 3. Moreover, it is noted that similar to that in Chapters 2, 3, and 4, in this chapter, we (i) ignore the impact of non-line-of-sight (nLoS) rays and focus only on the LoS rays of THz signals [62, 69, 72, 73, 75, 86–88], (ii) omit the impact of fading in the THz channel [62, 69, 72–75, 86–88, 113], and (iii) consider inter-band interference (Inter-BI) free transmission [50, 114]. The justifications behind these considerations are given in Section 2.2.4.

5.3 Impacts of Blockages and 3D Directional Antennas

In this section, we analyze the impact of blockages and 3D directional antennas. The summary of the main quantities of interest used in this chapter is given in Table 5.2.

Table 5.2: Summary of the main quantities of interest used in Chapter 5.

	Symbol	Description
Quantities of Interest	$\rho^{\mathrm{LoS}}(l_{ij})$	LoS probability
	$\rho_{\mathrm{B}}^{\mathrm{LoS}}(l_{ij})$	LoS probability in the presence of only human blockers
	$\rho_{\mathrm{W}}^{\mathrm{LoS}}(l_{ij})$	LoS probability in the presence of only wall blockers
	$\Gamma_l(l_{ii})$	PDF of the horizontal distance between AP_i and UE_i in the presence of wall blockers
	$\rho^{\mathrm{hp}}(l_{i0})$	Hitting probability
	$\rho_{\mathrm{H}}^{\mathrm{hp}}(l_{i0})$	Horizontal hitting probability
	$\rho_{\mathrm{V}}^{\mathrm{hp}}(l_{i0})$	Vertical hitting probability
	$D_{\kappa,\iota}$	Distance from UE_0 to the boundary of the region around UE_0 where *dominant interferers* can exist
	$\Lambda_{\Phi^{\mathrm{N}}}$, $\Lambda_{\Phi^{\mathrm{F}}}$	Average number of *near* and *far dominant interferers* that exist around UE_0
	$\rho^{\mathrm{c}}(l_{00})$	Coverage probability at UE_0
	$\rho^{\mathrm{c,LoS}}(l_{00})$	Coverage probability at UE_0 when the link between UE_0 and AP_0 is in LoS

*A is for AP, U is for UE, B is for human blocker, W is for wall blocker, H is for horizontal, V is for vertical, m is for main lobe, and s is for side lobes.

5.3.1 Impact of Blockages

We first analyze the LoS probabilities due to each type of blockage acting alone, and present the results in the following lemmas.

Lemma 5.1 *The LoS probability for the link between AP_i and UE_j in the presence of only dynamic human blockers is*

$$\rho_B^{LoS}(l_{ij}) = \zeta e^{-\widetilde{\lambda}_B l_{ij}}, \tag{5.7}$$

where $\zeta = e^{-2L_{B,1}L_{B,2}\lambda_B}$ *and* $\widetilde{\lambda}_B = \frac{2(L_{B,1}+L_{B,2})\lambda_B(h_B-h_U)}{\pi h_\epsilon}$.

Proof: The proof is similar to that of Lemma 4.1 and thus omitted. ■

Lemma 5.2 *The LoS probability for the link between AP_i and UE_j in the presence of only wall blockers is*

$$\rho_W^{LoS}(l_{ij}) = e^{-\widetilde{\lambda}_{W,1} l_{ij}}, \tag{5.8}$$

where $\widetilde{\lambda}_{W,1} = \lambda_W \frac{2}{\pi}\mathbb{E}[L_W]$.

Proof: See Appendix C.1. ■

We clarify that in this chapter, we assume that each AP in the system selects its associating UE such that the link between the AP and its associated UE is not blocked by wall blockers. Thus, $\rho_{\mathrm{W}}^{\mathrm{LoS}}(l_{ii}) = 1, \forall i$.

We next jointly consider Lemma 5.1 and Lemma 5.2 to obtain the following corollary.

Corollary 5.1 *The LoS probability for the link between AP_i and UE_j in the presence of both human and wall blockers is*

$$\rho^{LoS}(l_{ij}) = \rho_B^{LoS}(l_{ij})\rho_W^{LoS}(l_{ij}) = \zeta e^{-\widetilde{\lambda} l_{ij}}, \tag{5.9}$$

where $\widetilde{\lambda} = \widetilde{\lambda}_B + \widetilde{\lambda}_{W,1}$.

We clarify that Corollary 5.1 is obtained by considering that the locations of humans and wall blockers are independent of each other and this consideration has been widely adopted in previous relevant studies in the literature for tractable analysis.[5] [71, 123, 126]

5.3.2 Impact of 3D Directional Antennas

To investigate the impact of an interfering AP on the aggregated interference at UE_0, it is essential to characterize whether the signal corresponding to the main lobe of the interfering AP reaches UE_0. To this end, we determine the *hitting probability*, $\rho^{\mathrm{hp}}(l_{i0})$, which is defined as the probability of the signal corresponding to the main lobe of an interfering AP, i.e., AP_i, reaching UE_0, where $i \neq 0$.

The previous studies that analyzed the coverage probability of THzCom systems approximated the antenna radiation pattern of THz transceivers using 2D antenna models [72–75, 86–88, 113]. In such studies, it was assumed that the main lobe of APs and their associated UEs are pointed toward each other in the horizontal direction. Under such consideration, the signal corresponding to the main

[5] In a realistic indoor environment, humans may keep a certain distance from walls. Thus, the consideration of dependency between the locations of humans and walls can improve the accuracy of the results and will be addressed in our future work.

lobe of the interfering AP reaches UE_0, as long as UE_0 is within the horizontal beamwidths of the interfering AP, regardless of whether UE_0 is in close proximity to the interfering AP or not. Therefore, when a 2D antenna model is adopted, the hitting probability is obtained as [87]

$$\rho^{\mathrm{hp}}(l_{i0})|_{\mathrm{2D}} = \frac{\varphi_{\mathrm{A,H}} l_{ij}}{2\pi l_{ij}} = \frac{\varphi_{\mathrm{A,H}}}{2\pi}. \tag{5.10}$$

In contrast to the previous studies, in this chapter, we assume that a 3D antenna model is utilized to approximate the antenna radiation patterns of transceivers. Therefore, we consider that the main lobe of APs and their associated UEs are tilted downwards and upwards, respectively, towards each other as shown in Fig. 5.3. This guarantees beam alignment between APs and their associated UEs. Under such consideration, the signal corresponding to the main lobe of an interfering AP reaches UE_0 only when UE_0 is within both the horizontal and vertical beamwidths of the interfering AP. Therefore, when the 3D sectored antenna model is adopted, $\rho^{\mathrm{hp}}(l_{i0})$ is expressed as

$$\rho^{\mathrm{hp}}(l_{i0}) = \rho^{\mathrm{hp}}_{\mathrm{H}}(l_{i0})\rho^{\mathrm{hp}}_{\mathrm{V}}(l_{i0}), \tag{5.11}$$

where $\rho^{\mathrm{hp}}_{\mathrm{H}}(l_{i0})$ and $\rho^{\mathrm{hp}}_{\mathrm{V}}(l_{i0})$ are the horizontal and vertical hitting probabilities, respectively. The expressions for $\rho^{\mathrm{hp}}_{\mathrm{H}}(l_{i0})$ and $\rho^{\mathrm{hp}}_{\mathrm{V}}(l_{i0})$ can be determined by evaluating the probabilities of UE_0 being within the horizontal and vertical beamwidths of AP_i, respectively [130]. Therefore, $\rho^{\mathrm{hp}}_{\mathrm{H}}(l_{i0})$ is given by

$$\rho^{\mathrm{hp}}_{\mathrm{H}}(l_{i0}) = \rho^{\mathrm{hp}}(l_{i0})|_{\mathrm{2D}} = \frac{\varphi_{\mathrm{A,H}}}{2\pi}. \tag{5.12}$$

We next derive $\rho^{\mathrm{hp}}_{\mathrm{V}}(l_{i0})$ in the following subsection.

5.3.2.1 Vertical Hitting Probability

The $\rho^{\mathrm{hp}}_{\mathrm{V}}(l_{i0})$ can be determined by evaluating the probabilities of UE_0 being within vertical beamwidths of AP_i. To determine this probability, it is essential to characterize the horizontal distance between AP_i and UE_i probabilistically. Thus, we determine the PDF of the horizontal distance between AP_i and UE_i in the following lemma.

Lemma 5.3 *The PDF of the horizontal distance between AP_i and UE_i in the presence of wall blockers is*

$$\Gamma_l(l_{ii}) = \begin{cases} \widetilde{\lambda}_{W,2} l_{ii} e^{-\widetilde{\lambda}_{W,1} l_{ii}}, & 0 \le l_{ii} \le L_T, \\ 0, & \textit{otherwise}, \end{cases} \tag{5.13}$$

where $\widetilde{\lambda}_{W,2} = \widetilde{\lambda}_{W,1}^2 / \left(1 - e^{-\widetilde{\lambda}_{W,1} L_T}\left(1 + \widetilde{\lambda}_{W,1} L_T\right)\right)$ *and*

$$L_T = \sqrt{\left(\frac{2}{k(f)} W\left[\frac{k(f)}{2}\sqrt{\frac{\widehat{\varrho}_{m,m}}{N_0 b\ \Upsilon_{\text{thr}}}}\right]\right)^2 - h_\epsilon^2}. \tag{5.14}$$

Here, N_0 is the noise power density and b is the bandwidth of the spectrum of interest, Υ_{thr} is the predefined signal-to-interference-plus-noise ratio (SINR) threshold, and $W[\cdot]$ is the Lambert W*-function.*

Proof: See Appendix C.2. ■

Using Lemma 5.3, we next derive $\rho_{\text{V}}^{\text{hp}}(l_{i0})$ in the following proposition.

Proposition 5.1 *The vertical hitting probability for the link between AP_i and UE_0 of the THzCom system is given by*

$$\rho_V^{hp}(l_{i0}) = \begin{cases} \frac{\widetilde{\lambda}_{W,2}}{\widetilde{\lambda}_{W,1}^2}\Big[e^{-\widetilde{\lambda}_{W,1} h_\epsilon \cot\left(\psi_{i0} + \frac{\varphi_{A,V}}{2}\right)}\left(1 + \widetilde{\lambda}_{W,1} h_\epsilon \cot\left(\psi_{i0} + \frac{\varphi_{A,V}}{2}\right)\right) \\ \qquad - e^{-\widetilde{\lambda}_{W,1} h_\epsilon \cot\left(\psi_{i0} - \frac{\varphi_{A,V}}{2}\right)}\left(1 + \widetilde{\lambda}_{W,1} h_\epsilon \cot\left(\psi_{i0} - \frac{\varphi_{A,V}}{2}\right)\right)\Big], & 0 \le l_{i0} \le l_\mu, \\ \frac{\widetilde{\lambda}_{W,2}}{\widetilde{\lambda}_{W,1}^2}\Big[e^{-\widetilde{\lambda}_{W,1} h_\epsilon \cot\left(\psi_{i0} + \frac{\varphi_{A,V}}{2}\right)}\left(1 + \widetilde{\lambda}_{W,1} h_\epsilon \cot\left(\psi_{i0} + \frac{\varphi_{A,V}}{2}\right)\right) \\ \qquad - e^{-\widetilde{\lambda}_{W,1} L_T}\left(1 + \widetilde{\lambda}_{W,1} L_T\right)\Big], & l_\mu < l_{i0} < l_\nu, \\ 0, & l_{i0} \ge l_\nu, \end{cases} \tag{5.15}$$

where $\psi_{i0} = \arctan\left(h_\epsilon / l_{i0}\right)$, $l_\mu = h_\epsilon \cot\left(min\left\{\frac{\pi}{2}, \overline{\psi} + \frac{\varphi_{A,V}}{2}\right\}\right)$, $\overline{\psi} = \arctan\left(h_\epsilon / L_T\right)$, *and* $l_\nu = h_\epsilon \cot\left(max\left\{0, \overline{\psi} - \frac{\varphi_{A,V}}{2}\right\}\right)$.

Proof: See Appendix C.3. ■

Remark 5.1 *Prior studies that analyzed the coverage probability of THzCom systems adopted a 2D model and ignored the impact of* $\rho_V^{hp}(l_{i0})$ *by assuming it to be* $\rho_V^{hp}(l_{i0}) = 1$ *[72–75, 86–88, 113]. However, by examining* (5.15)*, we observe that* $\rho_V^{hp}(l_{i0})$ *increases when* l_{i0} *increases up to* l_μ*, and thereafter starts to decrease. Furthermore,* $\rho_V^{hp}(l_{i0}) \leq 1$*,* $\forall l_{i0}$*. These insights reveal that ignoring the impact of* $\rho_V^{hp}(l_{i0})$ *in THzCom systems would lead to an overestimation of the hitting probability. This in turn overestimates the interference, thereby leading to an underestimation of the coverage probability if a 2D model is adopted for analysis. This will be illustrated through numerical results in Section 5.5.1.*

Based on the derived results in this section, we next derive the coverage probability at UE_0 in the following section.

5.4 Coverage Analysis

The coverage probability at UE_0, $\rho^{\mathrm{c}}(l_{00})$, is the probability that the SINR at UE_0 is larger than the predefined threshold Υ_{thr}, i.e., $\rho^{\mathrm{c}}(l_{00}) = \Pr[\mathrm{SINR} \geq \Upsilon_{\mathrm{thr}}]$. In the considered THzCom environment where blockages exist, $\rho^{\mathrm{c}}(l_{00})$ can be written as

$$\rho^{\mathrm{c}}(l_{00}) = \rho_{\mathrm{B}}^{\mathrm{LoS}}(l_{00})\rho^{\mathrm{c,LoS}}(l_{00}), \tag{5.14}$$

where $\rho_{\mathrm{B}}^{\mathrm{LoS}}(l_{00})$ is the LoS probability calculated in Lemma 5.1 and $\rho^{\mathrm{c,LoS}}(l_{00})$ is the probability of the SINR at UE_0 is larger than Υ_{thr} when the link between UE_0 and AP_0 is in LoS.

Conventionally, the coverage probability of communication systems has been derived with the aid of Laplace transform-based analysis when 2D antenna models are utilized to approximate the antenna radiation patterns of transceivers [83–85, 87]. In such studies, the coverage probability is obtained based on the moment generating function of the aggregate interference, $\mathcal{M}_{I^T_{\mathrm{agg}}|l_{00}}(s)$. However, in this chapter we model the THzCom system in a 3D environment, thus a 3D antenna model is adopted to approximate the antenna radiation patterns of transceivers. Under this consideration, it is challenging to obtain a tractable expression for $\mathcal{M}_{I^T_{\mathrm{agg}}|l_{00}}(s)$ [87]. Specifically, the non-linear expression for the vertical hitting probability derived in

Proposition 5.1 and the LoS probability derived in Corollary 5.1 have to be considered when determining $\mathcal{M}_{I^T_{\text{agg}}|l_{00}}(s)$, thereby making the expression for $\mathcal{M}_{I^T_{\text{agg}}|l_{00}}(s)$ intractable. Hence, we need to resort to approximation methods to analyze the coverage probability of 3D THzCom systems.

In this chapter, we use the dominant interferer analysis to derive the coverage probability [131]. In doing so, we partition the APs which contribute to the aggregated interference at UE_0 into two subsets: *dominant* and *non-dominant interferers*. We define an interferer as a *dominant interferer* if it causes outage at UE_0 when none of the other interferers contribute to the aggregated interference. Moreover, we define an interferer as a *non-dominant interferer* if it cannot cause outage by itself. Dominant interferer analysis assumes that the presence of any combination of *non-dominant interferers* cannot lead to the outage.[6] This assumption allows the coverage probability of THzCom systems to be calculated analytically.

By using the dominant interferer analysis, $\rho^{c,\text{LoS}}(l_{00})$ can be interpreted as the probability that no interferer is a *dominant interferer*, when the link between UE_0 and AP_0 is LoS. Mathematically, $\rho^{c,\text{LoS}}(l_{00})$ is written as $\rho^{c,\text{LoS}}(l_{00}) = \Pr[n(\Phi) = 0]$, where Φ is the sets that denotes the *dominant interferers* that exist around UE_0. In calculating $\Pr[n(\Phi) = 0]$, for analytical simplicity, we further categorize the *dominant interferers* into *near* and *far dominant interferers*.

We define an interferer as a *near dominant interferer* if it can cause outage by itself while having its main lobe or the side lobes facing UE_0. Differently, we define an interferer as a *far dominant interferer* if it causes outage by itself, only when its main lobe is facing UE_0. Therefore, $\rho^{c,\text{LoS}}(l_{00})$ can be re-interpreted as the probability that no interferer is a *near* or a *far dominant interferer*, when the link between UE_0 and AP_0 is LoS. Mathematically, it is written as

$$\rho^{c,\text{LoS}}(l_{00}) = \Pr[n(\Phi) = 0]$$

[6]It is reasonable to assume that any combination of *non-dominant interferers* cannot lead to the outage in THzCom systems, since the aggregated interference from distant interferers is minimal in such systems due to the following reasons. First, the interference power from a distant interferer is very small due to the exponential power decay as a result of the molecular absorption loss. Second, the probability of distant interferers causing interference at UE_0 is very low, due to the use of 3D directional antennas at the UEs and the APs and the fact that the LoS blockage exponentially increases with distance. We will validate the feasibility of this assumption in Section 5.5.2.

$$= \Pr\left[n(\Phi^{\mathrm{N}}) = 0\right] \Pr\left[n(\Phi^{\mathrm{F}}) = 0\right], \tag{5.15}$$

where Φ^{N} and Φ^{F} are the sets that denote the *near* and *far dominant interferers* that exist around UE_0, respectively. To find out the expression for $\Pr\left[n(\Phi^{\mathrm{N}}) = 0\right]$, we denote $\Lambda_{\Phi^{\mathrm{N}}}$ as the average number of *near dominant interferers* that exist around UE_0. Therefore, considering the null probability of $\Lambda_{\Phi^{\mathrm{N}}}$, we obtain

$$\Pr\left[n(\Phi^{\mathrm{N}}) = 0\right] = e^{-\Lambda_{\Phi^{\mathrm{N}}}}. \tag{5.16}$$

Similarly, we denote $\Lambda_{\Phi^{\mathrm{F}}}$ as the average number of *far dominant interferers* that exist around UE_0. Considering the null probability of $\Lambda_{\Phi^{\mathrm{F}}}$, we obtain

$$\Pr\left[n(\Phi^{\mathrm{F}}) = 0\right] = e^{-\Lambda_{\Phi^{\mathrm{F}}}}. \tag{5.17}$$

Thereafter, we substitute (5.16) and (5.17) into (5.15) to obtain

$$\rho^{\mathrm{c,LoS}}(l_{00}) = e^{-\Lambda_{\Phi^{\mathrm{N}}} - \Lambda_{\Phi^{\mathrm{F}}}}. \tag{5.18}$$

Finally, by substituting (5.7) and (5.18) into (5.16), we obtain the coverage probability at UE_0 for the considered THzCom system, and that is presented in the following theorem.

Theorem 5.1 *The coverage probability at UE_0 for the THzCom system is*

$$\rho^{c}(l_{00}) = \zeta e^{-\widetilde{\lambda}_B l_{00} - \Lambda_{\Phi^N} - \Lambda_{\Phi^F}}, \tag{5.19}$$

where $\zeta = e^{-2\lambda_B r_B^2}$, $\widetilde{\lambda}_B = 2\lambda_B r_B(h_B - h_U)/h_\epsilon$, and Λ_{Φ^N} and Λ_{Φ^F} are the average number of near and far dominant interferers that exist around UE_0, respectively.

In Fig. 5.4, we illustrate how the main results in this chapter are jointly utilized to obtain Theorem 5.1. We next present the steps followed in obtaining the expression for $\Lambda_{\Phi^{\mathrm{N}}}$ and $\Lambda_{\Phi^{\mathrm{F}}}$ in the following subsection.

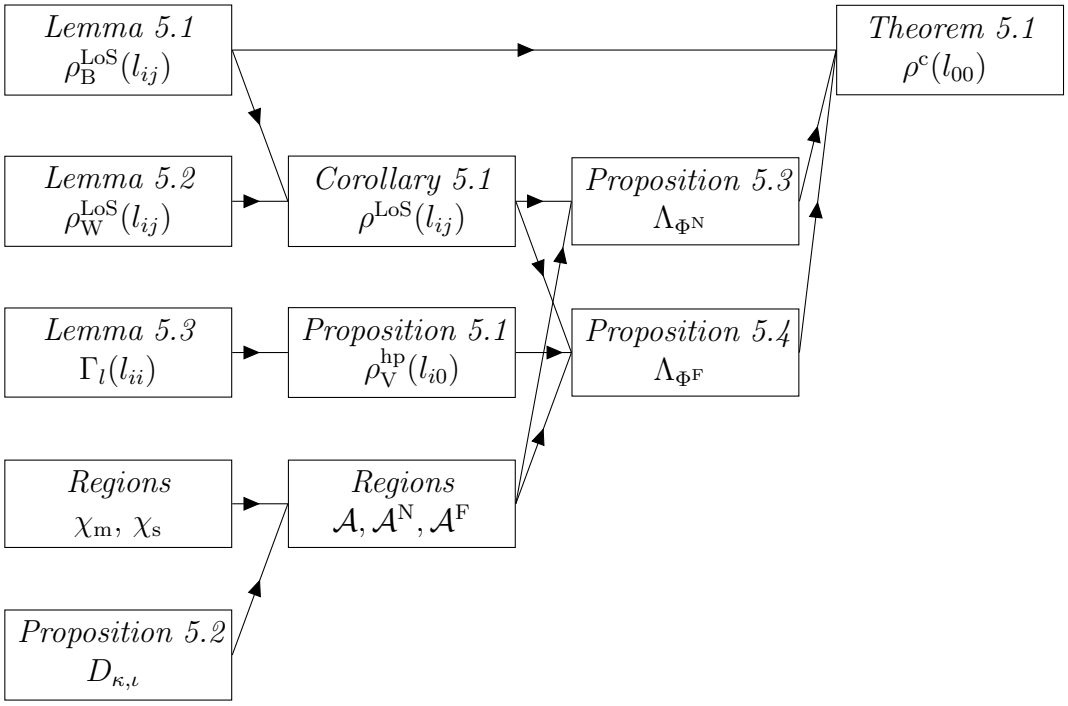

Figure 5.4: Summary of the analytical framework metrics used in this chapter to determine the coverage probability.

5.4.1 Derivation of $\Lambda_{\Phi^{\mathrm{N}}}$ and $\Lambda_{\Phi^{\mathrm{F}}}$

As shown in Fig. 5.4, to determine $\Lambda_{\Phi^{\mathrm{N}}}$ and $\Lambda_{\Phi^{\mathrm{F}}}$, it is essential to obtain $\mathcal{A}$, where $\mathcal{A}$ is the region around UE_0 where *dominant interferers* can exist. To obtain $\mathcal{A}$, we need to find (i) the region around UE_0 where the interfering APs exist that are within the main lobe and side lobes of UE_0, χ_{m} and χ_{s}, respectively, and (ii) the distance from UE_0 to the boundary of the region around UE_0 where *dominant interferers* can exist. We next find these quantities one after the other.

Considering the vertical heights of the THz devices and the fact that directional antennas are used at UE_0, we obtain χ_{m} as a truncated annular region in the horizontal plane, as shown in Fig. 5.5, where

$$\chi_{\mathrm{m}} = \left\{(l,\theta), l \in \left[\check{l}_{00}, \widehat{l}_{00}\right], \theta \in \Theta_{\mathrm{m}}\right\}, \tag{5.20}$$

with

$$\check{l}_{00} = \begin{cases} \frac{h_\epsilon\left(l_{00} - h_\epsilon \tan\left(\frac{\varphi_{\mathrm{U,V}}}{2}\right)\right)}{h_\epsilon + l_{00}\tan\left(\frac{\varphi_{\mathrm{U,V}}}{2}\right)}, & \text{if } \psi_{00} \leq \frac{\pi - \varphi_{\mathrm{U,V}}}{2}, \\ 0, & \text{otherwise}, \end{cases} \tag{5.21}$$

$$\widehat{l}_{00} = \begin{cases} \frac{h_\epsilon\left(l_{00} + h_\epsilon \tan\left(\frac{\varphi_{\mathrm{U,V}}}{2}\right)\right)}{h_\epsilon - l_{00}\tan\left(\frac{\varphi_{\mathrm{U,V}}}{2}\right)}, & \text{if } \psi_{00} \geq \frac{\varphi_{\mathrm{U,V}}}{2}, \\ \infty, & \text{otherwise}, \end{cases} \tag{5.22}$$

and , $\Theta_{\mathrm{m}} = \left\{\theta, \theta \in \left[\theta_{00} - \frac{\varphi_{\mathrm{U,H}}}{2}, \theta_{00} + \frac{\varphi_{\mathrm{U,H}}}{2}\right]\right\}$. We clarify that θ_{ij} is the angle that the projection of the UE$_j$-AP$_i$ link onto the horizontal plane forms with a given reference line in the horizontal plane. Based on the knowledge of geometry and [116, Eq (1.313.9)], we obtain $\check{l}_{00}$ and $\widehat{l}_{00}$ as in (5.21) and (5.22), respectively. Next, considering the "self-blockage zone", we obtain χ_{s} as

$$\chi_{\mathrm{s}} = \left\{(l, \theta), \left(l \in \left(\left(0, \check{l}_{00}\right) \cup \left(\widehat{l}_{00}, \infty\right]\right), \theta \in \Theta_{\mathrm{m}}\right) \cup \left(l \in [0, \infty], \theta \in \Theta_{\mathrm{s}}\right)\right\}, \tag{5.23}$$

where $\Theta_{\mathrm{s}} = \left\{\theta, \theta \in \left(\left(\theta_{00} + \frac{\varphi_{\mathrm{U,H}}}{2}, \pi + \theta_{00} - \frac{\vartheta}{2}\right] \cup \left[\pi + \theta_{00} + \frac{\vartheta}{2}, 2\pi + \theta_{00} - \frac{\varphi_{\mathrm{U,H}}}{2}\right]\right)\right\}$. Next, we derive the boundary of the region around UE$_0$ where *dominant interferers* can exist in the following proposition.

Proposition 5.2 *The distance from UE$_0$ to the boundary of the region around UE$_0$ where dominant interferers can exist is*

$$D = \sqrt{\left(\frac{2}{k(f)} W\left[\frac{k(f)}{2}\sqrt{\frac{\widehat{\varrho}_{\kappa,\iota}\ \Upsilon_{\mathrm{thr}}}{p^r_{m,m}(l_{00}) - \Upsilon_{\mathrm{thr}} N_0 b}}\right]\right)^2 - {h_\epsilon}^2}. \tag{5.24}$$

Proof: We recall that if an interferer is a dominant interferer, it causes outage at UE$_0$ when none of the other interferers contribute to the aggregated interference. Therefore, the SINR when only a dominant interferer contributes to the aggregated interference should be less than the predefined SINR threshold Υ_{thr}.

Mathematically, it is written as

$$\frac{p^r_{m,m}(l_{00})}{N_0 b + \widehat{\varrho}_{\kappa,\iota}\ (d(l^D_{i,0}))^{-2} e^{-k(f)d(l^D_{i,0})}} \leq\ \Upsilon_{\text{thr}}. \tag{5.25}$$

where $l^D_{i,0}$ denotes the horizontal distance between a dominant interferer and UE$_0$. By rearranging (5.25)*, we obtain*

$$\frac{k(f)d(l^D_{i,0})}{2} e^{\frac{k(f)d(l^D_{i,0})}{2}} \leq \frac{k(f)}{2}\sqrt{\frac{\widehat{\varrho}_{\kappa,\iota}\ \ \Upsilon_{\text{thr}}}{p^r_{m,m}(l_{00}) -\ \Upsilon_{\text{thr}} N_0 b}}. \tag{5.26}$$

Next, we apply the definition of the Lambert W-function to (5.26)*, which leads to*

$$\sqrt{(l^D_{i,0})^2 + h^2_\epsilon} \leq \frac{2}{k(f)} W\left[\frac{k(f)}{2}\sqrt{\frac{\widehat{\varrho}_{\kappa,\iota}\ \ \Upsilon_{\text{thr}}}{p^r_{m,m} -\ \Upsilon_{\text{thr}} N_0 b}}\right]. \tag{5.27}$$

Thereafter, we note that D is given by $D = \max(l^D_{i,0})$. Hence, we rearrange (5.27) *to obtain* (5.24). ■

We clarify that there are four possibilities for D in (5.24). This is due to the fact that the effective antenna gains at the *dominant interferer* and UE$_0$, corresponding to the link between the *dominant interferer* and UE$_0$, respectively, can each take two different values. Considering this, we define the four possibilities for D as $D_{\kappa,\iota}$ where $\kappa \in \{\text{m,s}\}$ and $\iota \in \{\text{m,s}\}$.

We next jointly consider χ_{m}, χ_{s}, and $D_{\kappa,\iota}$ to obtain the region around UE$_0$ where *dominant interferers* can exist, i.e., $\mathcal{A}$. We can obtain $\mathcal{A}$ as a combination of four regions which are denoted by $\mathcal{A}_{\kappa,\iota}$ where $\kappa \in \{\text{m,s}\}$ and $\iota \in \{\text{m,s}\}$. For example, $\mathcal{A}_{\text{m,s}}$ denotes the region where *dominant interferers* that are within the main lobe of UE$_0$ while having its side lobes facing UE$_0$ exist. Following the fact that $D_{\kappa,\iota} \gtrless \check{l}_{00}$ and $D_{\kappa,\iota} \gtrless \widehat{l}_{00}$, we obtain these region as

$$\mathcal{A}_{\text{m},\iota} = \left\{(l,\theta), l \in \left[\check{l}_{00}, v_{\text{m},\iota}\right], \theta \in \Theta_{\text{m}}\right\}, \tag{5.28}$$

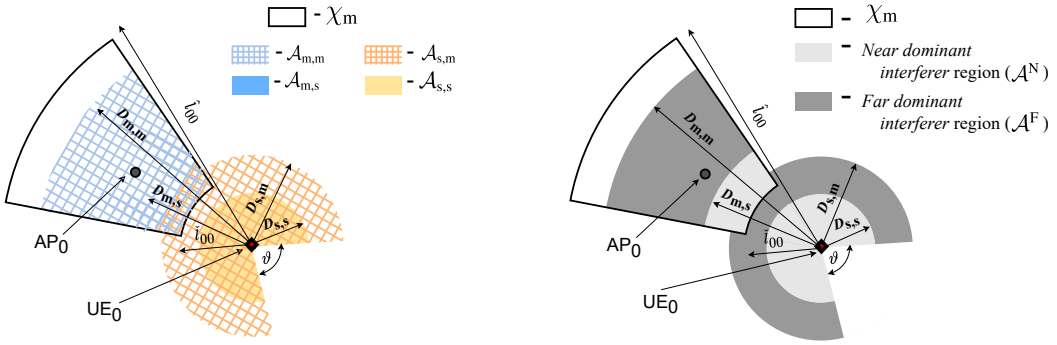

(a) The regions $\mathcal{A}_{\mathrm{m,m}}$, $\mathcal{A}_{\mathrm{m,s}}$, $\mathcal{A}_{\mathrm{s,m}}$, and $\mathcal{A}_{\mathrm{s,s}}$ (b) *Near* and *far dominant interferer* regions

Figure 5.5: Illustration of the regions corresponding to the *dominant interferers* when $D_{\mathrm{s,s}} < \check{l}_{00} < D_{\mathrm{s,m}} < D_{\mathrm{m,s}} < D_{\mathrm{m,m}} < \widehat{l}_{00}$.

where $\iota \in \{\mathrm{m}, \mathrm{s}\}$, $v_{\mathrm{m,m}} = \min\{\widehat{l}_{00}, D_{\mathrm{m,m}}\}$, and $v_{\mathrm{m,s}} = \max\{\check{l}_{00}, \min\{\widehat{l}_{00}, D_{\mathrm{m,s}}\}\}$, and

$$\mathcal{A}_{\mathrm{s},\iota} = \Big\{(l,\theta), \Big(l \in \Big([0, v_{\mathrm{s},\iota,1}] \cup \Big[\widehat{l}_{00}, v_{\mathrm{s},\iota,2}\Big]\Big), \theta \in \Theta_\mathrm{m}\Big) \cup \big(l \in [0, D_{\mathrm{s},\iota}], \theta \in \Theta_\mathrm{s}\big)\Big\}, \tag{5.29}$$

where $v_{\mathrm{s},\iota,1} = \min\{\check{l}_{00}, D_{\mathrm{s},\iota}\}$ and $v_{\mathrm{s},\iota,2} = \max\{\widehat{l}_{00}, D_{\mathrm{s},\iota}\}$ with $\iota \in \{\mathrm{m}, \mathrm{s}\}$.

Fig. 5.5(a) illustrates these regions when $D_{\mathrm{s,s}} < \check{l}_{00} < D_{\mathrm{s,m}} < D_{\mathrm{m,s}} < D_{\mathrm{m,m}} < \widehat{l}_{00}$. By examining these regions, we observe that $\mathcal{A}_{\mathrm{m,s}} \subset \mathcal{A}_{\mathrm{m,m}}$ and $\mathcal{A}_{\mathrm{s,s}} \subset \mathcal{A}_{\mathrm{s,m}}$. Hence, we can interpret that the interferers that are within the regions $\mathcal{A}_{\mathrm{m,s}}$ and $\mathcal{A}_{\mathrm{s,s}}$ cause outage by themselves while having its main lobe or the side lobes facing UE_0, i.e., *near dominant interferers*. We denote the region where *near dominant interferers* exist as $\mathcal{A}^\mathrm{N}$, where

$$\mathcal{A}^\mathrm{N} = (\mathcal{A}_{\mathrm{m,m}} \cap \mathcal{A}_{\mathrm{m,s}}) \cup (\mathcal{A}_{\mathrm{s,m}} \cap \mathcal{A}_{\mathrm{s,s}}) = \mathcal{A}_{\mathrm{m,s}} \cup \mathcal{A}_{\mathrm{s,s}}. \tag{5.30}$$

Similarly, we obtain the regions where the interferers that cause outage by themselves, only when its main lobe is facing UE_0, i.e., *far dominant interferers*, exist as

$$\mathcal{A}^\mathrm{F} = (\mathcal{A}_{\mathrm{m,m}} \cup \mathcal{A}_{\mathrm{m,s}}) \cup (\mathcal{A}_{\mathrm{s,m}} \cup \mathcal{A}_{\mathrm{s,s}}) - \mathcal{A}^\mathrm{N} = \mathcal{A} - \mathcal{A}^\mathrm{N}. \tag{5.31}$$

Fig. 5.5(b) illustrates the regions corresponding to the *near* and *far dominant interferers* when $D_{\mathrm{s,s}} < \check{l}_{00} < D_{\mathrm{s,m}} < D_{\mathrm{m,s}} < D_{\mathrm{m,m}} < \widehat{l}_{00}$.

Using the regions $\mathcal{A}^{\mathrm{N}}$, $\mathcal{A}^{\mathrm{F}}$ and the results in Section 5.3, we next derive the average number of *near* and *far dominant interferers* that exist around UE_0. The results are presented in the following propositions.

Proposition 5.3 *The average number of near dominant interferers that exist around UE_0 for the THzCom system is derived as*

$$\begin{aligned}
&\Lambda_{\Phi^N} \\
&= \frac{\lambda_A \zeta \varphi_{U,H}}{\widetilde{\lambda}^2}\Big[-e^{-\widetilde{\lambda} v_{s,s,1}}(1+\widetilde{\lambda} v_{s,s,1}) - e^{-\widetilde{\lambda} v_{m,s}}(1+\widetilde{\lambda} v_{m,s}) + e^{-\widetilde{\lambda}\check{l}_{00}}(1+\widetilde{\lambda}\check{l}_{00}) - e^{-\widetilde{\lambda} v_{s,s,2}}(1+\widetilde{\lambda} v_{s,s,2}) \\
&\quad + e^{-\widetilde{\lambda}\widehat{l}_{00}}(1+\widetilde{\lambda}\widehat{l}_{00}) + e^{-\widetilde{\lambda} D_{s,s}}(1+\widetilde{\lambda} D_{s,s})\Big] + \frac{\lambda_A \zeta\,(2\pi-\vartheta)}{\widetilde{\lambda}^2}\left[1 - e^{-\widetilde{\lambda} D_{s,s}}(1+\widetilde{\lambda} D_{s,s})\right].
\end{aligned} \tag{5.32}$$

Proof: See Appendix C.4. ■

Proposition 5.4 *The average number of far dominant interferers that exist around UE_0 for the THzCom system is derived as*

$$\begin{aligned}
&\Lambda_{\Phi^F} \\
&= \frac{\lambda_A \zeta \varphi_{A,H} \varphi_{U,H}}{2\pi}\Big[\digamma_D(v_{s,s,1}, v_{s,m,1}) + \digamma_D(v_{m,s}, v_{m,m}) + \digamma_D(v_{s,s,2}, v_{s,m,2}) \\
&\qquad - \digamma_D(D_{s,s}, D_{s,m})\Big] + \frac{\lambda_A \zeta \varphi_{A,H}\,(2\pi-\vartheta)}{2\pi}\digamma_D(D_{s,s}, D_{s,m}),
\end{aligned} \tag{5.33}$$

where $\digamma_D(a,b) = \int_a^b \rho_V^{hp}(l) e^{-\widetilde{\lambda} l}\, l\, dx$, which can be calculated numerically.

Proof: See Appendix C.5. ■

5.5 Numerical Results and Discussion

In this section, we investigate the reliability performance of the considered 3D THzCom system. To this end, we first examine the impact of the derived hitting probability on the 3D THzCom system. Thereafter, we assess the accuracy and

Table 5.3: Values of system parameters used for numerical results in Section 5.5.

Parameter	**Symbol**	**Value**
Heights of APs and UEs	h_{A}, h_{U}	3.0 m, 1.3 m
Density of APs	λ_{A}	0.1 m^{-2}
Operating frequency	f	1.05 THz
Molecular absorption coefficient	$k(f)$	0.07512 m^{-1}
Operating bandwidth	b	5 GHz
AP's antenna parameters	$G_{\mathrm{A}}^{\mathrm{m}}$, $G_{\mathrm{A}}^{\mathrm{s}}$, $\varphi_{\mathrm{A,H}}$, $\varphi_{\mathrm{A,V}}$	25 dBi, -10 dBi, 10°, 10°
UE's antenna parameters	$G_{\mathrm{U}}^{\mathrm{m}}$, $G_{\mathrm{U}}^{\mathrm{s}}$, $\varphi_{\mathrm{U,H}}$, $\varphi_{\mathrm{U,V}}$	15 dBi, -10 dBi, 33°, 33°
Transmit power	p^{t}	5 dBm
Noise spectral density	N_0	-174 dBm/Hz
SINR threshold	Υ_{thr}	3 dB
Self-blockage angle	ϑ	60°
Height and speed of human blockers	h_{B}, v_{B}	1.7 m, 1 ms^{-1}
Widths of human blockers	$L_{\mathrm{B},1}$, $L_{\mathrm{B},2}$	0.6 m, 0.3 m
Average length of wall blockers	$\mathbb{E}[L_{\mathrm{W}}]$	3.0 m
Density of wall blockers	λ_{W}	0.04 m^{-2}

examine the significance of our derived coverage probabilities. Finally, we investigate the effects of system parameters on the coverage probabilities, especially the blockage parameters.

The simulation results are obtained using a framework that operates in a time-driven regime [126] and considering a rectangular indoor environment of size 60 m $\times$ 50 m [135]. The values of the parameters used in this section are summarized in Table 5.3, unless specified otherwise. The chosen values are consistent with other relevant studies in the literature [29, 33, 71, 127, 129]. In this chapter, we use the absorption coefficient values that are calculated for the standard atmosphere with 10% humidity [29]. Also, we consider $\varphi_{\Psi,\mathrm{H}} = \varphi_{\Psi,\mathrm{V}}$. While our analysis uses the dominant interferer assumption, the simulations consider the interference from all interferers that exist within the rectangular indoor environment.

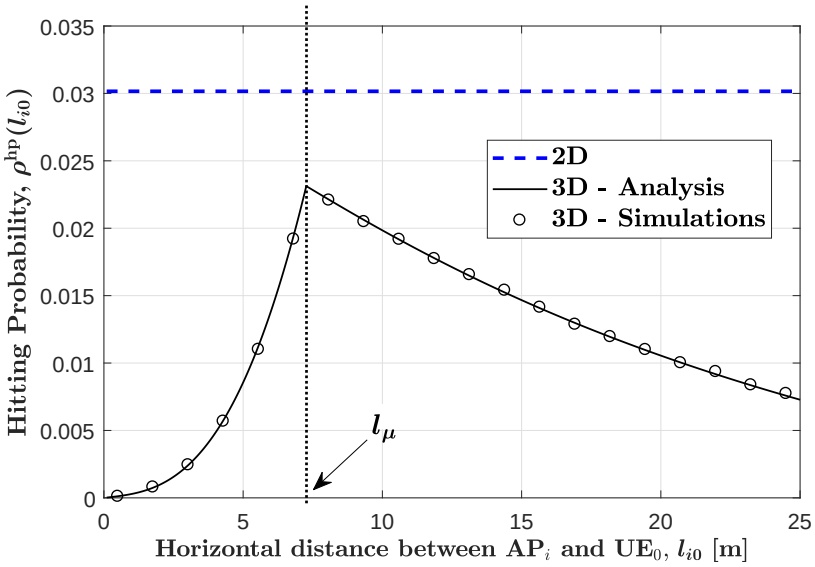

Figure 5.6: Hitting probability versus the horizontal distance between UE_0 and AP_i for L_{T}=12.2 m.

5.5.1 Hitting Probability

Fig. 5.6 plots the hitting probability for the UE_0-AP_i link, i.e., $\rho^{\mathrm{hp}}(l_{i0})$ in Proposition 5.1, versus the horizontal distance between UE_0 and AP_i, l_{i0}, for $L_{\mathrm{T}} = 12.2$ m. In addition, the hitting probability for the 2D model is also plotted as a reference. We first observe that the analytical results for the hitting probability match well with the simulation results, which demonstrates the correctness of our analysis. Second, we observe that the hitting probability is very small for low l_{i0}, increases when l_{i0} increases up to l_μ, and thereafter starts to decrease. This observation is in accordance with Remark 5.1, which further validates our analysis. Third, we observe that the hitting probability is significantly overestimated when the simplified 2D model is adopted as in previous studies that investigated coverage of THzCom systems. This demonstrates the importance of examining the performance of THz systems in a 3D environment.

5.5.2 Coverage Probability

Fig. 5.7 plots the coverage probability versus the horizontal distance between AP_0 and UE_0 for the typical indoor and open office environments. We clarify that

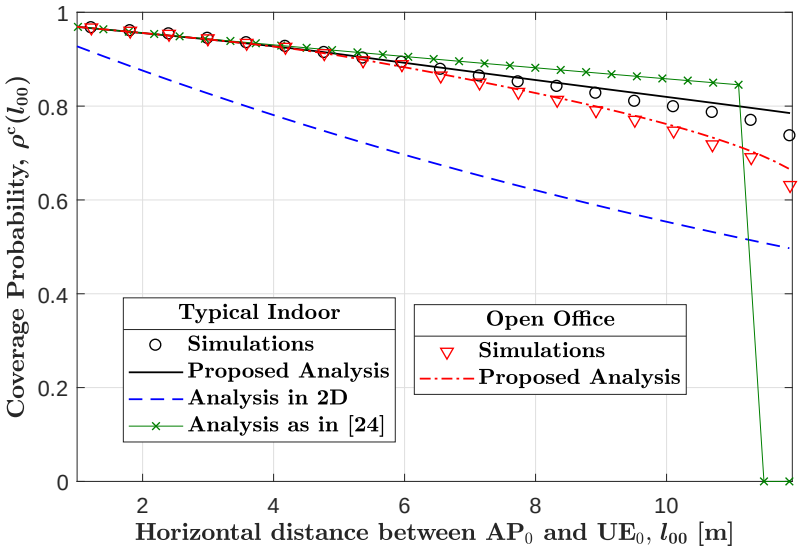

Figure 5.7: The coverage probability versus the horizontal distance between AP_0 and UE_0 for the typical indoor and the open office environment.

as mentioned in 3GPP standards [135], the open office environment where only human blockers exist is another interesting scenario for studies above-6 GHz. Thus, while presenting numerical results for the THzCom system in the typical indoor environment outlined in Section 5.2, we also present the numerical results for the THzCom system in an open office environment in Fig. 5.7.[7] In this figure, for the typical indoor environment, we plot (i) the simulated coverage probabilities in the considered in the 3D model, (ii) the coverage probabilities derived as per the proposed analysis in the 3D model, (iii) the coverage probabilities derived as per the analysis in [74] in the 3D model, and (iv) the coverage probabilities derived as per the proposed analysis in the 2D model, which is obtained by setting $\widetilde{\lambda}_{\mathrm{B}}$ in (5.7) as $\widetilde{\lambda}_{\mathrm{B}} = \frac{2(L_{\mathrm{B},1}+L_{\mathrm{B},2})\lambda_{\mathrm{B}}}{\pi}$, and $\rho_{\mathrm{V}}^{\mathrm{hp}}(l_{ij})$ in (5.15) as $\rho_{\mathrm{V}}^{\mathrm{hp}}(l_{ij}) = 1$ for $\forall i, j$.

We first observe that our analysis well matches the simulations for small and medium l_{00} for both the open office and the typical indoor environment, which demonstrates the correctness of our analysis. For high l_{00}, our analysis slightly overestimates the coverage probability for both the open office and the typical indoor environment. The slight overestimation for the open office environment is

[7]We clarify that for the open office environment and (i) simulations are carried out while considering no wall blockers, (ii) analytical results are obtained by considering $\lambda_{\mathrm{W}} = 0$.

due to the fact that our analysis is under the assumption that any combination of *non-dominant interferers* cannot lead to the outage. However, non-negligible possibilities of *non-dominant interferers* causing an outage to appear since there are more *non-dominant interferers* within the beamwidth of the UE for high l_{00}, which yields the slight overestimation. Differently, for the typical indoor environment, a much smaller overestimation appears. This is because, although we consider that the number of walls that intersect each link is independent, non-negligible dependencies appear in the number of walls that intersect each link.

Second, we observe a gradual decrease in the coverage probability when l_{00} increases for both the open office and the typical indoor environment. This is due to the fact that when the UE_0 is connected to a farther AP, in addition to the reduced received power, the impact of interference on the coverage probability becomes more detrimental since there are more interferers within the beamwidth of the UE_0. Moreover, the effective number of blockers that exist in the UE_0-AP_0 link increases with l_{00}, thereby further deteriorating the coverage probability. In addition, we observe that the coverage probability for the typical indoor environment is higher than that of the open office environment, especially when l_{00} is high. This is due to the fact that since there are wall blockers in addition to human blockers in a typical indoor environment, the likelihood of interference signals being blocked becomes higher, which improves the coverage probability.

We next compare the coverage probability obtained using our analysis with that obtained in previous studies. We first observe that the coverage probability is significantly underestimated when the analysis is performed using the 2D model as in [72–75, 86–88, 113]. This is due to the fact that in the 2D model, the blockage and hitting probabilities are overestimated since vertical heights of the THz devices are ignored. This in turn underestimates the received power, and overestimates the interference at UE_0, thereby leading to the underestimation of the coverage probability. This observation reveals that the vertical heights of THz devices profoundly impact the coverage probability of THzCom systems; therefore, ignoring them leads to an underestimation of the reliability of the system. Moreover, we observe that the underestimation of the coverage probability when the analysis is performed using the 2D model increases when the AP_0 to UE_0 link distance increases. Second, we observe that the analysis in [74], which is based on

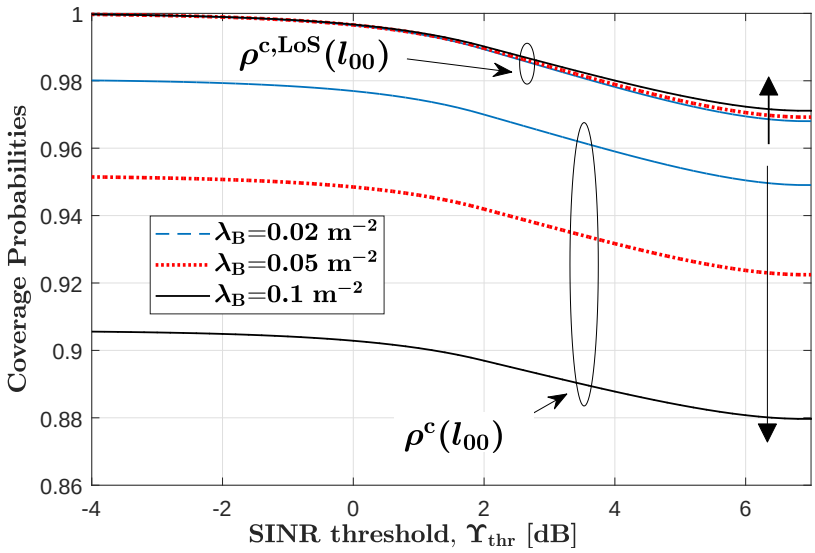

Figure 5.8: The coverage probability versus the SINR threshold for the typical indoor environment with different human blocker densities.

average interference, approximates the coverage probability well for low l_{00}, but the accuracy significantly deteriorates when l_{00} increases. In comparison, our analysis approximates the coverage probability very well for all l_{00}.

Impact of SINR Threshold and Blocker Densities: Fig. 5.8 plots the coverage probability, $\rho^{c}(l_{00})$, versus the SINR Threshold, Υ_{thr}, for different densities of human blockers, λ_{B}, when $l_{00} = 6$ m. We also plot the coverage probability when the UE_0-AP_0 link is in LoS, i.e., $\rho^{c,\mathrm{LoS}}(l_{00})$ in (5.18), which is used as a metric of interest in [82, 89]. We observe that $\rho^{c}(l_{00})$ and $\rho^{c,\mathrm{LoS}}(l_{00})$ become lower when Υ_{thr} increases. In addition, we observe that an increase in λ_{B} leads to a slight improvement in $\rho^{c,\mathrm{LoS}}(l_0)$, but a significantly decrease in $\rho^{c}(l_{00})$. When there are more blockers, the likelihood of interference signals being blocked becomes higher, which leads to higher $\rho^{c,\mathrm{LoS}}(l_0)$. However, the increase in λ_{B} increases the likelihood of AP_0 being blocked, leading to worse $\rho^{c}(l_{00})$. These observations on $\rho^{c}(l_{00})$ and $\rho^{c,\mathrm{LoS}}(l_0)$ for varying blocker densities indicate that it is important to carefully select system parameters, e.g., antenna gains, transmit power or density of APs, to obtain the desired reliability performance depending on the density of humans in the indoor environment.

Impact of Antenna Parameters of UEs and APs: Fig. 5.9 plots the

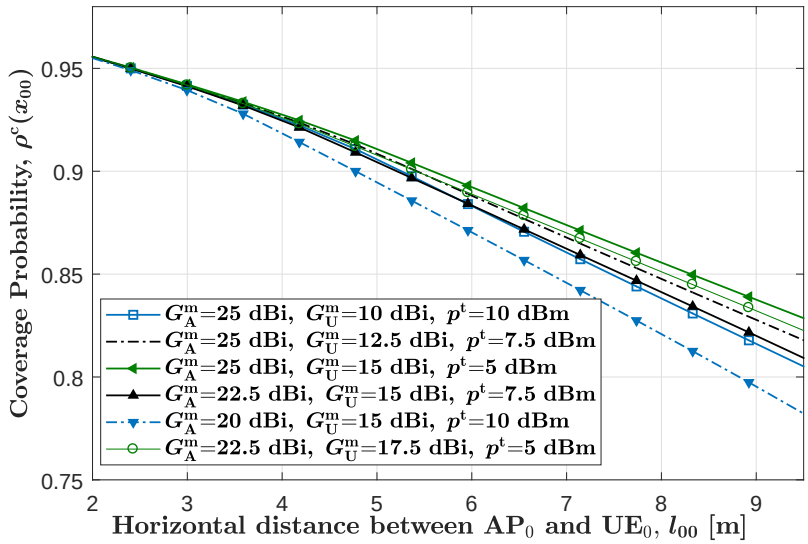

Figure 5.9: The coverage probability versus the UE$_0$-AP$_0$ link distance for the typical indoor environment with different antenna gains at UEs and APs.

coverage probability versus l_{00} for different antenna main lobe gains at APs and UEs, i.e., $G_{\mathrm{A}}^{\mathrm{m}}$ and $G_{\mathrm{U}}^{\mathrm{m}}$. In this figure, we keep $p^{\mathrm{t}}G_{\mathrm{A}}^{\mathrm{m}}G_{\mathrm{U}}^{\mathrm{m}}$ unchanged for the sake of a fair comparison. We first observe that the improvement in the coverage probability when $G_{\mathrm{A}}^{\mathrm{m}}$ and $G_{\mathrm{U}}^{\mathrm{m}}$ are increased is marginal for low l_{00} , but is noticeably high for larger l_{00}. This is due to the fact that the deterioration in the coverage probability caused by interference and the blockage is marginal for small l_0, but increases when l_0 becomes large. Thus, the opportunity for coverage improvement by increasing the antenna gains is higher for larger l_{00}. This reveals that the coverage performance of THzCom systems can be improved by increasing the antenna directivity at both the APs and the UEs for larger l_{00}. Second, observing the curves with the same p^{t}, we find that the coverage probability improvement brought by increasing $G_{\mathrm{A}}^{\mathrm{m}}$ is higher than that brought by increasing $G_{\mathrm{U}}^{\mathrm{m}}$. This implies that it is more worthwhile to increase the antenna directivity at the APs than at the UEs, to produce a more reliable THzCom system.

Impact of Operating Frequency and AP Densities: Fig. 5.10 plots the coverage probability versus the operating frequency for different values of AP densities in the first transmission window (TW) above 1 THz, when $l_{00} = 6$ m. First, we observe that the coverage probability remains almost unchanged throughout the

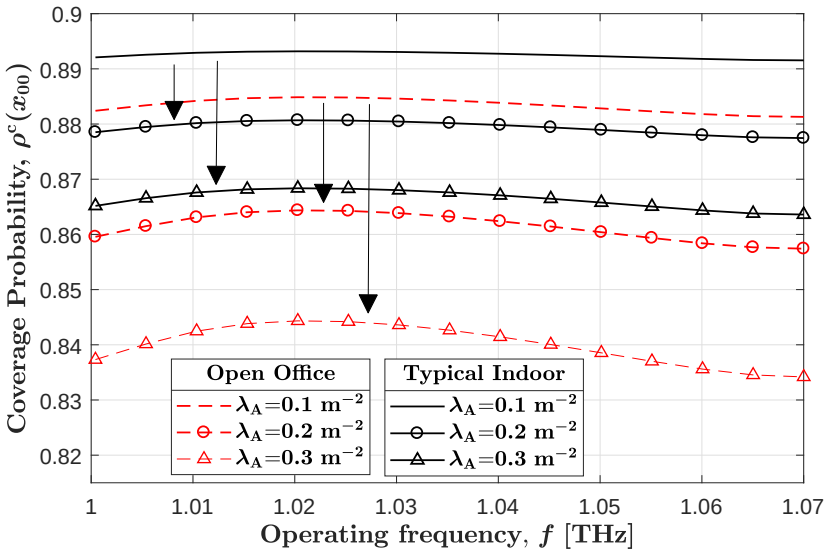

Figure 5.10: The coverage probability versus the operating frequency for different values of AP densities.

TW, despite the path loss varying drastically within the TW as shown in Fig. 1.2 due to frequency-dependent absorption loss. This is due to the fact when the operating frequency is changed, while the received power from the desired link changes, the interference power also changes in a similar manner. This results in coverage remaining almost unchanged throughout the TW. Second, we observe that the coverage probability significantly decreases when the density of APs becomes higher for both typical indoor and open offices, due to the increased impact from interferers. Third, we observe that the deterioration in the coverage probability due to the increased density of APs is less for a typical indoor environment than that in an open office environment. This is due to the fact that when there are wall blockers in a typical indoor environment, the likelihood of interference signals being blocked becomes higher, which leads to better coverage probability. The second and third observations above demonstrate that the network densification deteriorates the reliability of THzCom systems, and that it is necessary to carefully select the AP densities to obtain the desired reliability performance depending on the communication environment of interest.

5.6 Summary

In this chapter, we investigated (i) the modeling and analysis of different types of blockages in a 3D THzCom system and (ii) the coverage probability of an indoor THzCom system when frequency reuse is considered. We first modeled a realistic 3D THz system, where we considered the unique molecular absorption loss at the THz band, 3D directional antennas at both UEs and APs, and the interference from the nearby APs. Differing from the existing THz studies, we considered the joint impact of the blockage caused by the user itself, moving humans, and wall blockers, as well as the effect of the vertical heights of the THz devices. We then derived the blockage and hitting probabilities. Moreover, we derived a new expression for the coverage probability using the dominant interferer analysis for the considered indoor environment. Using numerical results, we validated our analysis and demonstrated that the coverage probability is significantly underestimated when the impact of vertical heights of communication entities is ignored in the analysis. We also found that an increase in the density of human blockers leads to a slight improvement in the coverage probability when the transmission link of interest is in LoS, but reduces the overall coverage probability.

Chapter 6

Conclusions and Future Research Directions

In this chapter, we first summarize the general conclusions drawn from the thesis. We then outline some of the research directions directly related to the thesis.

6.1 Thesis Conclusions

This thesis focused on the design and analysis of novel and efficient spectrum allocation strategies for multiuser THzCom systems. Specifically, the thesis investigated several research challenges encountered by multi-band-based spectrum allocation schemes, and proposed efficient designs and analytical frameworks to alleviate them. The detailed contributions are given as follows:

Spectrum Allocation with ASB: In Chapter 2, we, for the first time, proposed multi-band-based spectrum allocation with ASB to improve the spectral efficiency of multiuser THzCom systems, by allowing to divide the to-be-allocated spectrum into sub-bands with unequal bandwidth. To study the impact of ASB, we formulated a resource allocation problem, with the main emphasis on spectrum allocation with ASB, while aiming to maximize the data rate of the multiuser THzCom system under given constraints on sub-band bandwidth and power. We then proposed a solution approach to derive the sub-band bandwidth and optimal transmit power of the formulated resource allocation problem. Specifically,

we proposed reasonable approximations, as well as transformations, and arrived at an approximate convex problem, which can be solved efficiently by using standard convex problem solvers. Based on our numerical investigation, we showed that consideration of ASB leads to a significantly higher data rate as compared to the consideration of ESB; thus, it is beneficial to adopt ASB in multi-band-based spectrum allocation schemes. We also showed that the performance gain of adopting ASB is most profound when the variation in molecular absorption loss within the to-be-allocated spectrum is high.

Spectrum Allocation Among Multiple TWs for THzCom Systems: In Chapter 3, we proposed a novel spectrum allocation strategy for multiuser THzCom systems when the to-be-allocated spectrum is composed of multiple TWs. Specifically, we explored the benefits of (i) sub-band assignment, (ii) avoiding using some spectra that exist at the edges of TWs where molecular absorption loss is very high, and (iii) ASB when the to-be-allocated spectrum is composed of multiple TWs. With these considerations in mind, we formulated a resource allocation problem, with the primary focus on spectrum allocation, to maximize the aggregated multiuser data rate. We then proposed a solution approach to derive the sub-band assignment, sub-band bandwidth, the unused spectra at the edges of TW, and the transmit power of the formulated resource allocation problem. Specifically, we first proposed modifications to the formulated problem and arrived at a mixed-integer non-linear problem. We then proposed several transformations, including the binary variable to real variable transformation, and arrived at an approximate convex problem. Subsequently, we developed an iterative algorithm based on the SCA technique to solve the approximate convex problem. Based on our numerical investigation, we first showed that the proposed sub-band assignment can be utilized when the to-be-allocated spectrum is composed of multiple TWs since DAMC-based sub-band assignment is only readily applicable within a TW. We then showed that additional data rate gains can be obtained by optimally determining the unused spectra at the edges of TWs, as compared to avoiding using pre-defined spectra that exist at the edges of TWs. Finally, we showed that the feasibility region of the resource allocation problem can be improved by adopting ASB and optimally determining the unused spectra at the edges of TWs.

An Unsupervised Learning Approach for Spectrum Allocation in

THzCom Systems: In Chapter 4, we proposed an unsupervised learning-based approach to obtaining the near-optimal solution to the multi-band-based spectrum allocation problem with ASB when the molecular absorption coefficient varies in a highly non-linear manner. In the proposed approach, we first train a DNN while utilizing a loss function that is inspired by the Lagrangian of the formulated problem. Then using the trained DNN, we approximated the near-optimal sub-band bandwidth and transmit power. Based on our numerical investigation, we showed that when the values of the molecular absorption coefficient within the to-be-allocated spectrum change rapidly and thus cannot be modeled as an exponential function of frequency, the proposed unsupervised learning-based approach outperforms the existing approximate approaches.

Blockage and Coverage Analysis for 3D THzCom Systems: In Chapter 5, we investigated (i) the modeling and analysis of different types of blockages in 3D THzCom systems and (ii) the coverage probability of an indoor THzCom system when frequency reuse is considered. We first characterized the joint impact of blockages caused by the user itself, moving humans and wall blockers in a 3D THzCom environment, and derived the blockage probabilities associated with a point-to-point THzCom link. Also, we considered the effect of 3D directional antennas and derived the hitting probability. We then developed a tractable analytical framework, using stochastic geometry, to evaluate the coverage probability by characterizing the regions where dominant interferers can exist, and the average number of interferers that exist in these regions. Based on our numerical investigation, we first verified our analysis by comparing it to simulation results. We then showed that the throughput and the reliability of THzCom systems are greatly impacted by the density of blockers; thus, system parameters, e.g., power budget and maximum sub-band bandwidth, have to be carefully selected for achieving the desired throughput and reliability performance, depending on the density of human blockers in the indoor environment. We finally showed that network densification deteriorates the reliability of THzCom systems; thus, it is necessary to carefully select the AP densities to obtain the desired reliability performance depending on the communication environment of interest.

This thesis advanced our understanding of the fundamentals of spectrum allocation strategies for THzCom systems. It also provided design guidelines and

analytical frameworks to solve important problems on how to efficiently utilize the THz band to develop ready-to-use THzCom systems in years to come.

6.2 Future Research Directions

This thesis studied novel and efficient spectrum allocation strategies for multiuser THzCom systems. As the research topic is exploratory in nature, a number of potential research problems naturally arise. In this regard, a few promising research directions directly related to the thesis are briefly discussed in the following for future consideration.

- In the proposed spectrum allocation designs in Chapters 2, 3, and 4, we considered that the users in the system are served by separate sub-bands to ensure the data transmission to be free of Intra-BI and eliminate the signal processing overhead and hardware complexity caused by frequency reuse in the system. However, higher spectral efficiency can be achieved by leveraging sub-band reuse during spectrum allocation. Thus, the need exists to design spectrum allocation strategies while considering frequency reuse. New spatial and power-domain multiplexing strategies operated at the THz band need to be developed for adopting frequency reuse in THzCom systems. Some of the key research challenges related to the deployment of spatial and power-domain multiplexing strategies at the THz band, such as beam sectorization and NOMA, are detailed in Section 1.2.6.2.

- In the proposed spectrum allocation designs in Chapters 2, 3, and 4, we consider the guard band bandwidth to be fixed and pre-defined. However, to further improve the spectral efficiency, it may be beneficial to optimally design the values of guard band bandwidths. When guard band bandwidths are to be optimally designed, the impacts of Inter-BI, interference cancelation capabilities of the users, QoS requirements of the users such as tolerable interference and required data rate, and the spectral efficiency of the system need to be jointly considered.

- In the proposed spectrum allocation designs in Chapters 2, 3, and 4, per-

fect CSI is assumed. However, perfect CSI cannot be always guaranteed, and thus it would be interesting to investigate the design of spectrum allocation strategies while considering the uncertainty that occurs as a result of imperfect CSI.

- In the proposed spectrum allocation designs in Chapters 2, 3, and 4, we ignore the impact of Inter-BI due to the consideration of guard bands existing between sub-bands. However, the total mitigation of Inter-BI is not guaranteed, unless the guard band bandwidth is set to a higher value. Thus, the impact of Inter-BI needs to be precisely modeled and then analyzed when sub-bands are close to each other. As mentioned in Section 1.2.4, Gaussian approximation has been widely used to model Inter-BI at sub-6 GHz and mmWave frequencies, assuming that neighboring sub-bands have similar channel quality. However, the applicability of this approximation at the THz band needs to be re-examined, since the adjacent THz sub-bands exhibit drastically different channel qualities, due to molecular absorption loss.

- A deterministic THz band channel is considered in this thesis while ignoring the impacts of nLoS rays and fading. However, the consideration of nLoS rays and fading can lead to a more accurate characterization of the considered THzCom system, which needs to be addressed in future works.

- THzCom will be underpinned by (massive) multiple-input-multiple-output (MIMO) technologies to compensate for the substantial path and penetration losses. Throughout the thesis, fixed antenna gains are considered for THz transceivers while ignoring the impacts of THz band antenna arrays and beamforming designs. However, it is of utmost importance to consider the impacts of THz band antenna array and beamforming designs for a more accurate characterization of the considered THzCom system. Some of the possible research directions related to THz band antenna arrays and beamforming designs that need investigation are (i) characterization of channel squit effect, (ii) different beamforming architectures such as widely-spaced hybrid beamforming architectures (HBAs), dynamic array-of-subarray (DAoS) HBAs, and unified HBAs, and (iii) graphene technology and THz true-time

delays (TTDs) for THz band antennas.

- To address the reliability degradation caused by blockages at the THz band, promising solutions such as MC and Reconfigurable intelligent surfaces (RISs) need to be explored. Some of the key research challenges associated with the deployment of MC-assisted THzCom systems are detailed in Section 1.2.5.2. As for RIS-assisted THzCom systems, they are still in their early stages and enormous challenges lie ahead. First, given the high reflection loss at THz band, the material of reflector arrays needs to be carefully selected to support RIS at the THz band. For example, at frequencies of 1 THz and beyond, graphene can be used for RIS, due to its tunable properties and low reflection coefficient. Second, tractable models that describe the THz band RIS channel need to be developed and validated through experimental results. Third, the challenges arising during the acquisition of the CSI between the RIS and the involved AP and users need to be addressed. A viable method to overcome this challenge can be that, instead of estimating the RIS-AP and RIS-user channels separately, the concatenated AP-RIS-user channel can be estimated based on direct AP-user channel measurements and some known RIS reflection patterns. Fourth, to integrate RISs with the fixed wireless infrastructure, the design of a dedicated control plane, with appropriate protocols and networking procedures, is desired.

- The need exists for accelerated development of THz devices and testbeds/ prototypes to obtain experimental measurements since the state-of-the-art advances still remain mostly theoretical in nature. Some of the key research challenges related to the development of THz devices and testbeds/prototypes are detailed in Section 1.2.7.

Appendix A

Appendix A

This appendix contains the proof needed in Chapter 2.

A.1 Proof of Lemma 2.1

We prove the concavity of $\widehat{r}_s$ in (2.16) w.r.t. z_ν, where $s, \nu \in \mathcal{S}$. To this end, we rearrange $\widehat{r}_s$ in (2.16) to obtain

$$\widehat{r}_s = b_s(z_s) \log_2 \left(1 + \Upsilon_s^\nu\right), \tag{A.1}$$

where

$$b_s(z_s) = \xi_s + \omega_s \log(\varsigma_s z_s), \tag{A.2}$$

$$\Upsilon_s^\nu = \frac{\varrho e^{-d_s \sigma_3} p_s}{d_s^2} \frac{e^{-\widehat{\sigma}_{s,\nu} d_s e^{-\widehat{a}_{s,\nu} \log(\varsigma_\nu z_\nu)}}}{\left(\widehat{f}_{s,\nu} - \eta a_{s,\nu} \omega_\nu \log(\varsigma_\nu z_\nu)\right)^2 b_s(z_s)}, \tag{A.3}$$

$$\widehat{\sigma}_{s,\nu} = d_s(e^{\sigma_1 + \sigma_2 \widehat{f}_{s,\nu}}) \tag{A.4}$$

$$\widehat{f}_{s,\nu} = f_{\text{ref}} - \eta \left(\sum_{\kappa \in \mathcal{S}} a_{s,\kappa} \xi_\kappa + \sum_{\kappa \in \mathcal{S}/\nu} a_{s,\kappa} \omega_\kappa \log(\varsigma_\kappa z_\kappa) + (s-1) B_{\text{g}} \right). \tag{A.5}$$

Thereafter, while considering the fact that $\widehat{f}_{s,\nu} \gg \eta a_{s,\nu} \omega_\nu \log(\varsigma_\nu z_\nu)$, we take the second derivative of $\widehat{r}_s$ in (A.1) w.r.t. z_ν and rearrange the resulting terms to arrive at

$$\frac{\partial^2 \widehat{r}_s}{\partial z_\nu^2} = \begin{cases} E_{2,1}^{s,\nu}, & \nu < s, \\ E_{2,2}^{s,\nu} & \nu = s, \\ E_{2,3}^{s,\nu}, & \text{elsewhere}, \end{cases} \qquad \forall s, \nu \in \mathcal{S}, \tag{A.6}$$

where

$$E_{2,1}^{s,\nu} = -\frac{b_s(z_s)\widehat{a}_{s,\nu}^2 \Upsilon_s^\nu}{\log(2) z_\nu^2 \left(1+\Upsilon_s^\nu\right)^2}\Big(\left(1+\Upsilon_s^\nu\right)\left(1+\frac{1}{\widehat{a}_{s,\nu}}\right) - d_s\ \widehat{\kappa}(f_s)e^{d_s\sigma_3}\Big) d_s\ \widehat{\kappa}(f_s)e^{d_s\sigma_3}, \tag{A.7}$$

$$E_{2,2}^{s,\nu} = \underbrace{-\frac{\omega_s}{\log(2) z_s^2}\left(\log\left(1+\Upsilon_s^s\right) - \frac{\Upsilon_s^s}{\left(1+\Upsilon_s^s\right)}\right)}_{\text{Term}_1} \underbrace{-\frac{\left(\Upsilon_s^s\right)^2\left(\widehat{a}_{s,s} b_s(z_s) d_s\ \widehat{\kappa}(f_s)e^{d_s\sigma_3} - \omega_s\right)^2}{\log(2)\left(1+\Upsilon_s^s\right)^2 z_s^2 b_s(z_s)}}_{\text{Term}_2}$$
$$\underbrace{-\frac{b_s(z_s)\widehat{a}_{s,s}^2 \Upsilon_s^s}{\log(2) z_s^2\left(1+\Upsilon_s^s\right)}\Big(\left(1+\frac{1}{\widehat{a}_{s,s}}\right) - d_s\ \widehat{\kappa}(f_s)e^{d_s\sigma_3}\Big) d_s\ \widehat{\kappa}(f_s)e^{d_s\sigma_3}}_{\text{Term}_3}, \tag{A.8}$$

and $E_{2,3}^{s,\nu} = 0$. It can be shown that $E_{2,1}^{s,\nu} < 0$ when $1/\omega_\nu > \overline{\omega}$, where

$$\overline{\omega} = |\sigma_2|\left(\widehat{d}_{\max}\widehat{\kappa}(f_{\text{ref}})e^{\widehat{d}_{\max}\sigma_3} - 1\right) \tag{A.9}$$

and $\widehat{d}_{\max} > d_{n_1}$ [55]. Also, it can be shown that $E_{2,2}^{s,\nu} < 0$ when $1/\omega_\nu > \overline{\omega}$, since $\text{Term}_1 < 0$ and $\text{Term}_2 < 0$, $\forall\ s, \nu \in \mathcal{S}$ and $\text{Term}_3 < 0$ when $1/\omega_\nu > \overline{\omega}$. Based on these, we conclude that $\widehat{r}_s$ in (2.16) is concave w.r.t. z_ν when $1/\omega_\nu > \overline{\omega}$.

Appendix B

Appendix B

This appendix contains the proof needed in Chapter 4.

B.1 Proof of Lemma 4.1

According to the RD model, if a human is moving in the area $\mathbb{R}^2$, the PDF of its location is uniform over time [125]. As such, at any given time instant, the locations of human blockers form a PPP with the same density of λ_{B}. This makes it possible to analyze a single time instant and then generalize the results over all time instants, thereby simplifying the mobility-related analysis.

Let us focus on a specific time instant. The region in which a human blocker should appear to block the link between the AP and an user can be approximated by a polygon region between the AP and the user, as shown in Fig. 4.2(b). The dimensions of this polygon region depends on the orientation of the human blocker with respect to the user-AP link [76, Fig. 1]. Considering the area of this polygon region and the fact that the orientations of the human blockers are uniformly distributed between 0 and 2π, we obtain the average number of human blockers that intersect the link the AP and the user assigned to sth sub-band in the 3D environment as

$$n_{\mathrm{B}}^{s} = \left(L_{\mathrm{B},1} L_{\mathrm{B},2} + \frac{2}{\pi} (L_{\mathrm{B},1} + L_{\mathrm{B},2}) \bar{l}_s \right) \lambda_{\mathrm{B}}, \tag{B.1}$$

where $\bar{l}_s = \frac{(h_{\mathrm{B}} - h_{\mathrm{U}})}{(h_{\mathrm{A}} - h_{\mathrm{U}})} l_s$. Thereafter, considering the void probability of human blockers existing within the link between the AP and the user assigned to sth sub-band,

we obtain ρ_s^{nb} as

$$\rho_s^{\mathrm{nb}} = e^{-n_{\mathrm{B}}^s}. \tag{B.2}$$

Finally, substituting (B.1) in (B.2), we arrive at (5.7).

Appendix C

Appendix C

This appendix contains the proofs needed in Chapter 5.

C.1 Proof of Lemma 5.2

The average of the number of walls that intersect the link between AP_i and UE_j for the binary wall orientation is given by

$$\widetilde{\lambda}_{\mathrm{W},ij} = \lambda_{\mathrm{W}} \mathbb{E}\left[L_{\mathrm{W}}\right] \xi(\phi_{ij}) l_{ij}, \tag{C.1}$$

where $\xi(\phi_{ij}) = \frac{1}{2}\left(|\sin(\phi_{ij})| + |\cos(\phi_{ij})|\right)$ with ϕ_{ij} being the angle that the projection of the UE_j-AP_i link onto the horizontal plane forms with a reference line in the horizontal plane [129]. Hence, considering the void probability of walls existing within the link between AP_i and UE_j, we obtain $\rho_{\mathrm{W}}^{\mathrm{LoS}}(l_{ij})$ as

$$\begin{aligned} \rho_{\mathrm{W}}^{\mathrm{LoS}}(l_{ij}) &= e^{-\widetilde{\lambda}_{\mathrm{W},ij}} \\ &= e^{-\lambda_{\mathrm{W}} \mathbb{E}[L_{\mathrm{W}}] \frac{1}{2}\left(|\sin(\phi_{ij})| + |\cos(\phi_{ij})|\right) l_{ij}}. \end{aligned} \tag{C.2}$$

We note that the analysis for the coverage probability is mathematically intractable if the expression for $\rho_{\mathrm{W}}^{\mathrm{LoS}}(l_{ij})$ in (C.2) is in its current form. To address this intractability, we use the fact that ϕ_{ij} is uniformly distributed between $-\pi$ and π,

and approximate $\rho_{\mathrm{W}}^{\mathrm{LoS}}(l_{ij})$ for the binary wall orientation as

$$\rho_{\mathrm{W}}^{\mathrm{LoS}}(l_{ij}) = e^{-\lambda_{\mathrm{W}}\mathbb{E}[L_{\mathrm{W}}]\mathbb{E}_{\phi_{ij}}[\xi(\phi_{ij})]l_{ij}}, \tag{C.3}$$

where $\mathbb{E}_{\phi_{ij}}\left[\xi(\phi_{ij})\right] = \int_{-\pi}^{\pi} \xi(\phi_{ij})\frac{1}{2\pi}\mathrm{d}\phi_{ij} = \frac{2}{\pi}$. This approximation allows us to obtain (5.8).

C.2 Proof of Lemma 5.3

Recall that AP_i is assumed to select its associated UE, UE_i, such that the link between the AP_i and UE_i is not blocked by wall blockers. Thus, to formulate $\Gamma_l(l_{ii})$, we first find the PDF of the distance to a random UE located around AP_i, denoted by $\Gamma_{\widetilde{l}}(\widetilde{l}_{ii})$, as

$$\Gamma_{\widetilde{l}}(\widetilde{l}_{ii}) = \begin{cases} \frac{2\widetilde{l}_{ii}}{L_{\mathrm{T}}}, & 0 \leq \widetilde{l}_{ii} \leq L_{\mathrm{T}}, \\ 0, & \text{otherwise.} \end{cases} \tag{C.4}$$

Next, using (C.4) and Lemma 5.2, we express $\Gamma_l(l_{ii})$ as

$$\Gamma_l(l_{ii}) = \widetilde{\lambda}_{\mathrm{W},3}\Gamma_{\widetilde{l}}(\widetilde{l}_{ii})e^{-\widetilde{\lambda}_{\mathrm{W},1}l_{ii}}, \tag{C.5}$$

where $\widetilde{\lambda}_{\mathrm{W},3}$ is the unknown constant that is utilized to ensure $\int_0^{\infty} \Gamma_l(l_{ii})\mathrm{d}l_{ii} = 1$. Thereafter, substituting (C.4) in (C.5), and applying [116, Eq (2.322.1)], we obtain (5.13).

To find the expression for L_{T} in (5.14), we ensure that the signal-to-noise ratio (SNR) at UE_i when the link between AP_i and UE_i is not blocked is above Υ_{thr} for all possible values of l_{ii} [8]. Therefore, we let the SNR when the UE-AP distance is L_{T} equal Υ_{thr} to obtain (5.14).

C.3 Proof of Proposition 5.1

Let denote ψ_{ij} as the angle that the link between AP_i and UE_j forms with the horizontal plane as shown in Fig. 5.3. For UE_0 to be within the vertical beamwidth

of AP_i, ψ_{ii} needs to satisfy $\psi_{i0} - \frac{\varphi_{\mathrm{A,V}}}{2} \leq \psi_{ii} \leq \psi_{i0} + \frac{\varphi_{\mathrm{A,V}}}{2}$. Therefore, $\rho_{\mathrm{V}}^{\mathrm{hp}}(l_{i0})$ is obtained as

$$\rho_{\mathrm{V}}^{\mathrm{hp}}(l_{i0}) = \int\limits_{\psi_{i0}-\frac{\varphi_{\mathrm{A,V}}}{2}}^{\psi_{i0}-\frac{\varphi_{\mathrm{A,V}}}{2}} \Gamma_{\psi}(\psi_{ii}) d\psi_{ii}, \tag{C.6}$$

where $\Gamma_{\psi}(\psi_{ii})$ is the PDF of ψ_{ii}.

To formulate $\Gamma_{\psi}(\psi_{ii})$, we use the transformation $l_{ii} = h_{\epsilon}\cot(\psi_{ii})$ into Lemma 5.3 to arrive at

$$\Gamma_{\psi}(\psi_{ii}) = \begin{cases} \widetilde{\lambda}_{\mathrm{W},2} h_{\epsilon}^2 \cot(\psi_{ii}) \csc^2(\psi_{ii}) e^{-h_{\epsilon}\widetilde{\lambda}_{\mathrm{W},1}\cot(\psi_{ii})}, & \overline{\psi} \leq \psi_{ii} \leq \frac{\pi}{2}, \\ 0, & \text{otherwise.} \end{cases} \tag{C.7}$$

Finally, by substituting (C.7) into (C.6) and solving the resultant integral by jointly applying [116, Eq (2.02.5)] with [116, Eq (2.521.1)], we obtain (5.15).

C.4 Proof of Proposition 5.3

We note that the *near dominant interferers* lead to outage at UE_0 when their main lobe or the side lobes are facing UE_0. Despite that the locations of all the interferers follow a homogeneous PPP with the density λ_{A}, the interferers that are in LoS with UE_0 within the region $\mathcal{A}^{\mathrm{N}}$ follow a non-homogeneous PPP, due to the distant-dependent nature of the blockage probability. Thus, using Corollary 5.1, we probabilistically thin the original homogeneous PPP to obtain $\Lambda_{\Phi^{\mathrm{N}}}$ as

$$\begin{aligned} \Lambda_{\Phi^{\mathrm{N}}} &= \iint_{\mathcal{A}^{\mathrm{N}}} \lambda_{\mathrm{A}} \rho^{\mathrm{LoS}}(l) l \mathrm{dA} \\ &= \int_0^{v_{\mathrm{s,s},1}} \int_0^{\varphi_{\mathrm{U,H}}} \lambda_{\mathrm{A}} \zeta e^{-\widetilde{\lambda} l} l \mathrm{d}\theta \mathrm{d}l + \int_{\check{l}_{00}}^{v_{\mathrm{m,s}}} \int_0^{\varphi_{\mathrm{U,H}}} \lambda_{\mathrm{A}} \zeta e^{-\widetilde{\lambda} l} l \mathrm{d}\theta \mathrm{d}l \\ &\quad + \int_{\widehat{l}_{00}}^{v_{\mathrm{s,s},2}} \int_0^{\varphi_{\mathrm{U,H}}} \lambda_{\mathrm{A}} \zeta e^{-\widetilde{\lambda} l} l \mathrm{d}\theta \mathrm{d}l + \int_0^{D_{\mathrm{s,s}}} \int_{\varphi_{\mathrm{U,H}}}^{2\pi-\vartheta} \lambda_{\mathrm{A}} \zeta e^{-\widetilde{\lambda} l} l \mathrm{d}\theta \mathrm{d}l. \end{aligned} \tag{C.8}$$

Thereafter, we apply [116, Eq (2.322.1)] into (C.8) to obtain (5.32).

C.5 Proof of Proposition 5.4

Unlike the *near dominant interferers*, for the *far dominant interferers* to cause outage, their main lobe should be facing UE_0. Thus, using Proposition 5.1 and Corollary 5.1, we probabilistically thin the original homogeneous PPP to obtain $\Lambda_{\Phi^{\mathrm{F}}}$ as

$$\begin{aligned}\Lambda_{\Phi^{\mathrm{F}}} &= \iint_{\mathcal{A}^{\mathrm{F}}} \lambda_{\mathrm{A}} \rho^{\mathrm{hp}}(l) \rho^{\mathrm{LoS}}(l) l \mathrm{dA} \\ &= \frac{\lambda_{\mathrm{A}} \zeta \varphi_{\mathrm{A,H}} \varphi_{\mathrm{U,H}}}{2\pi} \Big[\int_{v_{\mathrm{m,s}}}^{v_{\mathrm{m,m}}} \rho_{\mathrm{V}}^{\mathrm{hp}}(l) e^{-\widetilde{\lambda} l} l \mathrm{d}l + \int_{v_{\mathrm{s,s,1}}}^{v_{\mathrm{s,m,1}}} \rho_{\mathrm{V}}^{\mathrm{hp}}(l) e^{-\widetilde{\lambda} l} l \mathrm{d}l + \int_{v_{\mathrm{s,s,2}}}^{v_{\mathrm{s,m,2}}} \rho_{\mathrm{V}}^{\mathrm{hp}}(l) e^{-\widetilde{\lambda} l} l \mathrm{d}l \Big] \\ &\quad + \frac{\lambda_{\mathrm{A}} \zeta \varphi_{\mathrm{A,H}} \left(2\pi - \varphi_{\mathrm{U,H}} - \vartheta\right)}{2\pi} \int_{D_{\mathrm{s,s}}}^{D_{\mathrm{s,m}}} \rho_{\mathrm{V}}^{\mathrm{hp}}(l) e^{-\widetilde{\lambda} l} l \mathrm{d}l, \end{aligned} \tag{C.9}$$

which leads to (5.33).

Bibliography

[1] A. Shafie, N. Yang, S. Durrani, X. Zhou, C. Han, and M. Juntti, "Coverage analysis for 3D terahertz communication systems," *IEEE J. Sel. Areas Commun.*, vol. 39, no. 6, pp. 1817–1832, June 2021.

[2] A. Shafie, N. Yang, S. A. Alvi, C. Han, S. Durrani, and J. M. Jornet, "Spectrum allocation with adaptive sub-band bandwidth for terahertz communication systems," *IEEE Trans. Commun.*, vol. 70, no. 2, pp. 1407–1422, Jan. 2022.

[3] A. Shafie, N. Yang, C. Han, and J. M. Jornet, "Novel spectrum allocation among multiple transmission windows for terahertz communication systems," *IEEE Trans. Veh. Techn.*, vol. 71, no. 12, pp. 13 415–13 421, Dec. 2022.

[4] A. Shafie, N. Yang, C. Li, X. Zhou, and T. Q. Duong, "Spectrum allocation for multiuser terahertz communication systems: An unsupervised learning approach," *submitted to IEEE J. Topics Signal Process.*, Dec. 2022.

[5] A. Shafie, N. Yang, C. Han, J. M. Jornet, M. Juntti, and T. Kürner, "Terahertz communications for 6G and beyond wireless networks: Challenges, key advancements, and opportunities," *IEEE Netw. Mag.*, pp. 1–8, Sept. 2022.

[6] N. Yang and A. Shafie, "Terahertz communications for massive connectivity and security in 6G and beyond era," *IEEE Com. Mag.*, Oct. 2022.

[7] A. Shafie, N. Yang, and C. Han, "Multi-connectivity for indoor terahertz communication with self and dynamic blockage," in *Proc. IEEE Int. Conf. Commun. (ICC)*, Dublin, Ireland, June 2020, pp. 1–7.

[8] A. Shafie, N. Yang, Z. Sun, and S. Durrani, "Coverage analysis for 3D terahertz communication systems with blockage and directional antennas," in *Proc. IEEE Int. Conf. Commun. (ICC) Workshop*, Dublin, Ireland, June 2020, pp. 1–7.

[9] A. Shafie, N. Yang, S. Alvi, S. Durrani, C. Han, and J. M. Jornet, "Adaptive sub-band bandwidth enabled spectrum allocation for terahertz communication systems," in *Proc. IEEE Int. Conf. Commun. (ICC)*, Seoul, South Korea, May 2022, pp. 4013–4018.

[10] A. Shafie, C. Li, N. Yang, X. Zhou, and T. Q. Duong, "An unsupervised learning approach for spectrum allocation in Terahertz communication systems," in *Proc. IEEE Global Commun. Conf. (Globecom)*, Rio de Janeiro, Brazil, Dec. 2022, pp. 3447–3453.

[11] F. Boccardi, R. W. Heath, A. Lozano, T. L. Marzetta, and P. Popovski, "Five disruptive technology directions for 5G," *IEEE Commun. Mag.*, vol. 52, no. 2, pp. 74–80, Feb. 2014.

[12] "Cisco visual networking index: Forecast and methodology 2015 to 2020," CA, USA, CISCO, White Paper, 2015.

[13] M. Giordani, M. Polese, M. Mezzavilla, S. Rangan, and M. Zorzi, "Toward 6G networks: Use cases and technologies," *IEEE Commun. Mag.*, vol. 58, no. 3, pp. 55–61, May 2020.

[14] W. Saad, M. Bennis, and M. Chen, "A vision of 6G wireless systems: Applications, trends, technologies, and open research problems," *IEEE Netw.*, vol. 34, no. 3, pp. 134–142, June 2020.

[15] M. Giordani, M. Polese, M. Mezzavilla, S. Rangan, and M. Zorzi, "Toward 6G networks: Use cases and technologies," *IEEE Commun. Mag.*, vol. 58, no. 3, pp. 55–61, Mar. 2020.

[16] V. Petrov, J. Kokkoniemi, D. Moltchanov, J. Lehtomäki, Y. Koucheryavy, and M. Juntti, "Last meter indoor terahertz wireless access: Performance

insights and implementation roadmap," *IEEE Commun. Mag.*, vol. 56, no. 6, pp. 158–165, June 2018.

[17] J. Lee, E. Tejedor, K. Ranta-aho, H. Wang, K.-T. Lee, E. Semaan, E. Mohyeldin, J. Song, C. Bergljung, and S. Jung, "Spectrum for 5G: Global status, challenges, and enabling technologies," *IEEE Commun. Mag.*, vol. 56, no. 3, pp. 12–18, Mar. 2018.

[18] Z. Lin, X. Du, H.-H. Chen, B. Ai, Z. Chen, and D. Wu, "Millimeter-wave propagation modeling and measurements for 5G mobile networks," *IEEE Wireless Commun.*, vol. 26, no. 1, pp. 72–77, Feb. 2019.

[19] C. J. Rapson, B.-C. Seet, P. H. J. Chong, and R. Klette, "Safety assessment of radio frequency and visible light communication for vehicular networks," *IEEE Wireless Commun.*, vol. 27, no. 1, pp. 186–192, Feb. 2020.

[20] N. Chi, Y. Zhou, Y. Wei, and F. Hu, "Visible light communication in 6G: Advances, challenges, and prospects," *IEEE Veh. Technol. Mag.*, vol. 15, no. 4, pp. 93–102, Dec. 2020.

[21] I. F. Akyildiz, A. Kak, and S. Nie, "6G and beyond: The future of wireless communications systems," *IEEE Access*, vol. 8, pp. 133 995–134 030, July 2020.

[22] V. Petrov, J. Kokkoniemi, D. Moltchanov, J. Lehtomäki, Y. Koucheryavy, and M. Juntti, "Last meter indoor terahertz wireless access: Performance insights and implementation roadmap," *IEEE Commun. Mag.*, vol. 56, no. 6, pp. 158–165, June 2018.

[23] K. M. S. Huq, S. A. Busari, J. Rodriguez, V. Frascolla, W. Bazzi, and D. C. Sicker, "Terahertz-enabled wireless system for beyond-5G ultra-fast networks: A brief survey," *IEEE Netw.*, vol. 33, no. 4, pp. 89–95, July 2019.

[24] C. Chaccour, M. N. Soorki, W. Saad, M. Bennis, and P. Popovski, "Can terahertz provide high-rate reliable low-latency communications for wireless VR?" *IEEE Internet of Things Journal*, vol. 9, no. 12, pp. 9712–9729, June 2022.

[25] I. F. Akyildiz, J. M. Jornet, and C. Han, "Terahertz band: Next frontier for wireless communications," *Phys. Commun.*, vol. 12, pp. 16–32, Sept. 2014.

[26] I. F. Akyildiz, C. Han, Z. Hu, S. Nie, and J. M. Jornet, "Terahertz band communication: An old problem revisited and research directions for the next decade," *IEEE Trans. Commun.*, vol. 70, no. 6, pp. 4250–4285, June 2022.

[27] H. Sarieddeen, N. Saeed, T. Y. Al-Naffouri, and M.-S. Alouini, "Next generation terahertz communications: A rendezvous of sensing, imaging, and localization," *IEEE Commun. Mag.*, vol. 58, no. 5, pp. 69–75, 2020.

[28] A. Goldsmith, *Wireless Communications*. Cambridge, U.K.: Cambridge Univ. Press, 2005.

[29] J. M. Jornet and I. F. Akyildiz, "Channel modeling and capacity analysis for electromagnetic wireless nanonetworks in the terahertz band," *IEEE Trans. Wireless Commun.*, vol. 10, no. 10, pp. 3211–3221, Oct. 2011.

[30] K. Guan, B. Peng, D. He, J. M. Eckhardt, S. Rey, B. Ai, Z. Zhong, and T. Krner, "Measurement, simulation, and characterization of train-to-infrastructure inside-station channel at the terahertz band," *IEEE Trans. THz Sci. Technol.*, vol. 9, no. 3, pp. 291–306, May 2019.

[31] Z. Chen, X. Ma, B. Zhang, Y. Zhang, Z. Niu, N. Kuang, W. Chen, L. Li, and S. Li, "A survey on terahertz communications," *China Commun.*, vol. 16, no. 2, pp. 1–35, Feb. 2019.

[32] C. Han and I. F. Akyildiz, "Distance-aware bandwidth-adaptive resource allocation for wireless systems in the terahertz band," *IEEE Trans. THz Sci. Technol.*, vol. 6, no. 4, pp. 541–553, July 2016.

[33] V. Petrov, J. M. Eckhardt, D. Moltchanov, Y. Koucheryavy, and T. Kürner, "Measurements of reflection and penetration losses in low terahertz band vehicular communications," in *Proc. Eur. Conf. Antennas Propag. (EuCAP)*, Copenhagen, Denmark, Mar. 2020, pp. 1–5.

[34] C. Han and I. F. Akyildiz, "Three-dimensional end-to-end modeling and analysis for graphene-enabled terahertz band communications," *IEEE Trans. Veh. Technol.*, vol. 66, no. 7, pp. 5626–5634, July 2017.

[35] R. Piesiewicz, C. Jansen, S. Wietzke, D. Mittleman, M. Koch, and T. Kürner, "Properties of building and plastic materials in the THz range," *Int. J. Infr. Millim. Waves*, vol. 28, pp. 263–371, Mar. 2007.

[36] H. Elayan, O. Amin, B. Shihada, R. M. Shubair, and M. Alouini, "Terahertz band: The last piece of RF spectrum puzzle for communication systems," *IEEE Open J. Commun. Soc.*, vol. 1, pp. 1–32, Nov. 2019.

[37] H. Sarieddeen, M.-S. Alouini, and T. Y. Al-Naffouri, "An overview of signal processing techniques for terahertz communications," *Proc. of the IEEE*, pp. 1–38, Aug. 2021.

[38] M. Polese, J. M. Jornet, T. Melodia, and M. Zorzi, "Toward end-to-end, full-stack 6G terahertz networks," *IEEE Commun. Mag.*, vol. 58, no. 11, pp. 48–54, Nov. 2020.

[39] V. Petrov, T. Kurner, and I. Hosako, "IEEE 802.15.3d: First standardization efforts for sub-terahertz band communications toward 6G," *IEEE Commun. Mag.*, vol. 58, no. 11, pp. 28–33, Nov. 2020.

[40] Z. Hossain and J. M. Jornet, "Hierarchical bandwidth modulation for ultra-broadband terahertz communications," in *Proc. IEEE Int. Conf. Commun. (ICC)*, Shanghai, China, May 2019, pp. 1–7.

[41] P. Boronin, V. Petrov, D. Moltchanov, Y. Koucheryavy, and J. M. Jornet, "Capacity and throughput analysis of nanoscale machine communication through transparency windows in the terahertz band," *Nano Commun. Netw.*, vol. 5, no. 3, pp. 72–82, Sept. 2014.

[42] J. M. Jornet and I. F. Akyildiz, "Femtosecond-long pulse-based modulation for terahertz band communication in nanonetworks," *IEEE Trans. Commun.*, vol. 62, no. 5, pp. 1742–1754, May 2014.

[43] Z. Hossain, C. N. Mollica, J. F. Federici, and J. M. Jornet, "Stochastic interference modeling and experimental validation for pulse-based terahertz communication," *IEEE Trans. Wireless Commun.*, vol. 18, no. 8, pp. 4103–4115, Aug. 2019.

[44] C. Han, I. F. Akyildiz, and W. H. Gerstacker, "Timing acquisition and error analysis for pulse-based terahertz band wireless systems," *IEEE Trans. Veh. Technol.*, vol. 66, no. 11, pp. 10 102–10 113, Nov. 2017.

[45] A. Saeed, O. Gurbuz, A. O. Bicen, and M. A. Akkas, "Variable-bandwidth model and capacity analysis for aerial communications in the terahertz band," *IEEE J. Sel. Areas Commun.*, vol. 39, no. 6, pp. 1768–1784, June 2021.

[46] C. Han, A. O. Bicen, and I. F. Akyildiz, "Multi-wideband waveform design for distance-adaptive wireless communications in the terahertz band," *IEEE Trans. Signal Process.*, vol. 64, no. 4, pp. 910–922, Feb. 2016.

[47] R. Perez, *Space Interference*. Academic Press, 1998.

[48] V. K. Garg and Y.-C. Wang, *The Electrical Engineering Handbook*. Academic Press, 2005.

[49] L. Yan, C. Han, and J. Yuan, "Energy-efficient dynamic-subarray with fixed true-time-delay design for terahertz wideband hybrid beamforming," *IEEE J. Sel. Areas Commun.*, pp. 1–1, Aug. 2022.

[50] A. Moldovan, P. Karunakaran, I. F. Akyildiz, and W. H. Gerstacker, "Coverage and achievable rate analysis for indoor terahertz wireless networks," in *Proc. IEEE Int. Conf. Commun. (ICC)*, Paris, France, May 2017, pp. 1–7.

[51] M. Yu, A. Tang, X. Wang, and C. Han, "Joint scheduling and power allocation for 6G terahertz mesh networks," in *Proc. Int. Conf. Comput. Netw. Commun. (ICNC)*, Big Island, HI, USA, Feb. 2020, pp. 631–635.

[52] X. Zhang, C. Han, and X. Wang, "Joint beamforming-power-bandwidth allocation in terahertz NOMA networks," in *Proc. Int. Conf. Sensing, Commun., Netw. (SECON)*, Boston, MA, USA, Sept. 2019, pp. 1–9.

[53] H. Zhang, Y. Duan, K. Long, and V. C. M. Leung, "Energy efficient resource allocation in terahertz downlink NOMA systems," *IEEE Trans. Commun.*, vol. 69, no. 2, pp. 1375–1384, Feb. 2021.

[54] H. Zhang, H. Zhang, W. Liu, K. Long, J. Dong, and V. C. M. Leung, "Energy efficient user clustering and hybrid precoding for terahertz MIMO-NOMA systems," in *Proc. IEEE Int. Conf. Commun. (ICC)*, Dublin, Ireland, June 2020, pp. 1–5.

[55] S. Boyd and L. Vandenberghe, *Convex Optimization*. Cambridge, U.K.: Cambridge Univ. Press, 2004.

[56] M. Grant and S. Boyd, "CVX: Matlab software for disciplined convex programming, v2.1," http://cvxr.com/cvx, Mar. 2014.

[57] J. Du, C. Jiang, J. Wang, Y. Ren, and M. Debbah, "Machine learning for 6G wireless networks: Carrying forward enhanced bandwidth, massive access, and ultrareliable/low-latency service," *IEEE Veh. Technol. Mag.*, vol. 15, no. 4, pp. 122–134, Sept. 2020.

[58] U. Challita, H. Ryden, and H. Tullberg, "When machine learning meets wireless cellular networks: Deployment, challenges, and applications," *IEEE Commun. Mag.*, vol. 58, no. 6, pp. 12–18, June, 2020.

[59] X. Jia and X. Zhou, "IRS-assisted ambient backscatter communications utilizing deep reinforcement learning," *IEEE Wireless Commun. Letters*, vol. 10, no. 11, pp. 2374–2378, Nov. 2021.

[60] K. M. Thilina, K. W. Choi, N. Saquib, and E. Hossain, "Machine learning techniques for cooperative spectrum sensing in cognitive radio networks," *IEEE J. Sel. Areas Commun.*, vol. 31, no. 11, pp. 2209–2221, Nov. 2013.

[61] T. Nishio, H. Okamoto, K. Nakashima, Y. Koda, K. Yamamoto, M. Morikura, Y. Asai, and R. Miyatake, "Proactive received power prediction using machine learning and depth images for mmWave networks," *IEEE J. Sel. Areas Commun.*, vol. 37, no. 11, pp. 2413–2427, Nov. 2019.

[62] Y. Chen and C. Han, "Deep CNN-based spherical-wave channel estimation for terahertz ultra-massive MIMO systems," in *Proc. IEEE Global Commun. Conf. (Globecom)*, Taipei, Taiwan, Dec. 2020, pp. 1–6.

[63] X. Liu, Y. Deng, C. Han, and M. D. Renzo, "Learning-based prediction, rendering and transmission for interactive virtual reality in RIS-assisted terahertz networks," *IEEE J. Sel. Areas Commun.*, vol. 40, no. 2, pp. 710–724, Feb. 2022.

[64] S. Fan, Y. Wu, C. Han, and X. Wang, "SIABR: A structured intra-attention bidirectional recurrent deep learning method for ultra-accurate terahertz indoor localization," *IEEE J. Sel. Areas Commun.*, vol. 39, no. 7, pp. 2226–2240, July 2021.

[65] F. Hussain, S. A. Hassan, R. Hussain, and E. Hossain, "Machine learning for resource management in cellular and IoT networks: Potentials, current solutions, and open challenges," *IEEE Commun. Surveys Tuts.*, vol. 22, no. 2, pp. 1251–1275, Jan. 2020.

[66] M. Eisen, C. Zhang, L. F. O. Chamon, D. D. Lee, and A. Ribeiro, "Learning optimal resource allocations in wireless systems," *IEEE Trans. Signal Process.*, vol. 67, no. 10, pp. 2775–2790, May 2019.

[67] C. Li, C. She, N. Yang, and T. Q. S. Quek, "Secure transmission rate of short packets with queueing delay requirement," *IEEE Trans. Wireless Commun.*, vol. 21, no. 1, pp. 203–218, Jan. 2022.

[68] H. Yuan, N. Yang, K. Yang, C. Han, and J. An, "Enabling massive connections using hybrid beamforming in terahertz micro-scale networks," in *Proc. IEEE Wireless Commun. Netw. Conf. (WCNC)*, Seoul, South Korea, June 2020, pp. 1–7.

[69] W. Gao, Y. Chen, C. Han, and Z. Chen, "Distance-adaptive absorption peak modulation for terahertz covert communications," *IEEE Trans. Wireless Commun.*, vol. 20, no. 3, pp. 2064–2077, Nov. 2020.

[70] N. Hosseini, M. Khatun, C. Guo, K. Du, O. Ozdemir, D. W. Matolak, I. Guvenc, and H. Mehrpouyan, "Attenuation of several common building materials: Millimeter-wave frequency bands 28, 73, and 91 GHz," *IEEE Antennas and Propagation Mag.*, vol. 63, no. 6, pp. 40–50, Dec. 2021.

[71] I. K. Jain, R. Kumar, and S. S. Panwar, "The impact of mobile blockers on millimeter wave cellular systems," *IEEE J. Sel. Areas Commun.*, vol. 37, no. 4, pp. 854–868, Apr. 2019.

[72] V. Petrov, M. Komarov, D. Moltchanov, J. M. Jornet, and Y. Koucheryavy, "Interference and SINR in millimeter wave and terahertz communication systems with blocking and directional antennas," *IEEE Trans. Wireless Commun.*, vol. 16, no. 3, pp. 1791–1808, Mar. 2017.

[73] D. Moltchanov, P. Kustarev, and Y. Koucheryavy, "Analytical approximations for interference and SIR densities in terahertz systems with atmospheric absorption, Directional antennas and blocking," *Phys. Commun.*, vol. 26, pp. 21–30, Feb. 2018.

[74] X. Yao, C. Wang, W. Wang, and C. Han, "Stochastic geometry analysis of interference and coverage in terahertz networks," *Nano Commun. Netw.*, vol. 13, pp. 9–19, Sept. 2017.

[75] C. Wang, X. Yao, C. Han, and W. Wang, "Interference and coverage analysis for terahertz band communication in nanonetworks," in *Proc. IEEE Global Commun. Conf. (Globecom)*, Singapore, Singapore, Dec. 2017, pp. 1–6.

[76] T. Bai, R. Vaze, and R. W. Heath, "Analysis of blockage effects on urban cellular networks," *IEEE Trans.Wireless Commun.*, vol. 13, no. 9, pp. 5070–5083, Sep. 2014.

[77] T. Bai and R. W. Heath, "Analysis of self-body blocking effects in millimeter wave cellular networks," in *Proc. Asilomar Conf. Signals, Syst. Comput.*, Pacific Grove, CA, USA, Nov. 2014, pp. 1921–1925.

[78] R. Liu, M. Lee, G. Yu, and G. Y. Li, "User association for millimeter-wave networks: A machine learning approach," *IEEE Trans. Commun.*, vol. 68, no. 7, pp. 4164–4174, July 2020.

[79] M. Suer, C. Thein, H. Tchouankem, and L. Wolf, "Multi-connectivity as an enabler for reliable low latency communications-an overview," *IEEE Commun. Surveys Tuts.*, vol. 22, no. 1, pp. 156–169, Firstquarter 2020.

[80] Y. Liu, X. Fang, M. Xiao, and S. Mumtaz, "Decentralized beam pair selection in multi-beam millimeter-wave networks," *IEEE Trans. Commun.*, vol. 66, no. 6, pp. 2722–2737, June 2018.

[81] M. F. Özkoc, A. Koutsaftis, R. Kumar, P. Liu, and S. S. Panwar, "The impact of multi-connectivity and handover constraints on millimeter wave and terahertz cellular networks," *IEEE J. Sel. Areas Commun.*, vol. 39, no. 6, pp. 1833–1853, June 2021.

[82] M. Gerasimenko, D. Moltchanov, M. Gapeyenko, S. Andreev, and Y. Koucheryavy, "Capacity of multiconnectivity mmWave systems with dynamic blockage and directional antennas," *IEEE Trans. Veh. Technol.*, vol. 68, no. 4, pp. 34–49, Apr. 2019.

[83] X. Zhou, J. Guo, S. Durrani, and M. Di Renzo, "Power beacon-assisted millimeter wave ad hoc networks," *IEEE Trans. Commun.*, vol. 66, no. 2, pp. 830–844, Feb. 2018.

[84] J. G. Andrews, F. Baccelli, and R. K. Ganti, "A tractable approach to coverage and rate in cellular networks," *IEEE Trans. Commun.*, vol. 59, no. 11, pp. 3122–3134, Nov. 2011.

[85] J. Guo, S. Durrani, and X. Zhou, "Outage probability in arbitrarily-shaped finite wireless networks," *IEEE Trans. Commun.*, vol. 62, no. 2, pp. 699–712, Feb. 2014.

[86] J. Kokkoniemi, J. Lehtomäki, and M. Juntti, "Stochastic geometry analysis for mean interference power and outage probability in THz networks," *IEEE Trans. Wireless Commun.*, vol. 16, no. 5, pp. 3017–3028, May 2017.

[87] J. Sayehvand and H. Tabassum, "Interference and coverage analysis in coexisting RF and dense terahertz wireless networks," *IEEE Wireless Commun. Lett.*, vol. 9, no. 10, pp. 1738–1742, Oct. 2020.

[88] V. Petrov, D. Moltchanov, and Y. Koucheryavy, "Interference and SINR in dense terahertz networks," in *Proc. IEEE Veh. Technol. Conf. (VTC-Fall)*, Boston, MA, USA, Sept. 2015, pp. 1–5.

[89] Y. Wu, J. Kokkoniemi, C. Han, and M. Juntti, "Interference and coverage analysis for terahertz networks with indoor blockage effects and line-of-sight access point association," *IEEE Trans. Wireless Commun.*, vol. 20, no. 3, pp. 72–86, Nov. 2021.

[90] S. E. Nai, Z. Lei, S. H. Wong, and Y. H. Chew, "Optimizing radio network parameters for vertical sectorization via taguchi's method," *IEEE Trans. Veh. Technol.*, vol. 65, no. 2, pp. 860–869, Feb. 2016.

[91] R. Shafin, H. Chen, Y.-H. Nam, S. Hur, J. Park, J. Zhang, J. H. Reed, and L. Liu, "Self-tuning sectorization: Deep reinforcement learning meets broadcast beam optimization," *IEEE Trans. Wireless Commun.*, vol. 19, no. 6, pp. 4038–4053, June 2020.

[92] O. Maraqa, A. S. Rajasekaran, S. Al-Ahmadi, H. Yanikomeroglu, and S. M. Sait, "A survey of rate-optimal power domain NOMA with enabling technologies of future wireless networks," *IEEE Commun. Surveys Tuts.*, vol. 22, no. 4, pp. 2192–2235, 4th Quart. 2020.

[93] Z. Ding *et al.*, "Application of non-orthogonal multiple access in LTE and 5G networks," *IEEE Commun. Mag.*, vol. 55, no. 2, pp. 185–191, Feb. 2017.

[94] FCC opens 95GHz to 3THz spectrum for 6G, 7G, or whatever, is next. [Online]. Available: https://venturebeat.com/mobile/fcc-opens-95ghz-to-3thz-spectrum-for-6g-7g-or-whatever-is-next/ (Accessed-in-Oct.,-2022)

[95] A. Singh, M. Andrello, N. Thawdar, and J. M. Jornet, "Design and operation of a graphene-based plasmonic nano-antenna array for communication in the

terahertz band," *IEEE J. Sel. Areas Commun.*, vol. 38, no. 9, pp. 2104–2117, Sept. 2020.

[96] J. YU and Y. WEI, "Digital signal processing for high-speed thz communications," *Chinese J. Electronics*, vol. 31, no. 3, pp. 534–546, May 2022.

[97] J.-F. Ruan, F. Lan, Z. Tao, Z.-F. Meng, and S.-W. Ji, "Tunable terahertz metamaterial filter based on applying distributed load," *Phys. Letters A*, vol. 421, p. 127705, Jan. 2022.

[98] P. Sen and J. M. Jornet, "Experimental demonstration of ultra-broadband wireless communications at true terahertz frequencies," in *IEEE 20th Int. Workshop on Signal Process. Advances in Wireless Commun. (SPAWC)*, July 2019, pp. 1–5.

[99] P. Sen, D. A. Pados, S. N. Batalama, E. Einarsson, J. P. Bird, and J. M. Jornet, "The teranova platform: An integrated testbed for ultra-broadband wireless communications at true terahertz frequencies," *Computer Netw.*, p. 107370, June 2020.

[100] TERANOVA: An integrated testbed for true terahertz communications. [Online]. Available: https://unlab.tech/nanodownloads/teranova/ (Accessed-in-Oct.,-2022)

[101] Y. C. Ziming Yu and, G. Wang, W. Gao, and C. Han, "Wideband channel measurements and temporal-spatial analysis for terahertz indoor communications," in *Proc. IEEE Int. Conf. Commun. (ICC) Workshop*, Dublin, Ireland, June 2020, pp. 1–6.

[102] M. Polese, F. Restuccia, A. Gosain, J. Jornet, S. Bhardwaj, V. Ariyarathna, S. Mandal, K. Zheng, A. Dhananjay, M. Mezzavilla, B. James, R. Mark, W. Xin, Z. Michele, M. Arjuna, and M. Tommaso, "MillimeTera: Toward a large-scale open-source mmWave and terahertz experimental testbed," in *Proc. ACM Workshop Millim.-Wave Netw. Sens. Syst.*, Los Cabos, Mexico, Oct. 2019, pp. 27–32.

[103] NI announces sub THz testbed for 6G research. [Online]. Available: https://www.microwavejournal.com/articles/32916-ni-announces-sub-thz-testbed-for-6g-research(Accessed-in-Oct. ,-2022)

[104] 6G sub-terahertz R&D testbed demo. [Online]. Available: https://www.keysight.com/au/en/solutions/emerging-technologies/6g-technology.html(Accessed-in-Oct.,-2022)

[105] Huawei conducts 6G research at Ottawa's R&D facility: Report. [Online]. Available: https://www.rcrwireless.com/20190827/business/huawei-6g-research-ottawa(Accessed-in-Oct.,-2022)

[106] L. Rothman, I. Gordon, A. Barbe, D. Benner, P. Bernath, M. Birk, V. Boudon, and L. Brown, "The HITRAN 2008 molecular spectroscopic database," *J. Quantitative Spectroscopy Radiative Transfer*, vol. 110, no. 9, pp. 533–572, July 2009.

[107] A. Saeed, O. Gurbuz, and M. A. Akkas, "Terahertz communications at various atmospheric altitudes," *Physical Commun.*, vol. 41, pp. 101–113, Aug. 2020.

[108] ITU-R, "Attenuation by atmospheric gases and related effects," Recommendation ITU-R P.676-12, Aug. 2019.

[109] M. Ma, X. Huang, B. Jiao, and Y. J. Guo, "Optimal orthogonal precoding for power leakage suppression in DFT-based systems," *IEEE Trans. Commun.*, vol. 59, no. 3, pp. 844–853, Mar. 2011.

[110] J. Ma, R. Shrestha, W. Zhang, L. Moeller, and D. M. Mittleman, "Terahertz wireless links using diffuse scattering from rough surfaces," *IEEE Trans. THz Sci. Technol.*, vol. 9, no. 5, pp. 463–470, Sept. 2019.

[111] Y. Xing, O. Kanhere, S. Ju, and T. S. Rappaport, "Indoor wireless channel properties at millimeter wave and sub-terahertz frequencies," in *Proc. IEEE Global Commun. Conf. (Globecom)*, Waikoloa, HI, USA, Dec. 2019, pp. 1–6.

[112] V. Petrov, D. Moltchanov, J. M. Jornet, and Y. Koucheryavy, "Exploiting multipath terahertz communications for physical layer security in beyond 5G networks," in *IEEE Conf. Comput. Commun. Workshops (INFOCOM Wkshps)*, Paris, France, Apr. 2019, pp. 865–872.

[113] X. Yao, C. Wang, and C. Qi, "Interference and coverage analysis for indoor THz communications with beamforming antennas," in *Proc. IEEE/CIC Int. Conf. Commun. Workshops in China (ICCC Wkshps)*, Aug. 2019, pp. 147–152.

[114] R. Liu, Q. Chen, G. Yu, and G. Y. Li, "Joint user association and resource allocation for multi-band millimeter-wave heterogeneous networks," *IEEE Trans. Commun.*, vol. 67, no. 12, pp. 8502–8516, Dec. 2019.

[115] Z. Wang, V. Aggarwal, and X. Wang, "Joint energy-bandwidth allocation in multiple broadcast channels with energy harvesting," *IEEE Trans. Commun.*, vol. 63, no. 10, pp. 3842–3855, Oct. 2015.

[116] I. S. Gradshteyn and I. M. Ryzhik, *Table of Integrals, Series, and Products*, 7th ed. San Diego, CA: Academic press, 2007.

[117] R. Fourer, D. Gay, and B. Kernighan, "AMPL: A mathematical programing language," in *Algorithms and Model Formulations in Mathematical Programming. (NATO ASI Series, Series F: Computer and Systems Sciences)*, vol. 51, S. W. Wallace, Ed. Berlin, Germany: Springer, 1989.

[118] E. Che, H. D. Tuan, and H. H. Nguyen, "Joint optimization of cooperative beamforming and relay assignment in multi-user wireless relay networks," *IEEE Trans. Wireless Commun.*, vol. 13, no. 10, pp. 5481–5495, Oct. 2014.

[119] S. A. Alvi, X. Zhou, S. Durrani, and D. T. Ngo, "Sequencing and scheduling for multi-user machine-type communication," *IEEE Trans. Commun.*, vol. 68, no. 4, pp. 2459–2473, Apr. 2020.

[120] D. W. K. Ng and R. Schober, "Secure and green SWIPT in distributed antenna networks with limited backhaul capacity," *IEEE Trans. Wireless Commun.*, vol. 14, no. 9, pp. 5082–5097, Sept. 2015.

[121] T. T. Vu, D. T. Ngo, M. N. Dao, S. Durrani, and R. H. Middleton, "Spectral and energy efficiency maximization for content-centric C-RANs with edge caching," *IEEE Trans. Commun.*, vol. 66, no. 12, pp. 6628–6642, Dec. 2018.

[122] B. R. Marks and G. P. Wright, "A general inner approximation algorithm for nonconvex mathematical programs," *Oper. Res.*, vol. 26, no. 4, pp. 681–683, Aug. 1978.

[123] S. Choi, J. Choi, and S. Bahk, "Mobility-aware analysis of millimeter wave communication systems with blockages," *IEEE Trans. Veh. Technol.*, vol. 69, no. 6, pp. 5901–5912, June 2020.

[124] G. R. MacCartney, S. Deng, S. Sun, and T. S. Rappaport, "Millimeter-wave human blockage at 73 GHz with a simple double knife-edge diffraction model and extension for directional antennas," in *Proc. IEEE Veh. Technol. Conf. (VTC-Fall)*, Montreal, QC, Canada, Sept. 2016, pp. 1–6.

[125] P. Nain, D. Towsley, B. Liu, and Z. Liu, "Properties of random direction models," in *Proc. IEEE Conf. Comput. Commun. Workshops (INFOCOM Wkshps)*, Miami, FL, Mar. 2005, pp. 1897–1907.

[126] V. Petrov, D. Solomitckii, A. Samuylov, M. A. Lema, M. Gapeyenko, D. Moltchanov, S. Andreev, V. Naumov, K. Samouylov, M. Dohler, and Y. Koucheryavy, "Dynamic multi-connectivity performance in ultra-dense urban mmWave deployments," *IEEE J. Sel. Areas Commun.*, vol. 35, no. 9, pp. 2038–2055, Sep. 2017.

[127] M. Gapeyenko, A. Samuylov, M. Gerasimenko, D. Moltchanov, S. Singh, M. R. Akdeniz, E. Aryafar, N. Himayat, S. Andreev, and Y. Koucheryavy, "On the temporal effects of mobile blockers in urban millimeter-wave cellular scenarios," *IEEE Trans. Veh. Technol.*, vol. 66, no. 11, pp. 10 124–10 138, Nov. 2017.

[128] M. K. Müller, M. Taranetz, and M. Rupp, "Analyzing wireless indoor communications by blockage models," *IEEE Access*, vol. 5, pp. 2172–2186, Dec. 2016.

[129] H. Zheng, J. Zhang, H. Hu, and J. Zhang, "The analysis of indoor wireless communications by a blockage model in ultra-dense networks," in *Proc. IEEE Veh. Technol. Conf. (VTC-Fall)*, Aug. 2018, pp. 1–6.

[130] R. Kovalchukov, D. Moltchanov, A. Samuylov, A. Ometov, S. Andreev, Y. Koucheryavy, and K. Samouylov, "Evaluating SIR in 3D millimeter-wave deployments: Direct modeling and feasible approximations," *IEEE Trans. Wireless Commun.*, vol. 18, no. 2, pp. 879–896, Feb. 2019.

[131] S. Wu, R. Atat, N. Mastronarde, and L. Liu, "Improving the coverage and spectral efficiency of millimeter-wave cellular networks using device-to-device relays," *IEEE Trans. Commun.*, vol. 66, no. 5, pp. 2251–2265, May 2018.

[132] N. Khalid, N. A. Abbasi, and O. B. Akan, "Capacity and coverage analysis for FD-MIMO based THz band 5G indoor internet of things," in *Proc. IEEE Int. Symp. Personal, Indoor, and Mobile Radio Commun. (PIMRC)*, Montreal, QC, Canada, Oct. 2017, pp. 1–7.

[133] Y. Wu and C. Han, "Interference and coverage analysis for indoor terahertz wireless local area networks," in *Proc. IEEE Global Commun. Conf. (Globecom) Workshop*, Waikoloa, HI, USA, Dec. 2019, pp. 1–6.

[134] H. C. Rajpoot, "HCR's Theory of Polygon (proposed by harish chandra rajpoot)" solid angle subtended by any polygonal plane at any point in the space," *Inter. J. Mathematics and Physical Sci. Research*, vol. 2, no. 2, pp. 1–30, 2014.

[135] 3GPP, "Study on channel model for frequency spectrum above 6 GHz," 3GPP TR 38.900 V14.2.0, June 2017.